Superconductivity Program for Electric Systems Annual Progress Report for Fiscal Year 2002

Superconductivity Technology Center
Los Alamos National Laboratory

Dean E. Peterson, Center Director and Program Manager

Jeffrey O. Willis, Principal Team Leader and Editor

Contributors:

P.N. Arendt	P. Gifford[a]	A. Neuber[b]
S.P. Ashworth	J.R. Groves	P.J. Pellegrino[#]
H.J. Boenig	M.E. Hawley	D.E. Peterson
R. Bramlett	T.G. Holesinger	Y. Qiao[#]
L.E. Bronisz	J.Y. Huang	D.A. Roybal
N.D. Browning[d]	J.C. Idrobo[d]	V. Selvamanickam[#]
L.N. Bulaevskii	S.S. Indrakanti[c]	J.E. Serna
B.L. Burley[+]	D.B. Jan	A. Serquis
L. Civale	Q.X. Jia	J.F. Smith
J.Y. Coulter	H. Keene[b]	L. Stan
R.F. DePaula	R.F. Klie[d]	J.A. Stewart
R. Dishman[a]	X.Z. Liao	P. Sutherland[#]
P.C. Dowden	M.P. Maley	J.A. Waynert
R. Edwards	V. Matias	J.O. Willis
L.A. Emmert	C.H. Mielke	X. Yuan[#]
A.T. Findikoglu	N.O. Moreno	Y.T. Zhu
S.R. Foltyn	F.M. Mueller	
B.J. Gibbons	V.F. Nesterenko[c]	

[a]Cryomech, Inc.
[+]General Atomics
[#]IGC-Superpower
[b]Texas Tech University
[c]University of California-San Diego
[d]University of Illinois at Chicago

Table of Contents

Table of Figures

8

Glossary of Acronyms

ANL	Argonne National Laboratory
AMSC	American Superconductivity Corporation
BEI	Backscatter Electron Imaging
Bi-2212	$Bi_2Sr_2CaCu_2O_8$
Bi-2223	$(Bi,Pb)_2Sr_2Ca_2Cu_3O_8$
BSCCO	Bi-2212 or Bi-2223
CRADA	Cooperative Research and Development Agreement
EBSD	Electron Back-Scattered Diffraction
EDS	Energy Dispersive Spectroscopy
FCC	Fault Current Controller
FCL	Fault Current Limiter
HGMS	High-Gradient Magnetic Separator
HTS	High-Temperature Superconductivity
IBAD	Ion Beam-Assisted Deposition
IMP	Isothermal Melt Processing
I_c	Critical current of a superconductor, A
J_c	Critical current density of a superconductor, A/cm^2
LANL	Los Alamos National Laboratory
3M	Minnesota Mining and Manufacturing, Inc.
NHMFL	National High-Magnetic Field Laboratory
ORNL	Oak Ridge National Laboratory
OSTI	Oxford Superconductivity Technology, Inc.
PLD	Pulsed-Laser Deposition
PMC	Prototype Multi-Strand Cable
RBS	Rutherford Backscattering Spectroscopy
RHEED	Reflection High-Energy Electron Diffraction
SAD	Selected Area Diffraction
SCE	Southern California Edison
SEM	Scanning Electron Microscopy
Sm-123	$SmBa_2Cu_3O_{7-\delta}$
SNL	Sandia National Laboratories
SPI	Superconductivity Partnership Initiative
STC	Superconductivity Technology Center (Los Alamos)
T_c	Critical temperature for superconductivity, K
TEM	Transmission Electron Microscopy
XRD	X-Ray Diffraction
YBCO	$YBa_2Cu_3O_{7-\delta}$
YSZ	Yttria-Stabilized Zirconia

Introduction

Tremendous progress was made during the past year in development of High Temperature Superconductors (HTS). Properties of commercially available BSCCO tapes continued to improve resulting in further reductions in cost. The second generation coated conductors continued to show improved superconducting properties in longer lengths. Power applications involving HTS prototype demonstrations in Superconductivity Partnership Initiatives further emphasized the exciting potential of these materials.

LANL refocused our coated conductor development onto IBAD MgO templates, which were shown to yield excellent superconducting properties in short lengths when continuously and rapidly processed. The research yielded new promising buffer layer assemblies and thicker superconducting films for higher current carrying abilities. Replacement of the amorphous silicon nitride layer with a yttria layer substantially reduced the control requirements for the IBAD MgO deposition.

The LANL Research Park became fully operational with an electropolisher, IBAD, PLD, and superconductor characterization facilities equipped and staffed. These capabilities within the national superconductor program offer numerous possibilities for collaborations.

LANL, in partnership with industry representatives, fully restored and tested one phase of the 15 kV fault current controller, demonstrating that it could fully limit a fault without a high voltage breakdown. This effort will be transferred to a fault current limiter operating at a higher voltage.

Our industrial CRADA partnerships with Superpower, American Superconductor, and 3M have been extremely beneficial in accelerating the development of practical superconducting wire with appropriate properties, lengths, and cost for broad power applications.

Research and development activities at LANL related to the HTS program for fiscal year 2002 are collected in this report. Highlights of our technical progress are listed in Section 1, and summaries of individual project areas appear in Section 2. Section 3 lists the 19 journal publications that appeared, the 22 journal articles submitted, together with the 39 other publications and conference abstracts for this year. Section 4 gives the total patent and licensing activity since the inception of the Center in April 1988 to the present. Section 5 lists the various agreements that have been completed or that are underway.

Dean E. Peterson, Leader

Superconductivity Technology Center

1. Highlights of Fiscal Year 2002

- *Using an amorphous Y_2O_3 nucleation layer decreases the process sensitivity for IBAD MgO deposition and eliminates the need for in situ RHEED monitoring.*
- *Introduction of industrially scaleable electropolishing of Ni-alloy substrate tapes provides smooth surfaces and results in high J_c YBCO.*
- *IBAD MgO deposition in the continuous mode resulted in 18 meters with in-plane and out-of-plane textures of 6.6-9.5° and 2.5-3.7°, respectively.*
- *$SrRuO_3$ (SRO) was shown to be an excellent buffer on IBAD MgO, structurally compatible with both MgO and YBCO. It is less sensitive to MgO in-plane textures >10° FWHM than other buffers. It smooths surface height variations in the MgO/Ni-alloy layer and has excellent chemical stability. For a 50 nm thick SRO buffer, J_cs greater than 1 MA/cm^2 for 1 µm YBCO are routinely achieved.*
- *Use of thin Sm-123 interlayers in multilayer YBCO films results in reduced porosity for films thicker than 2 µm. The porosity reduction mechanism does not involve planarization, however, the Sm-123 layers do appear to inhibit the cumulative roughening process that leads to current blocking porosity in thick single layer YBCO films.*
- *YBCO/Sm-123 multilayers show improved performance in field relative to single layer films.*
- *YBCO/Sm-123 multilayers of 3-4 µm thick films have J_c values >1 MA/cm^2 and thus equivalent currents of 300-400 A/cm width at 75 K and self field.*
- *For YBCO grown on IBAD YSZ or single-crystal YSZ substrates, it was found that substrate defects can propagate through the intervening buffer layer and affect YBCO film growth. Proper substrate surface preparation and buffer layer thickness can also be used to reduce the severity of interfacial reactions. The optimal ceria buffer layer thicknesses were found to be 90 Å and 200 Å for IBAD and single-crystal substrates, respectively.*
- *Several laboratories were set up at the Research Park for coated conductor fabrication and characterization. The electropolish system can produce tape at up to 30 m/h with surface finish <1 nm RMS; the IBAD system can prepare IBAD MgO templates over multiple meters with in-plane and out-of-plane textures of 12° and 2.7° FWHM, respectively, at speeds to 6 m/h; the PLD system has been used to deposit YBCO continuously on single-crystal and metal tape substrates. Methods to reduce the ac losses of coated conductors carrying ac transport currents were also developed.*
- *At the Research Park various characterization tools were implemented. In-situ RHEED was used for process optimization and quality control of the IBAD-MgO process. This was used in a combinatorial approach for optimizing various parameters. A Bruker x-ray diffractometer with large area detector was used to characterize crystallographic phases and textures of samples produced at the Research Park. A continuous measurement system to determine the critical current as a function of position along long tapes was implemented.*
- *A microstructural study of the formation of Bi-2223 in silver sheathed tapes shows that defects and secondary phases in the as-rolled tape can significantly affect the alignment and phase development of intermediate Bi-2212 phase, which in turn affects that of the subsequent Bi-2223*

phase. Residual porosity and other structures in the tape after the initial heat treatment must be removed by an intermediate deformation process.

- *Hot isostatic pressing (HIPing) of MgB$_2$ powder results in a much denser, better connected material with similar magnetization critical current density at self field, but better in field performance than a sample pressed and sintered at ambient pressure. The HIPed sample is also found to have less MgO at the grain boundaries and additional dislocations and fine MgO particulates within the MgB2 grains, compared to the un-HIPed sample. Both these microstructural features are expected to enhance flux pinning.*
- *A new high voltage (HV) bus for the Fault Current Controller (FCC) was designed, built, and successfully tested to 15 kV. This followed identification of a number of mechanisms the might be responsible for the HV breakdown observed during initial testing of the FCC.*
- *One of the three phases of the FCC was fully modified and successfully tested on the LANL 13.7 kV substation. The system underwent high voltage standoff testing; it responded appropriately to a 1 MW to 3 MW and back to 1 MW load change; it also responded properly to the shorting of a 1 MW load. The fault current could be varied by adjusting the phase angle firing of the thyristors. Finally, the FCC operated, as predicted, without a bias power supply.*
- *Seven new patents were disclosed and four new patents issued*
- *Four CRADAs were signed this year with American Superconductor Corp., DuPont, General Electric, and Hyper Tech Research*

2. Technical Activities

2.1 Wire Technology

2.1.1 Development of MgO Templates for Coated Conductors Using Ion-Beam Assisted Deposition

P.N. Arendt, S.R. Foltyn, Q.X. Jia, J.R. Groves, T.G. Holesinger, V. Matias, L. Emmert, R. DePaula, L. Stan, P. Dowden, S. Kreiskott, (IGC Superpower-LLC): V. Selvamanickam, Y. Qiao

Preparation of high temperature superconductors on flexible metal substrates for advanced applications like transmission wires, motor windings, or magnets requires lengths of material with the ability to carry sufficient current. Bi-based superconductors have been successfully produced in long lengths using the oxide-powder-in-tube (OPIT) method for some time. However, these superconductors are limited in their application due to their high anisotropy that results in a low irreversibility field at 77 K despite the fact that they have such high superconducting transition temperatures (90 K and above). $YBa_2Cu_3O_{7-\delta}$ (YBCO), when deposited on single-crystal substrates, shows high critical current densities ($>10^6$ A/cm^2 at 77 K) and superior irreversibility as compared to the Bi-based superconductors. However, YBCO exhibits a weak-link behavior in superconducting transport properties as the intergrain boundary angle increases. As a result, deposition of such films on metallic polycrystalline substrates, which provide a robust platform for long length deposition and high mechanical strength for device integration, is problematic.

Our approach initially had been the use of ion-beam assisted deposition (IBAD) to grow a biaxially textured film of yttria-stabilized zirconia (YSZ) on mechanically polished nickel alloys for subsequent pulsed laser deposition (PLD) of YBCO. At LANL, the use of this process has resulted in the fabrication of one-meter long coated conductors with critical current densities (J_c) of 1 MA/cm^2 or better for YBCO films $\geq$ 1 µm. The IBAD YSZ process develops texture by an evolutionary grain growth competition process that requires between 500 to 1000 nm of material to achieve an in-plane texture with a phi scan full width at half maximum (FWHM) of 12°. A small FWHM value is necessary for high performance conductors because large angle grain boundaries reduce the critical current density significantly.

One drawback to the commercialization of the process to lengths in excess of one meter has been the amount of time required to deposit the IBAD YSZ. A typical deposition takes ~20 hours per meter of tape. In 1997, researchers at Stanford found that comparable in-plane texture could be developed using the IBAD process with magnesium oxide (MgO). The major difference between the two material systems is the mechanism that controls the texture development. As mentioned above, IBAD YSZ has an evolutionary texture development character while IBAD MgO requires ~10 nm deposited on (amorphous) a-Si_3N_4 to develop similar texture. Since the deposition rates for the two materials are comparable, this texturing mechanism translates to a process that is ~100 times faster than that of IBAD YSZ.

However, there are a number of difficulties associated with depositing the MgO template layer. When deposited on an a-Si_3N_4 film, the window in thickness to achieve optimally in plane textured MgO is less than 75 Å (7.5 nm) wide. This is shown in Fig. 1. For MgO thicknesses greater than ~100 Å, the c axis of the MgO film begins to tilt away from the

film normal (Fig. 2) and away from the assist ion beam direction. This phenomenon could account for the narrow width of the thickness window.
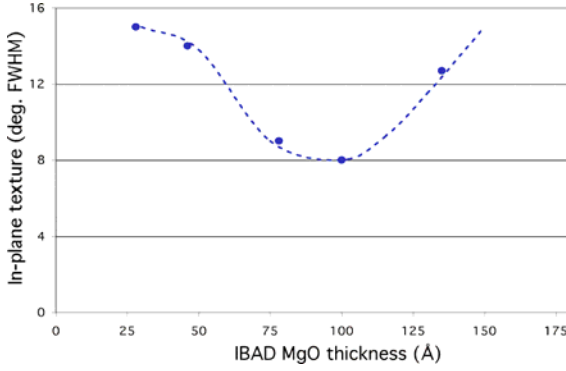
Fig. 1. Optimum texture for IBAD MgO/a-Si$_3$N$_4$ is restricted to a relatively narrow thickness range
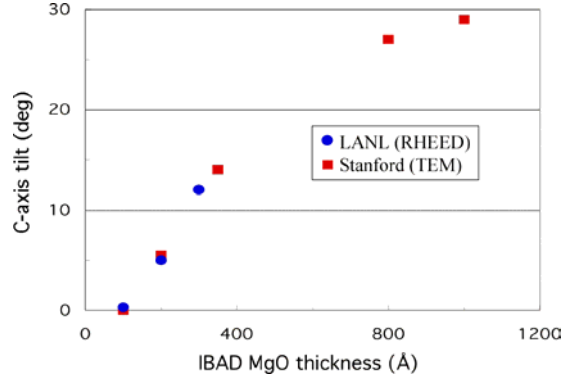
Fig. 2. The c-axis tilt of IBAD MgO increases with film thickness.

It is possible to determine the optimum in-plane texture for the MgO template film using in-situ reflection high-energy electron diffraction (RHEED). The region of greatest RHEED spot intensity, shown in Fig. 3, observed for deposition times of 60 to ~90 seconds, correlates well with the region where x-ray diffraction shows that the in-plane texture is the best.

By investigating other materials as possible candidates for the amorphous nucleation layer, it was found that there is great process sensitivity to this factor. In particular, MgO on a-Y$_2$O$_3$ does not show the drop off in RHEED spot intensity for thicker MgO films.
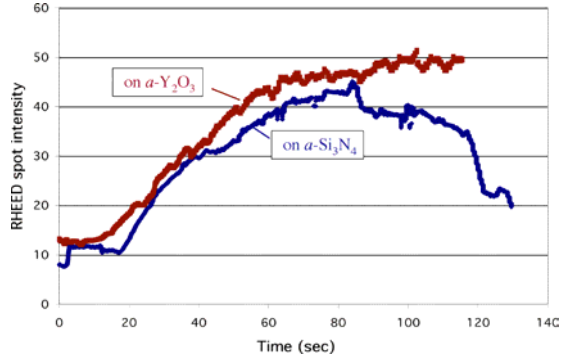
Fig. 3. Optimum texture of IBAD MgO/a-Si$_3$N$_4$ can be obtained using RHEED monitoring of diffraction spot intensity.

Fig. 4. Comparison of RHEED texture as a function of IBAD MgO deposition time for two different amorphous nucleation layers.

Comparing the texture in the MgO film as a function of thickness for the two amorphous nucleation layers, it is found that the optimum texture can be found over a much larger thickness window for MgO on a-Y$_2$O$_3$, as seen in Fig. 5. The window increases from about 75 Å for a-Si$_3$N$_4$ to >100 Å for a-Y$_2$O$_3$. This greatly reduces the requirements on process control for the IBAD MgO deposition process.
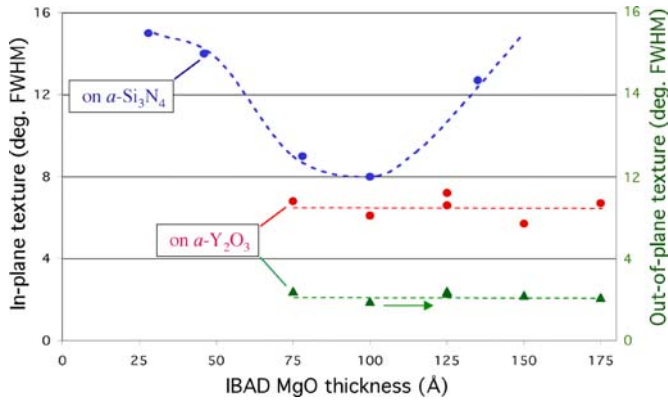
Fig. 5. Comparison of texture as a function of MgO film thickness for two different amorphous nucleation layers. The triangles are the out of plane texture for a-Y_2O_3.

Microstructure analysis of the MgO films deposited on the a-Y_2O_3 on Ni-alloy substrates reveal in general, a well ordered structure. Before the YBCO superconductor layer is deposited, one or more buffer layers are needed. The buffer layers serve both as a chemical barrier layer to protect the YBCO film from the substrate and as a means to achieve better lattice matching. One of these buffers is a homoepitaxial layer of MgO deposited directly on the IBAD MgO layer. In a transmission electron microscopy (TEM) and RHEED investigation, shown in Fig. 6, it is also found that the homoepi-MgO has fewer defects than the IBAD MgO, and therefore acts as both a better chemical barrier and as an improved, more highly textured template layer.
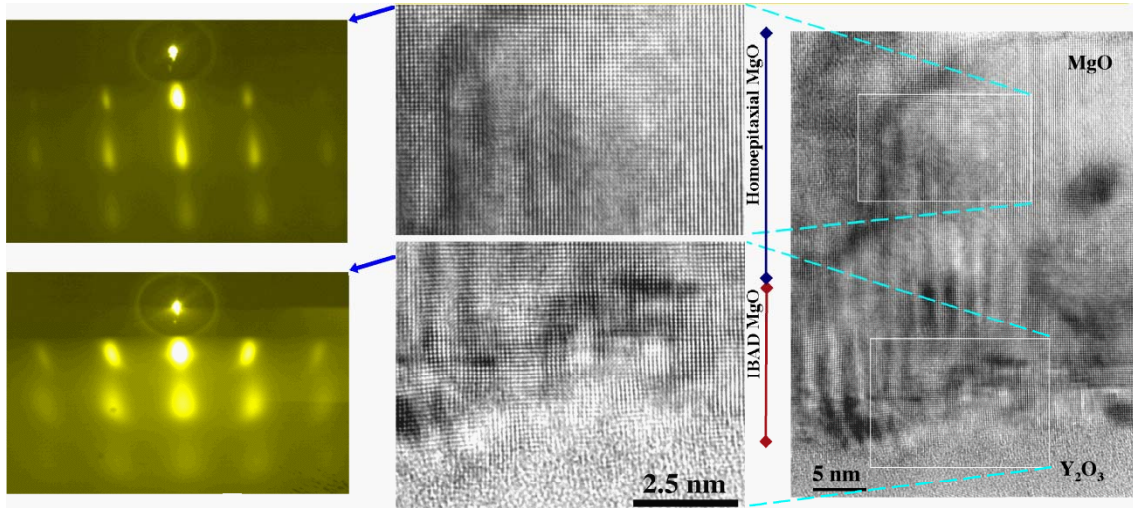
Fig. 6. Microstructure of homoepi-MgO/IBAD MgO/a-Y_2O_3 /Hastelloy C276. Image at right shows a TEM image of the stacking sequence on the Hastelloy. The center shows that the homoepi-MgO has fewer defects than the IBAD MgO. The RHEED images at the points indicated by the areas support this conclusion.

Another requirement that is more stringent for IBAD MgO than it is for the slower, and much thicker IBAD YSZ, is that the substrate roughness must be much less. For C-276 substrates that were orbitally polished at LANL, it was found (Fig. 7) that there is a strong correlation between the substrate roughness and the YBCO in-plane texture. Because of the inverse correlation between the in-plane texture and J_c, this results in a great premium on smooth substrate finishes.

The required surface finishes can now be achieved in long lengths using reel-to-reel polishing systems at both IGC-SuperPower and at LANL. IGC-SuperPower has supplied 100 m lengths of polished substrates to Los Alamos. Fig. 8 shows the achievable finishes and corresponding in-plane textures and critical current densities.
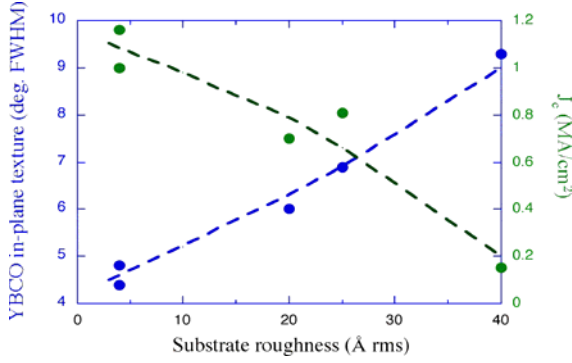
Fig. 7. In-plane texture and critical current density of YBCO/CeO2/YSZ/homoepi-MgO/IBAD MgO/a-Si$_3$N$_4$/orbital polished-C276 as a function of substrate roughness measured by AFM on a 5x5 μm area.
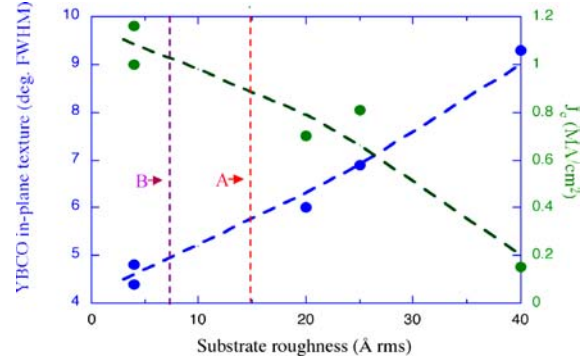
Fig. 8. In-plane texture and critical current density for long length polished substrates. A is the surface finish achieved at IGC-SuperPower. B is the surface finish in the LANL electropolishing system.

The IBAD 1.1 m loop tape transport system, Fig. 9., was used to deposit IBAD MgO on a number of loops in preparation for YBCO deposition. A set of 18 loops had good in-plane alignment values, with median MgO phi-scan peak FWHM values of 8.1-8.5°.
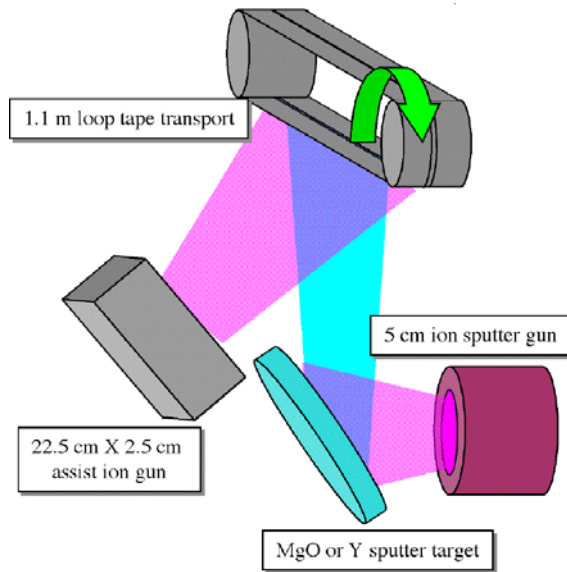
Fig. 9a. Schematic of 1.1 meter IBAD loop coating system.
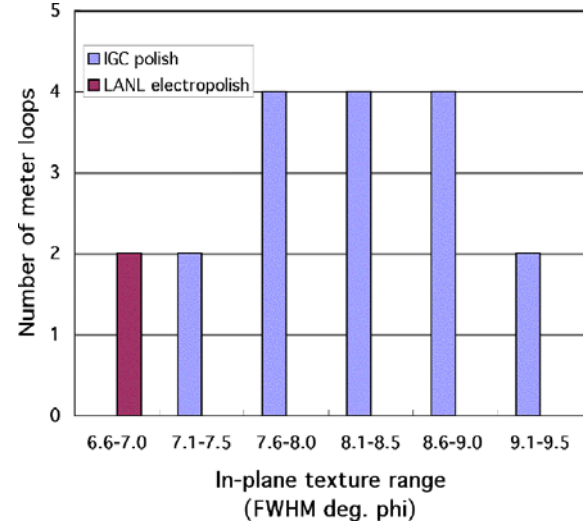
Fig. 9b. Histogram of MgO in-plane texture of 18 meter loops with substrates polished at IGC SuperPower and at LANL.

A short piece from one of these IBAD MgO/Ni-alloy electropolished tapes was coated with PLD YBCO. The texture values achieved were MgO in-plane FWHM = 6.6°, MgO out-of-plane FWHM =2.8°, YBCO in-plane FWHM = 4.9°, and YBCO out-of-plane FWHM =1.5°. For a YBCO film thickness of 1.65 μm, the critical current density at 75 K and self-field was a very good 1.5 MA/cm^2, and an equivalent critical current I$_c$ of 248 A/cm-width.

To assess the texture uniformity along a meter length of IBAD MgO on Hastelloy C276 substrate, a series of 0.5 x 1 cm samples were cut at regular intervals along the length. These were mounted on the heater of the pulsed laser deposition system for buffer layer and YBCO deposition. Two separate runs were made, and the texture results are shown in Fig. 10a. The average in-plane and out-of-plane texture for the entire meter is 5.1° and 1.6° FWHM, respectively. Small bridge samples were patterned on these pieces for J_c measurements. The results are shown in Fig. 10b. The average J_c value is 1.2 MA/cm^2.
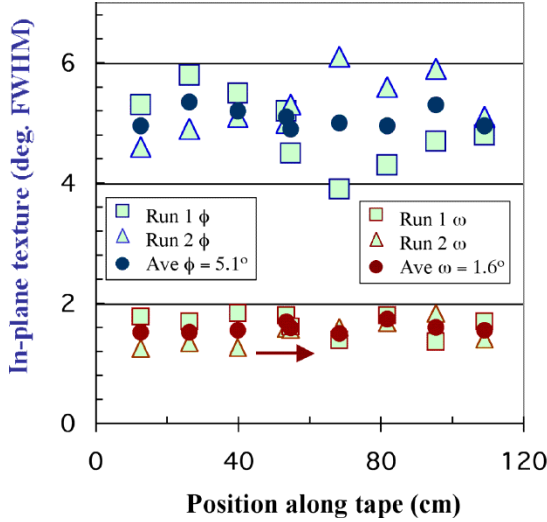
Fig. 10a. In-plane and out-of-plane texture of YBCO on IBAD MgO as a function of position along a 1.1 m tape.
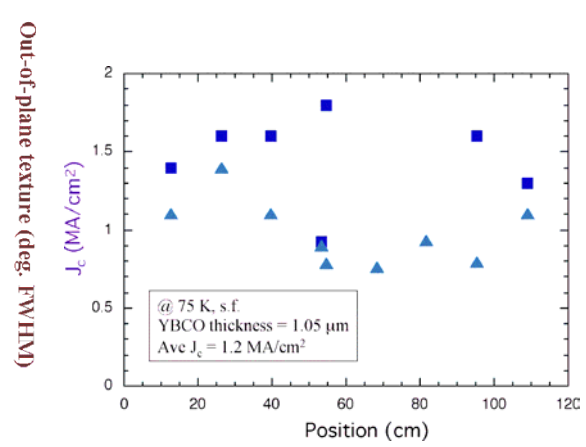
Fig. 10b. Critical current density J_c for 1.05 μm thick YBCO on IBAD MgO as a function of position along a 1.1 m tape.

To summarize the results, the use of an amorphous Y_2O_3 nucleation layer expands the IBAD MgO processing window (to larger thicknesses) and eliminates the need for *in situ* RHEED monitoring. The introduction of industrially scalable electropolishing of the Ni-alloy substrate tapes provides very smooth substrates and results in high critical current density YBCO on IBAD MgO. Deposition of IBAD MgO in the continuous mode produced 18 1.1 m lengths with in-plane and out-of-plane textures of 6.6°-9.5° and 2.5°-3.7° degrees, respectively. Critical current density values for 1.05 μm thick YBCO at 75 K, self-field were in the 1.2 MA/cm^2 range.

2.1.2 Buffer Layer Development for Coated Conductors Using the IBAD-MgO Template

Q.X. Jia, S.R. Foltyn, P.N. Arendt, T.G. Holesinger, J.R. Groves, M.E. Hawley, R.F. DePaula, J.Y. Coulter, P.C. Dowden, L. Stan

Buffer material plays a major role in determining the performance of YBCO films on metal substrates. There are many requirements for a high quality buffer layer: Structural compatibility – must have a good crystallographic lattice match between the HTS film and the template; Thermal stability – must be stable in high temperature oxidizing environment; Chemical stability – there must be minimal chemical interaction between the buffer and adjacent layers; and Barrier capability – the buffer must provide a sufficient barrier against interdiffusion. Some of the presently used buffer layer materials on MgO include $SrTiO_3$ ($Ba_{1-x}Sr_xTiO_3$), CeO_2/YSZ, and $LaMnO_3$ ($La_{1-x}Sr_xMnO_3$).

Our goal here is to develop a stable, effective, and single buffer layer on IBAD-MgO on Ni-alloy for coated conductors. One material we have been investigating is $SrRuO_3$, which has many unique properties making it attractive for use in coated conductors. Crystallographically, it is a pseudocubic perovskite with lattice parameter $a = 3.93$Å. In actuality, it has a small orthorhombic distortion such that $a/b = 1.006$, and $c/(a^2 + b^2)^{1/2} = 1.000$, ($a = 5.573$ Å, $b = 5.538$ Å, $c = 7.856$ Å). $SrRuO_3$ (SRO) is both structurally and chemically compatible with YBCO and MgO. It has excellent diffusion barrier properties. It also has good thermal stability, and is compositionally stable up to 850°C. SRO has high chemical corrosion resistance, being resistant to attack by strong acids.

Successful growth of $SrRuO_3$ thin films and as a buffer layer for YBCO dates from the early days of HTS in the early to mid 90's. Workers at Bell Labs, Conductus, and LANL produced high quality epitaxial SRO films on $SrTiO_3$ and other single crystal substrates and subsequently were able to fabricate high quality YBCO on this buffer layer.

X-ray diffraction reveals that $SrRuO_3$ aligns perfectly on single-crystal MgO. X-ray phi scans of the (132) peaks of SRO shows a strong epitaxial relationship with the (101) peaks of the MgO single crystal substrate (Fig. 11).

Fig. 11a. Phi scans of $SrRuO_3$ on single crystal MgO.

Fig. 11b. Diagram showing angular relationship between the MgO and the SRO reciprocal lattice points on the (001) plane.
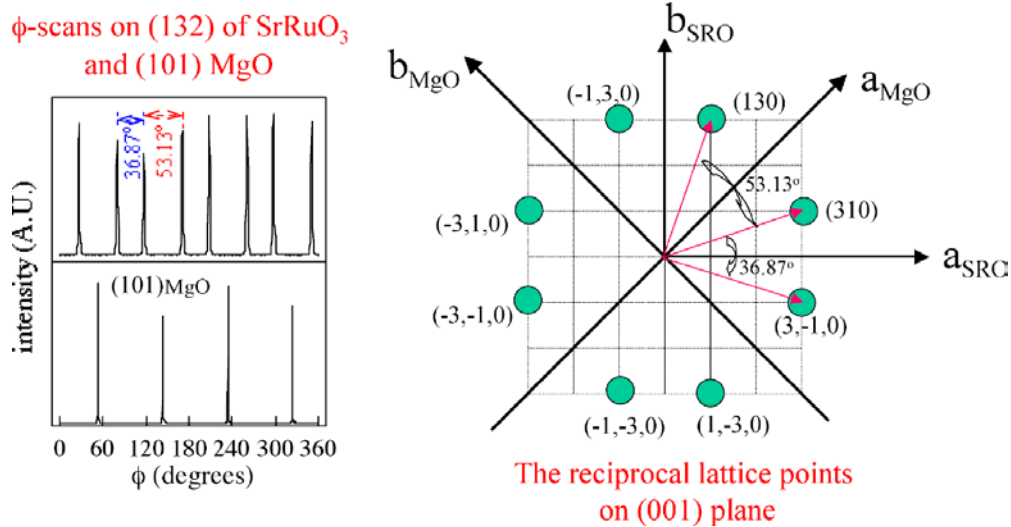
SrRuO$_3$ grown on IBAD-MgO on Ni-alloy substrates shows the same orientation relationship as that grown on crystal MgO. This is illustrated in Fig. 12. Phi-scan peak widths (FWHM) as narrow as ~3.7° have been obtained.
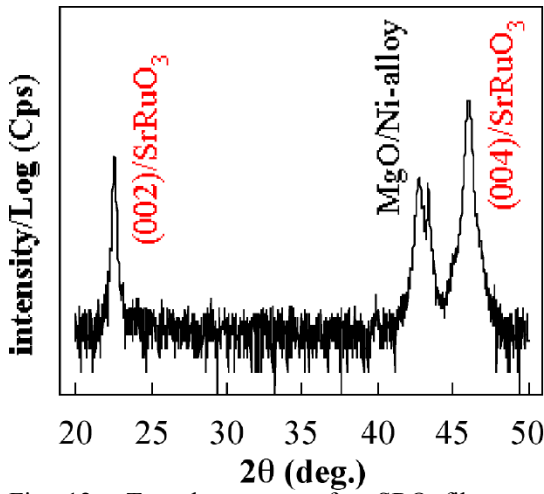
Fig. 12a. Two-theta scan of a SRO film grown epitaxially on IBAD MgO showing only the (00*l*) peaks of the SRO, indicating good c-axis alignment: (001)$_{SRO}$ || (001)$_{MgO}$.
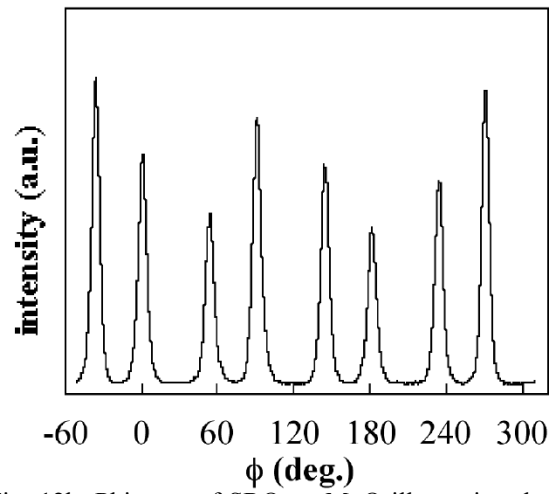
Fig. 12b. Phi scan of SRO on MgO illustrating the relationship <110>$_{SRO}$ || <100>$_{MgO}$. Phi scan FWHM values of 3.7° have been achieved.

SrRuO$_3$ films grown on IBAD-MgO on Ni-alloy show a smooth SRO/MgO interface, a low surface roughness and relatively large grain size, 3 nm and 120 nm, respectively (Figs. 13,14).
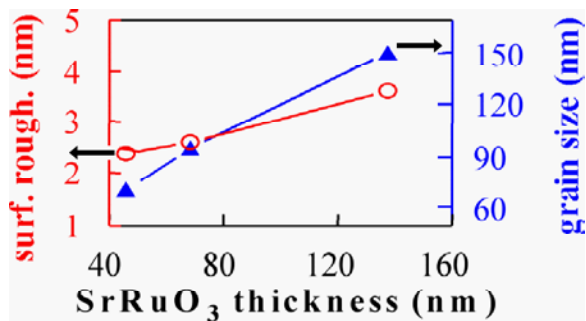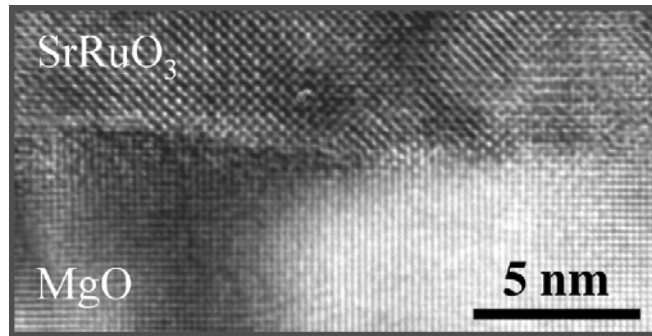
Fig. 13. Top shows a TEM cross sectional image of the clean interface between the MgO template layer and the SrRuO$_3$ buffer. The bottom shows the relationship between the SrRuO$_3$ film thickness and both the surface roughness and the grain size.
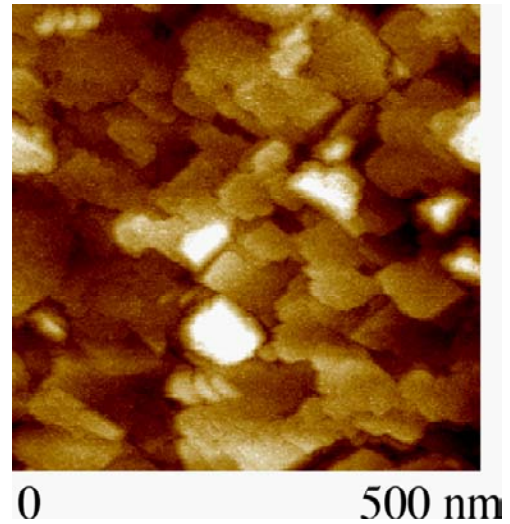
Fig. 14. AFM image of the surface of a SrRuO$_3$ on IBAD-MgO on Ni-alloy showing the relatively smooth surface and large grain sizes.

The epitaxial growth of SrRuO$_3$ is more favorable than that of SrTiO$_3$ on the IBAD-MgO template layer, but see the discussion below on the phi scan FWHM range of validity. The surface character (Fig. 15) of the SrRuO$_3$ film shows a much smoother surface with larger grains.
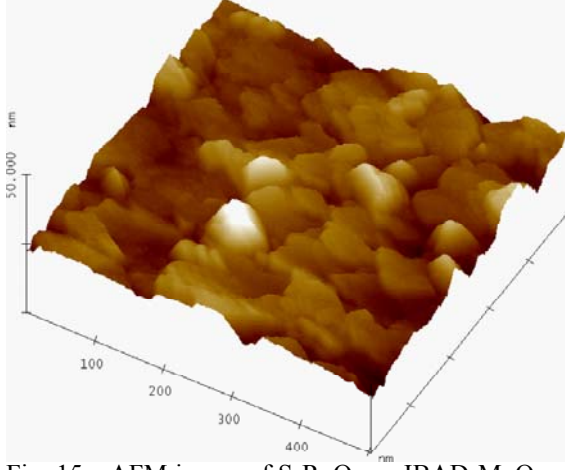
Fig. 15a. AFM image of SrRuO$_3$ on IBAD-MgO on a Ni-alloy substrate showing a relatively smooth surface.
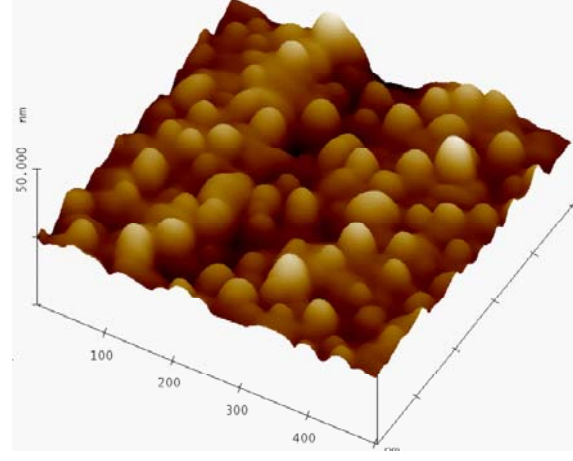
Fig. 15b. AFM image of SrTiO$_3$ buffer layer on IBAD-MgO on a Ni-alloy substrate showing smaller grains and shorter length scale roughness.

YBCO films grown on SrRuO$_3$/IBAD-MgO on Ni-alloy have field and angular dependencies typical of YBCO films deposited on other buffer layers, Fig. 16. Critical current densities at 75.5 K, self-field of 1.7 and 1.8 MA/cm^2 were measured on a 1.3 and 1.1 μm thick films, respectively.
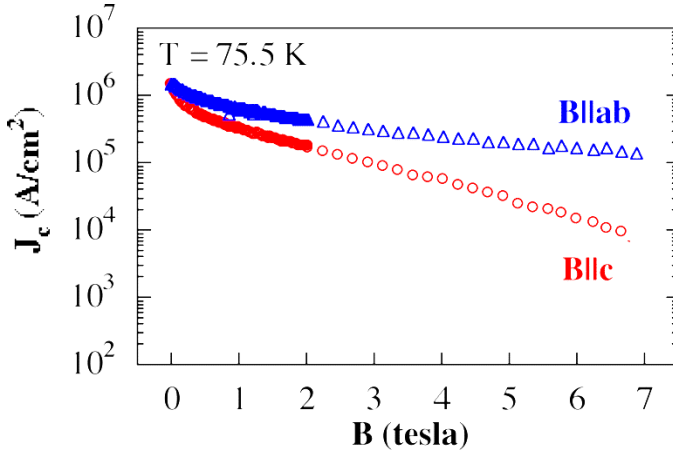
Fig. 16a. Field dependence of a YBCO/SrRuO$_3$/IBAD-MgO/Ni alloy film at 75.5 K, showing behavior typical of most YBCO.
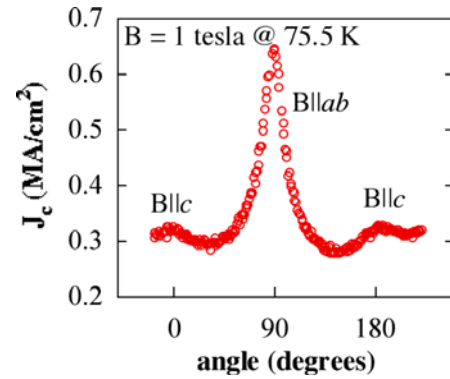
Fig. 16b. Angular dependence of a YBCO film on SRO at 1 T and 75.5 K. T

Experimentally it is known that the in-plane texture of YBCO is generally better than the in-plane texture, as determined by the x-ray diffraction ϕ scan peak width (FWHM), of the IBAD template layer upon which it is deposited. Furthermore, the degree of improvement also depends on the material used for the buffer layer. Fig. 17 illustrates that, especially for only moderately well textured IBAD, the texture improvement for SrRuO$_3$ is much better than that for two other frequently used buffer layer materials, LaMnO$_3$ and SrTiO$_3$.
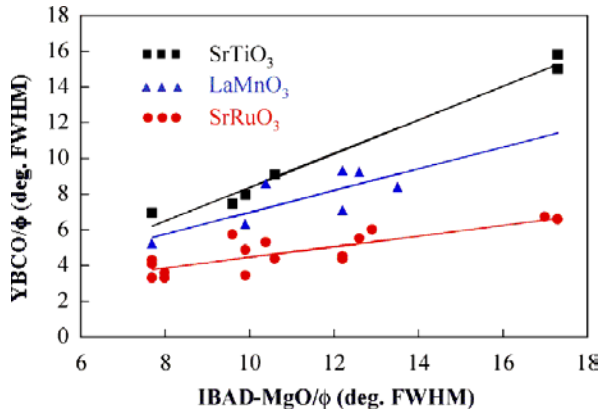
Fig. 17. YBCO ϕ scan peak widths as a function of IBAD MgO ϕ scan peak width for three buffer layer materials.

SrRuO$_3$ can also planarize surface irregularities present on the IBAD-MgO template on the Ni-alloy substrate (Fig. 18). This can help to improve the smoothness and texture of the subsequently deposited YBCO film, and thus its superconducting performance.
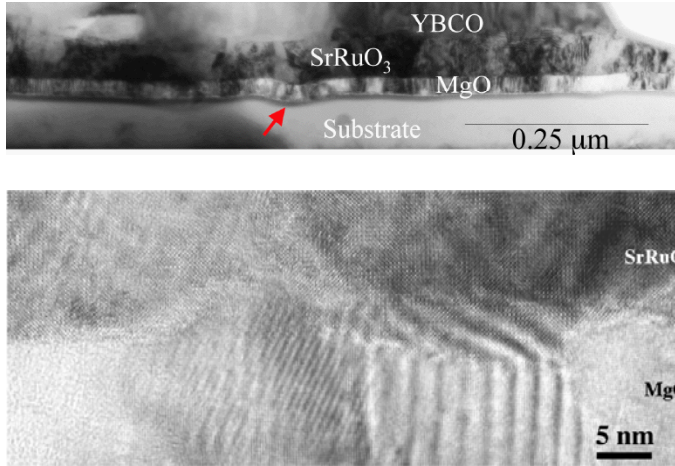
Fig. 18. The SrRuO$_3$ buffer layer is able to smooth out variations in the IBAD MgO/Ni-alloy substrate. Top figure shows the reduced roughness in the YBCO film. The bottom image shows an expanded view of the SrRuO$_3$/MgO interface region.

The SrRuO$_3$ film on IBAD-MgO exhibits superb chemical stability in the presence of hydrofluoric acid and water. A SRO film grown on IBAD MgO on a Ni alloy substrate has an initial texture of 6.0° ((132) line ϕ scan peak FWHM) and rms surface roughness of ~3 nm. The sample was then immersed in buffered HF for 30 minutes followed by 30 minutes in deionized water. No changes were observed in the phi scan peak width or the surface roughness. Subsequently, 1.1 µm of YBCO was applied by pulsed laser deposition. The YBCO showed a ϕ scan peak FWHM of ~4.6°, a ω scan rocking curve FWHM (out of plane texture) of ~1.6°, and a J$_c$ of 1.0 MA/cm^2.

To summarize, SrRuO$_3$ proved to be an excellent buffer on IBAD-MgO for coated conductors. It is structurally compatible with the YBCO conductor and the MgO template layer. It is chemically stable at processing conditions (temperature, pressure and atmosphere). SRO is less sensitive to the in plane texture of the IBAD-MgO layer, yielding YBCO in-plane texture much improved over that of the MgO layer. The SRO layer also tends to smooth out surface height variations in the MgO/Ni-alloy surface. The material has excellent chemical stability in the presence of hydrofluoric acid and water. By using a single buffer SrRuO$_3$ with a thickness of less than 50 nm, J$_c$ > 1 MA/cm^2 has been *routinely* achieved for over 1 µm thick YBCO films on IBAD-MgO on Ni-alloy.

2.1.3 Thick Superconducting Films for High Current Coated Conductors

S.R. Foltyn, Q.X. Jia, P.N. Arendt, J.Y. Coulter, P.C Dowden, T.G. Holesinger

The development of high current coated conductors will require an improvement over the "standard" YBCO produced to date. The reasons can be readily understood by referring to Fig. 19. Fig. 19a shows that the critical current of a YBCO film increases up to a thickness of about 2 µm; at that point it reaches a plateau or even decreases somewhat. This indicates that the upper layers of a YBCO thicker than about 2 µm carry little if any supercurrent. Referring to Fig. 19b, it can be seen that the microstructure begins to show increasing roughness-induced porosity for this film beyond a thickness of ~2 µm, suggesting that this is the source of the plateau in the critical current.
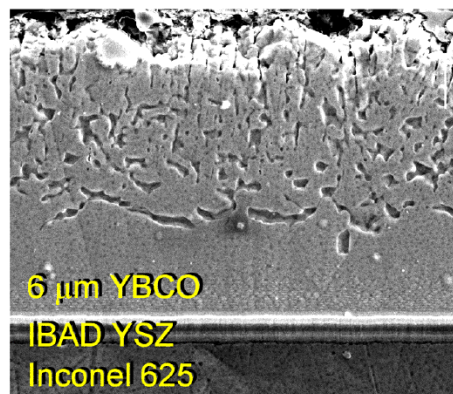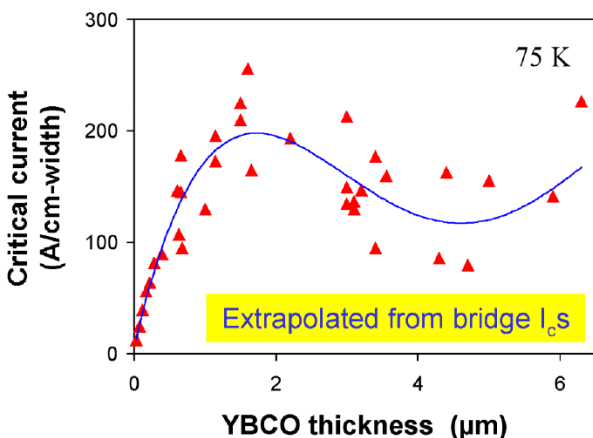
Fig. 19a. Dependence of critical current on YBCO thickness for laser deposited YBCO on CeO_2- or Y_2O_3-buffered IBAD YSZ on Ni-alloy.

Fig. 19b. Cross sectional SEM image of YBCO on IBAD YSZ/Inconel 625.

One of the possible improvements investigated here utilizes ~1 µm YBCO layers separated by thin (~200 nm) layers of $SmBa_2Cu_3O_{7-\delta}$. This multilayer architecture (fig. 20) combines the intrinsically smooth growth habit of $SmBa_2Cu_3O_{7-\delta}$ with the high J_c of YBCO. Such films are dense up to at least 5 µm, and carry current throughout the entire superconductor thickness. In bridges, I_c levels (75 K) of 400 A/cm-width are achieved routinely, with some samples reaching over 500 A/cm-width. On cm-wide, continuously processed tape, an I_c of 335 A has been measured, and a 225 A meter has been produced (2 µm thick, Y-Sm-Y multilayers).

One of the difficulties of reaching high currents is that the high J_c values typical of thin YBCO cannot be maintained in thick films, e.g., achieving 5 MA/cm^2 at 5 µm is not possible at present, Fig. 21. A similar trend in $J_c(t)$ is observed for YBCO on IBAD YSZ coated metal substrates; however, the J_c values on these substrates are only about 2/3 that of those on single-crystal substrates, at least for YBCO thickness <2 µm. For greater thicknesses, the J_c values of single-layer coated conductors drop more rapidly.

The multilayer architecture that is employed here restores the IBAD-based J_c values to the single-crystal trend, but does not alter that trend, as seen in Fig. 22. The self-field J_c values are increased by ~x2 at 4 µm and even more for thicker films. This results in substantially higher critical currents (calculated 400 A/cm-width (75K, sf) for 4 µm) in these thicker films.
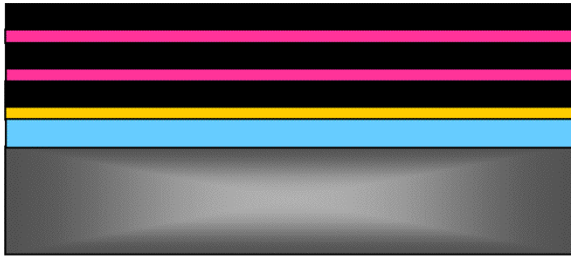
Fig. 20. Schematic showing the architecture of the Y/Sm-123 multilayer films.
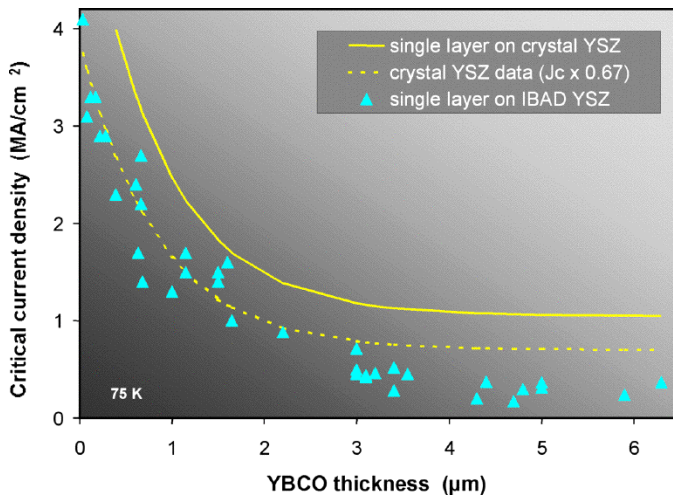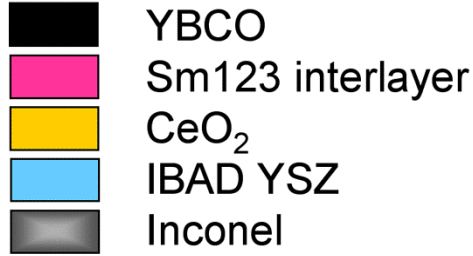
Fig. 21. Thickness dependence of the critical current density of YBCO films. The solid curve is for a single layer on single-crystal YSZ (from 1993 data). The dashed curve is the same data multiplied by 2/3 to scale to the data for single layer YBCO on IBAD YSZ (blue triangles).
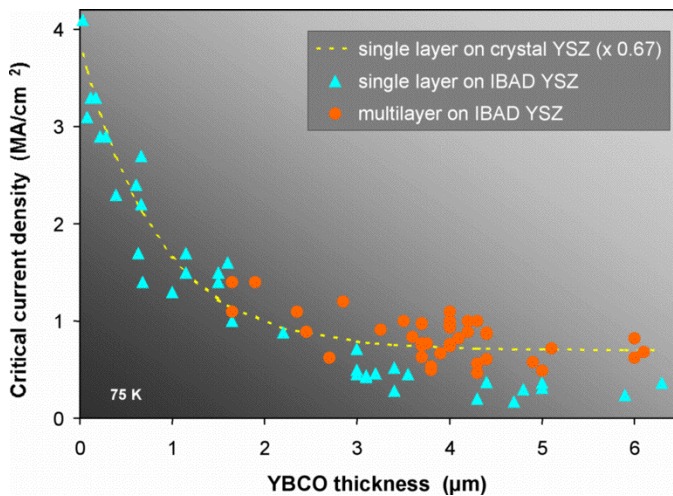
Fig. 22. Critical current density as a function of YBCO film thickness. The multilayer films on IBAD YSZ (Jia *et al*., *Appl. Phys. Lett.* **80**, 1601 (2002)) retain the trend shown by single layer films on single crystal substrates.

25

Several recent samples have exhibited "trend-breaking" potential as shown in Fig. 23. These are films on both IBAD YSZ and on the newer, faster IBAD MgO template layer. These new, higher J_c values, may indicate that, as a result of improvements in many parts of the coated conductor process, present day performance of coated conductors is significantly better than that for older IBAD samples, and even stronger than that of films on single crystals deposited in the past.
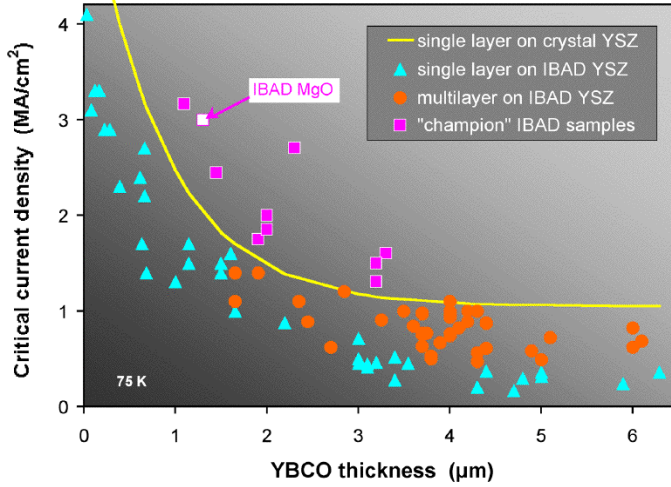
Fig. 23. Recent "champion" values of IBAD samples show Jc values higher than that of films on single-crystalline YSZ.

Examining the magnetic field dependence of $J_c(t)$ (75 K, self field) for single layer thick YBCO films on CeO_2-buffered IBAD YSZ, (Fig. 24a), it is found that J_c is relatively thickness independent up to ~4 T. However, in higher fields, the J_c of thick films falls off more rapidly than that of thinner ones. Fig. 24a also shows comparable data for a 3.2 μm thick multilayer film; its field dependence is comparable to that of a much thinner (1.5 μm) single layer film of comparable J_c value. The net result is that the *absolute* J_c value, and thus critical current performance, is much enhanced over that of the thinner film, and all others, in this study (Fig. 24b).
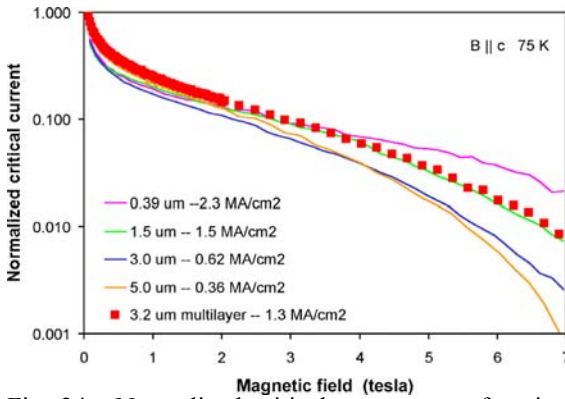
Fig. 24a. Normalized critical current as a function of film thickness for single layer (solid curves) and a multilayer (dashed curve) film.
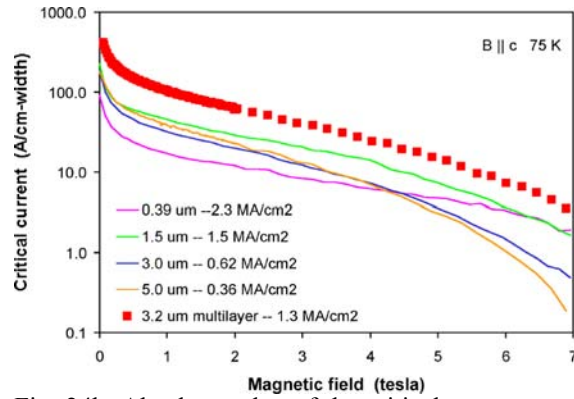
Fig. 24b. Absolute value of the critical current as a function of film thickness for single layer (solid curves) and a multilayer (dashed curve) films.

TEM cross-section analysis (Fig. 25a) reveals that the YBCO grain structure is unaltered by the presence of Sm-123 interlayers. It was previously thought that the Sm-123 interlayers planarize the YBCO surfaces, yielding a smooth surface from which to nucleate the YBCO growth and achieve a well oriented, dense growth morphology. The SEM image in Fig. 25bb shows that, instead, defects in a YBCO layer are mapped by the Sm-123 layer with no apparent smoothing effect. Nevertheless, the Sm-123 layers appear

to inhibit cumulative roughening. The result is that the porosity for total film thicknesses greater than 2 μm is reduced below that in a single layer YBCO film of equivalent thickness. Because the planarization hypothesis should favor thicker layers of Sm-123, and the previous observation that thinner Sm-123 results in higher I_c is contrary to that assumption, these results (Fig. 25c) also support the thesis that planarization is not taking place.
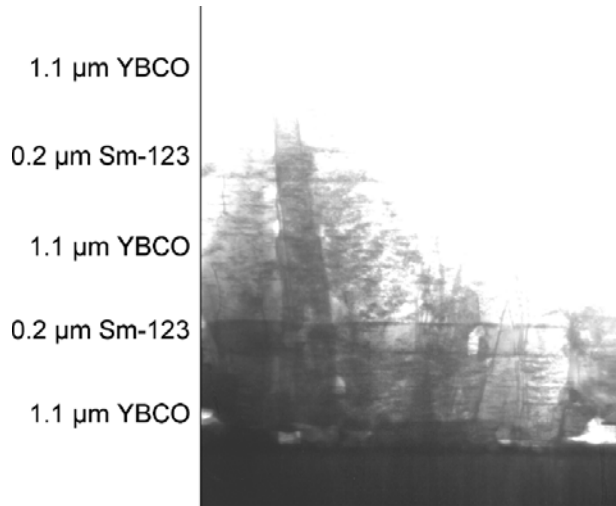
Fig. 25a. Cross sectional TEM image of multilayer film on CeO_2-buffered IBAD showing continuity of YBCO growth morphology.
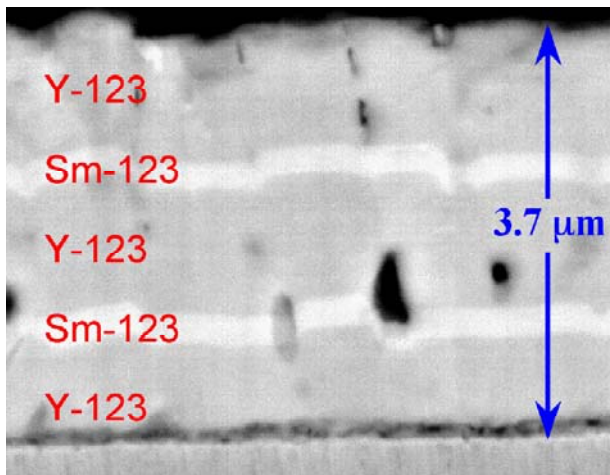
Fig. 25b. Cross sectional SEM image of multilayer film showing no evidence of planarization by the Sm-123 interlayers.
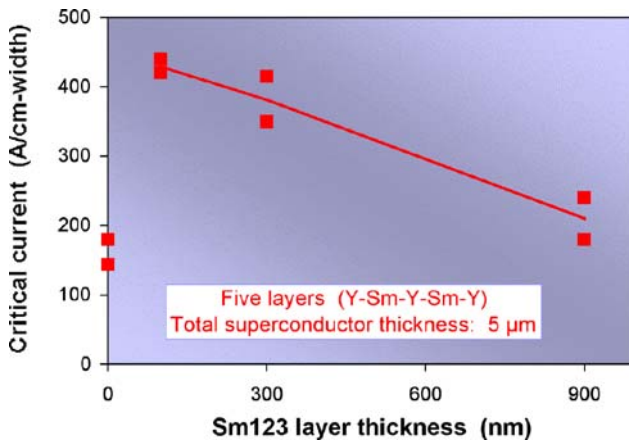
Fig. 25c. Critical current decreases with increasing Sm123 layer thickness for fixed superconductor thickness of 5 μm, suggesting planarization is not occurring.

In addition to the results described above for multilayer films on IBAD YSZ substrates, it has also been possible to achieve excellent performance for multilayer films on the newer IBAD MgO substrates. These data are shown in Fig. 26. The J_c values, while fewer in number, are largely comparable to the best achieved on the IBAD YSZ substrate system.
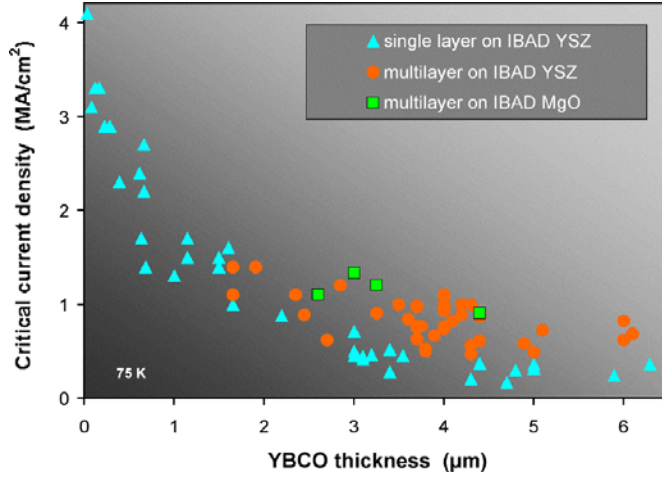
Fig. 26. Critical current density as a function of film thickness for YBCO films on IBAD MgO and on IBAD YSZ.

In conclusion, major improvements in coated conductor performance have been achieved by the introduction of multilayer architecture. YBCO with thin Sm-123 interlayers enable the growth of thicker films by reducing porosity above 2 μm. The mechanism for porosity reduction does not involve planarization of the YBCO surface by the Sm-123 layer, or alteration of the superconductor grain structure. However, the Sm-123 layers do appear to inhibit the cumulative roughening process that leads to current-blocking porosity in thick single layer YBCO films. In addition to the improvements at self-field, multilayers yield higher I_cs in an external magnetic field than do YBCO single-layer films. The performance of multilayers of 3 – 4 μm thickness on IBAD YSZ or IBAD MgO is very good and yields J_c values of greater than 1 MA/cm^2. This is equivalent to critical currents of 3-400 A/cm-width, again at 75 K and self field.

2.1.4 Engineered Microstructures and Transport Properties in YBCO Coated Conductors

T.G. Holesinger, B.J. Gibbons, J.Y. Coulter, S.R. Foltyn, J.R. Groves, and P.N. Arendt

The production of the so-called second-generation "coated conductors" requires a biaxially-textured template for the subsequent oriented growth of additional oxide buffer layers and YBa$_2$Cu$_3$O$_y$ (YBCO). Ion-beam-assisted deposition (IBAD) is one approach that is used for preparing a biaxially-aligned buffer layer on polycrystalline nickel-alloy substrates. In general, YBCO films may be deposited directly onto the IBAD YSZ or MgO templates. However, additional buffer layers have been found to be beneficial in optimizing the transport properties and controlling defects in the YBCO films.

Because the coated conductor process is a layering process, several interfaces are formed along which defects or interfacial reactions may result. These defects can be additive and propagate through the entire film structure to affect the growth and properties of the YBCO film. Structural defects, chemical defects, or a combination of both are often formed along the various interface. Their origins include substrate roughness, lattice mismatch, porosity, contamination, adhesion problems, and interfacial reactions.

One area of specific concern is the underlying buffer layer to the YBCO film. CeO$_2$ is often used successfully as this buffer layer as it is a stable oxide with a good lattice match to YBCO. However, even ceria reacts with YBCO and affects the superconductor's properties. Since it appears that nearly all materials that have been used as buffer layers react with YBCO at typical processing temperatures, it is especially important to understand what general aspects of the interfacial reactions between a given material and YBCO have on the superconducting transport properties. In this paper, various aspects of defect generation in YBCO coated conductors are discussed. Particular attention was paid to the role of the underlying buffer layer to the YBCO and how its thickness can influence the stability of the interface and the properties of the superconducting film.

IBAD was used to produce the biaxially-textured YSZ films on Inconel 625 or Hastelloy substrates. The IBAD YSZ thickness was kept at 0.5 μm. Ceria and YBCO layers were deposited by pulsed laser deposition (PLD) on either the IBAD YSZ templates or single-crystal YSZ substrates. The thickness of the ceria and YBCO layers was varied between 5 and 1000 nm and 1 and 3 micrometers, respectively.

Transmission and scanning electron microscopy (TEM and SEM) samples were prepared in the same manner for viewing in the longitudinal transverse direction (perpendicular to both the nominal c-axis of the film and direction of current flow). Dimple polishing and ion-milling with 3.4 kV Ar ions were used for TEM sample preparation. Phase identification was performed by x-ray diffraction, energy dispersive spectroscopy (EDS) and electron diffraction.

The growth of the YBCO film has been observed to change in order to accommodate substrate and buffer layer defects. Substrate defects that can affect YBCO film growth include surface roughness, cracks, pits or holes, bubbles, and substrate inclusions. Their effects may be reflected in the local alignment of the YBCO film, a structural defect in the YBCO film, the occurrence of an interfacial reaction phase, or a combination thereof. The TEM micrographs of Fig. 27 demonstrate how irregularities in the surface morphology of the substrate can affect film alignment. Rolling and polishing marks can affect the local out-of-plane alignment of the films perpendicular to the long axis of the tapes resulting in the striped contrast present in the TEM micrographs. Localized defects in the substrates can also propagate through the buffer layers and increase the likelihood of an interfacial reaction between the YBCO film and the underlying buffer layer.
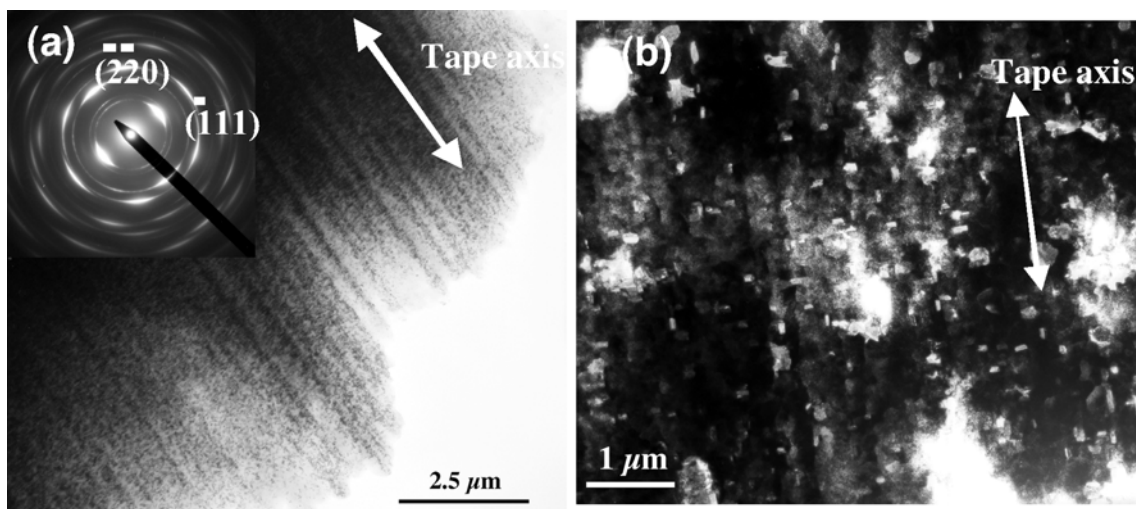
Fig. 27. Plan view TEM micrographs of (a) the IBAD YSZ layer and (b) the YBCO layer of a coated conductor. The images were taken with the beam nominally along the [1-12] and [001] zone axes, respectively. Local misorientations in the YSZ or YBCO from these conditions cause the material to appear brighter in the micrographs. The striped nature of the contrast along the tape axis arises from slight deviations in the alignment of the material due to the surface morphology of the substrate. The small, bright rectangular grains in (b) are a-axis oriented grains.

Shown in Fig. 28 are SEM and TEM micrographs of substrate defects that have propagated through the intervening buffer layers. The SEM micrograph of Fig. 28a shows a large pore structure in the YBCO film that is associated with a pit in the substrate. The TEM micrograph in Fig. 28b reveals a sequence of events in which a localized defect in the substrate affected the local alignment of the IBAD YSZ and ceria films. This was then followed by a severe interfacial reaction between the ceria and YBCO. Above this reaction zone, a large pore structure can be seen in the YBCO film. The J_c and thickness of the film were 1.7 MA/cm^2 (75 K, SF) and 1.5 μm, respectively. The source of almost all the observed interfacial reactions between the YBCO and ceria in this sample could be traced to substrate defects.
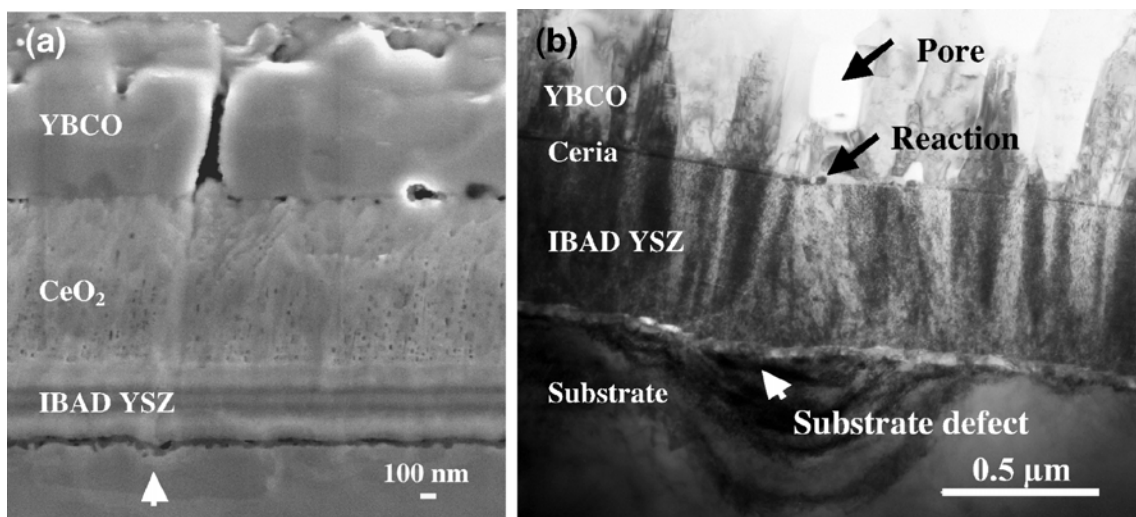
Fig. 28. Examples of localized substrate defects and their affects on the YBCO film growth. The SEM micrograph in (a) shows the formation of a large pore structure in the YBCO film that can be traced to a

30

substrate defect. The TEM micrograph (b) shows the sequence of events that starts with the substrate defect and ends with the formation of a large pore structure in the YBCO film.

No interfacial reactions were observed between the IBAD YSZ and ceria layers. However, the morphology of the interface will follow that of the underlying substrate and, as shown above, defects from the substrate can propagate through this interface and affect the films above it. However, even in the absence of the substrate defects, the ceria layer will in general react with the YBCO film. Shown in Fig. 29 are TEM micrographs of the types of reactions one finds along the interface. In some cases, the YBCO can maintain its alignment as shown in Fig. 29a. In other cases, the reaction phases can cause the growth of misoriented YBCO grains as shown in Fig. 29b. The reaction always results in the formation of $BaCeO_3$. When the reaction is severe, $YCuO_2$ is formed above the $BaCeO_3$ in these films. When the reaction is small, leftover material from the formation of $BaCeO_3$ can diffuse along the grain boundary and intercalate as intergrowths of $Y_2Ba_4Cu_7O_y$ (Y-247) or $Y_2Ba_4Cu_8O_y$ (Y-248). An example of the latter is shown in Fig. 30. The line in Fig. 30 indicates where a discontinuity in the ceria layer is associated with an interfacial reaction that formed the $BaCeO_3$.
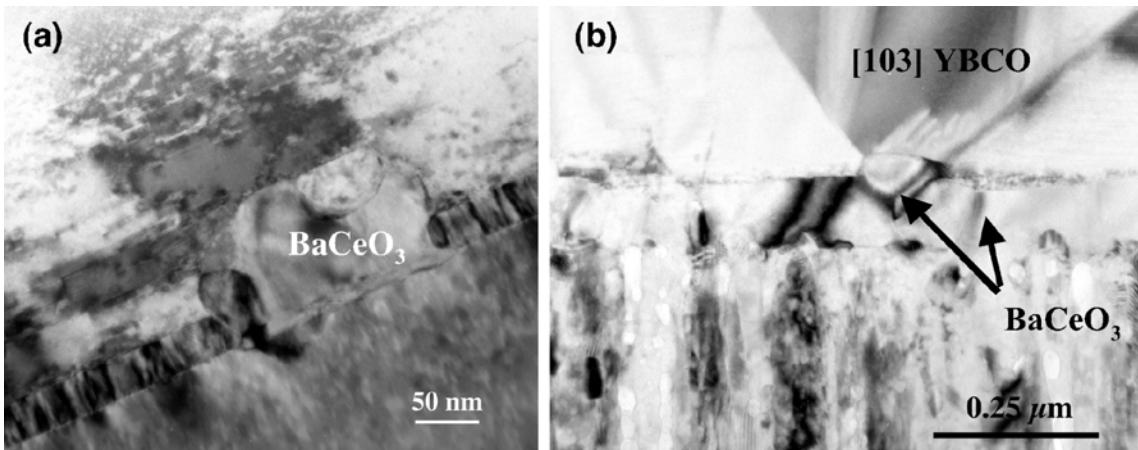
Fig. 29. TEM micrographs of examples in which (a) the alignment of the YBCO was not affected by the formation of $BaCeO_3$ during the interfacial reaction and (b) a [103] oriented YBCO grain that nucleated on a $BaCeO_3$ grain at the interface.
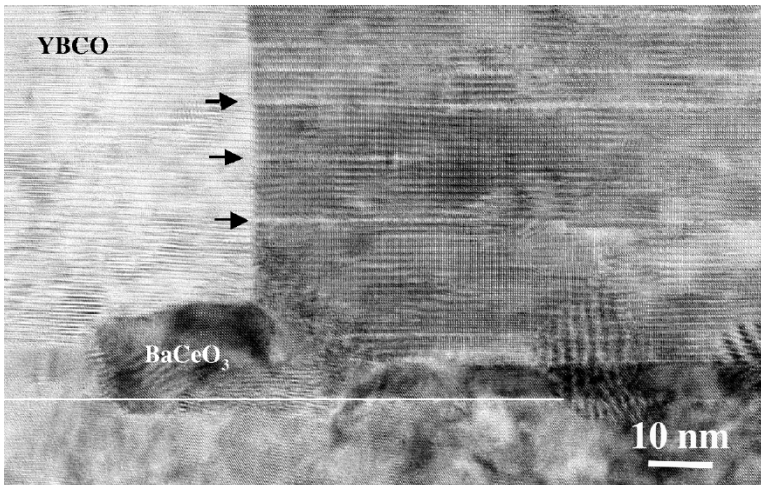
Fig. 30. TEM micrograph of an incomplete interfacial reaction. Material left over from the reaction to form $BaCeO_3$ diffuses along the grain boundary and intercalates as intergrowths of $Y_2Ba_4Cu_7O_y$ and $Y_2Ba_4Cu_8O_y$. The white line is a guide to the eye to locate the discontinuity in the ceria layer and the resulting interfacial reaction that formed $BaCeO_3$.

It is clear from the above discussion that eliminating substrate defects will reduce the number of interfacial reactions between the YBCO and underlying buffer layer. A second way to reduce the interfacial reactions is to optimize the thickness of the underlying buffer layer, which in this case is ceria. Shown in Figs. 31a and b are plots of the critical current density (J_c) as a function ceria thickness for YBCO films deposited on IBAD YSZ-coated metal substrates and YSZ single-crystal substrates. This maximum in J_c in both cases correlates with a minimum in the reactivity between the ceria buffer layer and YBCO film. The critical ceria layer thicknesses on the IBAD YSZ metal tapes and single crystals were approximately 90 Å and 200 Å, respectively. The maximum J_c value reached with a 90 Å ceria film on a metal substrate and a 1.5 μm YBCO film was 1.7 MA/cm^2 at 75 K and self-field. A maximum J_c value of 2.9 MA/cm^2 was reached for a 1μm thick YBCO film on a single-crystal YSZ substrate with an intervening 200 Å ceria buffer layer.
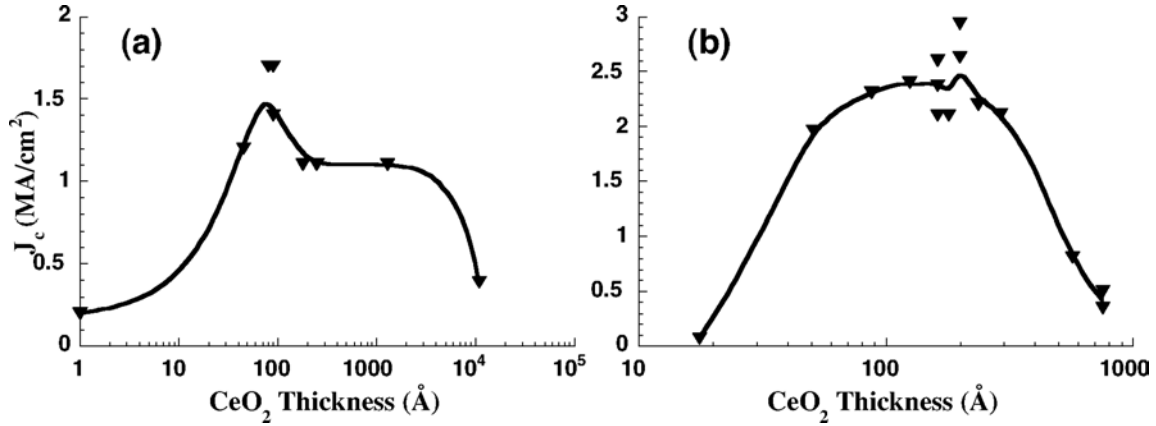
Fig. 31. Plot of the J_c values as a function of the thickness of the buffer layer beneath the YBCO film for (a) IBAD YSZ templates and (b) single-crystal YSZ substrates. The thickness averages of the YBCO films were 1.5 and 1.0 μm, respectively.

At the critical thickness, the interfacial reactions were found to be almost non-existent as shown in the example of a single-crystal substrate in Fig. 32. In contrast, relatively small increases or decreases in the thickness of the ceria buffer layer relative to the optimal thickness induced significant interfacial interactions. Shown in Fig. 33 are cross-sectional and plan view TEM images of YBCO films on a single-crystal substrates where the intervening ceria buffer layer of thicknesses were 560 and 800 Å, respectively. The corresponding J_c values in the 1 μm thick films were 0.8 and 0.35 MA/cm^2 at 75 K and self-field. In the cross section (Fig. 33a), the reactions are observed to be nearly continuous along the interface. The plan view image shown in Fig. 33b was taken with the beam nominally parallel to the [001] direction in the film and substrate. The areas of the micrograph that exhibit a bright contrast are YBCO grains that are misaligned relative to the desired alignment of [001] YBCO || [001] of the ceria || [001] of the YSZ single crystal. It has been found that the density of misaligned grains increases as the severity of the interfacial reactions increases.

In the case of metal substrates and the optimal ceria thickness, the few areas of significant interfacial reaction that were found could be traced to the propagation of defects from the substrate. Such was the case for the samples in Figs. 28b and 30, which had ceria thicknesses of approximately 90 Å and a J_c value of 2.9 MA/cm^2. The underlying reasons for the increased stability of the ceria buffer layer for certain optimal thicknesses is unclear at this point. Possibly an optimized stress state is obtained in the ceria buffer layer for a certain thickness as it bridges the lattice mismatch between the

YSZ and the YBCO films. The polycrystalline nature of the IBAD template may explain the factor of two decrease in the optimal thickness of the ceria buffer layer when compared to the results on single crystal substrates. However, the overall results are clear. Significant enhancements in J_c (up to 55% in the present work on IBAD YSZ templates) can be obtained in YBCO films when the thickness of the underlying buffer layer is optimized. In addition, many more defects in the YBCO films can be eliminated through a careful choice of substrate preparation conditions that reduce or eliminate substrate irregularities. Hence, one has the means to control and engineer the structure of a coated conductor in order to optimize its transport properties.
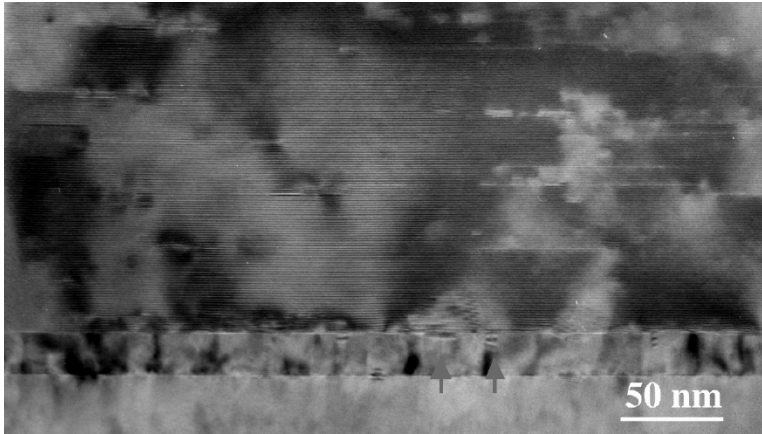
Fig. 32. TEM micrograph of the interface of a 1 μm thick YBCO film on a single-crystal YSZ substrate with an intervening 200 Å thick ceria buffer layer. Only a few nano-sized interfacial reactions products could be found along the interface as indicated by the arrows above. The J_c value of the film was 2.9 MA/cm^2 at 75K and self-field.
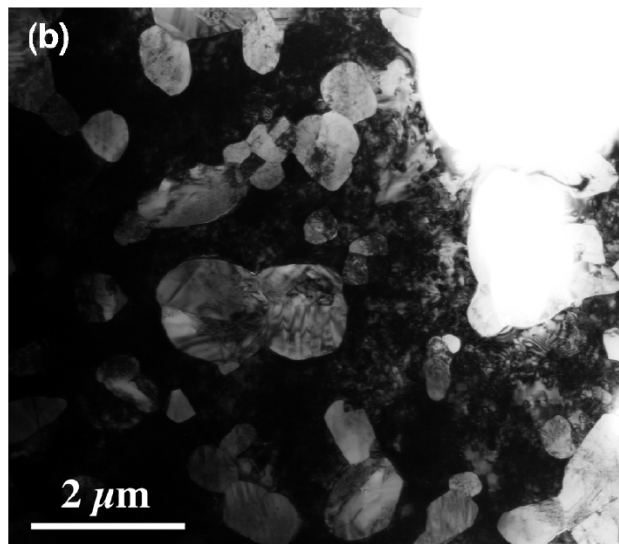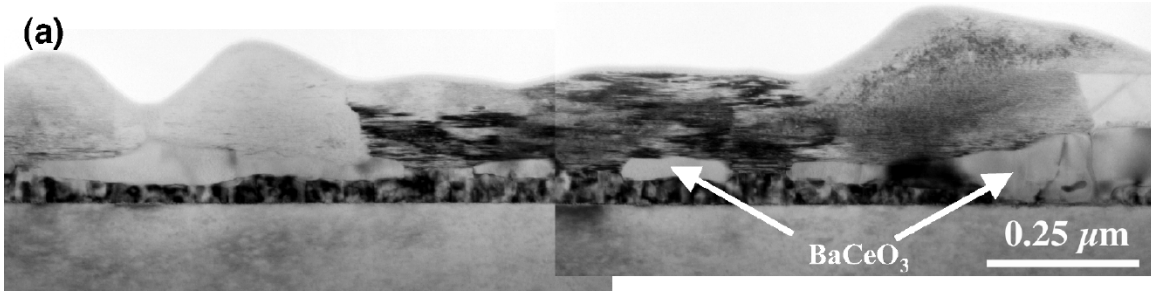
Fig. 33. TEM images of samples with YBCO films on single-crystal YSZ substrates with intervening ceria buffer layer thickness of (a) 560 Å and (b) 800 Å. The corresponding J_c values were 0.8 and 0.35 MA/cm^2. The cross-section in (a) shows a continuous interfacial reaction layer between the ceria and YBCO. The plan-view TEM image of (b) shows the misaligned YBCO grains in the film. The latter image was taken with the beam parallel to the [001] direction of sample. The areas of the sample that appear bright in the image are not aligned in this manner.

In conclusion, the roles that substrate defects and interfacial reactions play in the development of defects in YBCO films on IBAD YSZ templates and single-crystal YSZ substrates were examined. Substrate defects can propagate through the intervening buffer layers and affect YBCO film growth. Hence, the preparation of the substrate surface prior to film deposition is a critical parameter in the fabrication of high-J_c coated conductors. The thickness of the buffer layer immediately beneath the YBCO film can also be used to control the severity of the interfacial reactions. Optimal ceria thickness of 90 Å and 200 Å were found for the IBAD YSZ templates and YSZ single-crystal substrates, respectively. The use of the optimal ceria thickness significantly reduces the interfacial reactions and enhances the J_c values of the YBCO films. In the case of IBAD YSZ templates, the use of the optimal 90 Å thickness resulted in a 1.5μm thick YBCO film having a J_c level of 1.7 MA/cm^2. Likewise, an optimal ceria thickness of 200 Å on a single crystal YSZ substrate was used to produce a 1μm thick YBCO film with a J_c level of 2.9 MA/cm^2. These results show that it is possible to control the development of the structure of the coated conductor during processing for enhanced J_c values.

2.1.5 A New LANL Facility for Coated Conductor Fabrication, Characterization, and Applications

V. Matias, B.J. Gibbons, L.E. Bronisz, A.T. Findikoglu, S. Kreiskott, R.F. DePaula, R. Bramlett, R. Edwards, S. Ashworth, L. Civale, J.Y. Coulter, J.O. Willis, P.N. Arendt, J.R. Groves, S.R. Foltyn

The STC's Los Alamos Research Park (LARP) laboratories will be a national facility intended to demonstrate feasibility of continuous fabrication of high-quality HTS coated conductor (CC) tape using technologies already proven to produce smaller batch samples. This effort will provide an opportunity for accelerated development of 2nd generation HTS wire and its applications. The specific goals are to produce superconducting tapes of 10 m lengths, carrying over 100 A at 75 K, and to demonstrate their use in prototype applications. LANL staff, in collaboration with external partners, will do the work in this facility.

The LARP facility is a 10,000 sq ft area divided into 7 labs, 14 offices, and a reception area. The offices are for LANL staff as well as outside collaborators. At present 7 persons are full time at the Research Park, in addition to several students and 3-4 staff who spend part of their time at the Research Park. Fig. 34 shows an exterior view of the Research Park building. Fig. 35 shows a schematic layout of the labs in this building. Fig. 36 shows the progress of installing laboratory apparatus and Fig. 37, two of the finished labs.

Fig. 34. Exterior view of the Los Alamos Research Park building
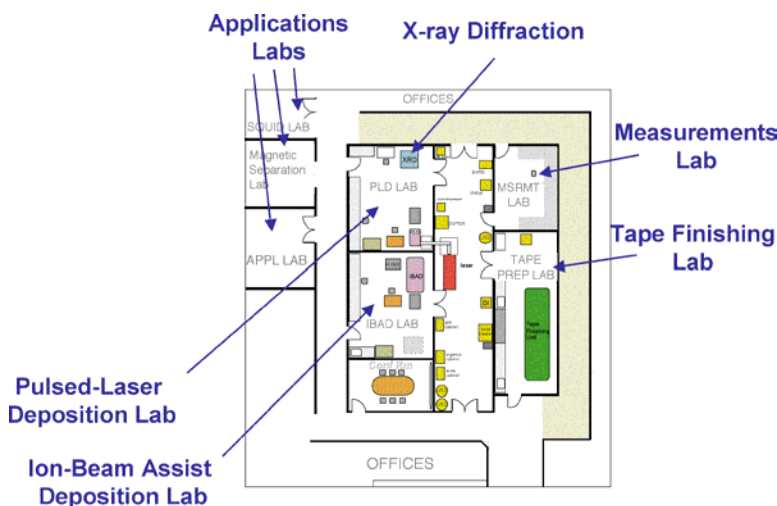
Fig. 35. Schematic of the STC suite at the LARP.

Fig. 36. Clockwise, from upper right: installation of the tape polishing unit, moving the IBAD chamber through the laboratory door, the IBAD chamber in place, and moving the 200 W industrial laser into the

Fig. 37. Left - IBAD chamber and electronics racks and right – PLD chamber installed at the LARP laboratories.

During this year the facility was set up and became operational. The dual activities of CC fabrication development and applications research have internal as well as external components. Foremost, it is to be a leading CC research facility. STC's Research Park Labs will be performing research and development work that moves the superconducting community towards manufacturing of CC tape. As a national center it will also facilitate collaboration and coordinate research among universities, national labs, and companies. In addition, by providing a collection of state-of-the-art equipment for CC development and making it available to outside users, this will also be a unique national user facility. It

will be the first and most complete open facility to encompass a whole line of activities from CC fabrication to characterization and applications development.

The major accomplishments during the fiscal year 2002 include:
The metal finishing line is operational and has been producing tens of meters of tape with RMS surface roughness of < 1nm on 5 μm scans.
The IBAD system has been set up and is producing meters of IBAD-MgO templates (Δφ ~ 12°) on metal tapes.
The PLD system has been set up and is producing superconducting YBCO films continuously on metal tapes.
The electrical characterization system has demonstrated reel-to-reel critical current measurement results.

Coated conductors require starting with metal tape substrates with smooth, clean surfaces. To achieve this goal a custom industrial-type machine has been purchased to electropolish the metal tapes. The unit is capable of reel-to-reel polishing up to 100's of meters of tape at high speeds. The system is very versatile and has the capability to be used for tape finishing research, including electroplating. The system is shown in Figs. 38 and 39.

Fig. 38. Left – tape finishing system; right – comparison of unpolished and electropolished tapes.
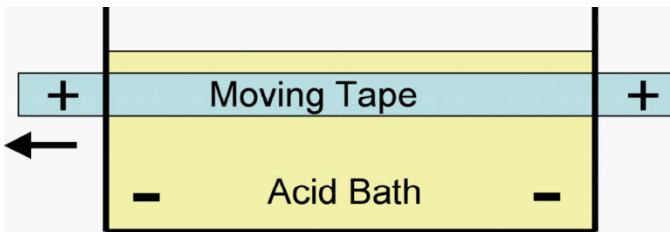
Fig. 39a. Schematic of electropolishing cell.
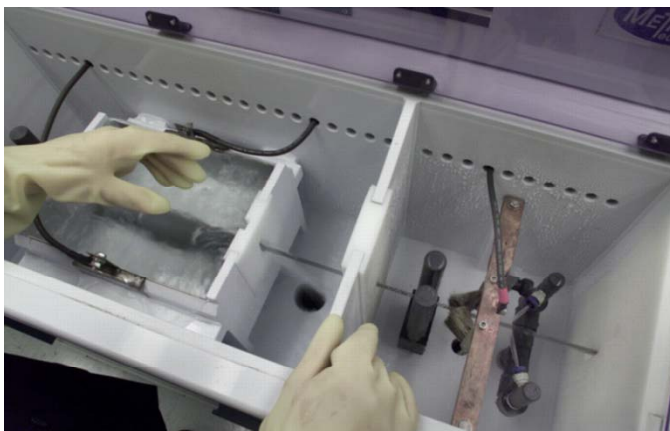
Fig. 39b. View of electropolishing cell, showing brushes on the right side and electrodes, tape, and solution on the left.

The results of polishing the metal tapes are shown in the next two figures. On a coarse scale (Fig. 40), electropolishing results in an RMS surface finish of 8 nm, 50% better than that of the mechanically polished substrate. More importantly, on a much finer scale (Fig. 41), not only was the surface finish markedly better, but the largest slopes observed in line scans were an order of magnitude smaller than for mechanical polishing. With these small angle inclines, there should be almost no effect on the intergranular current transfer, while this could be a much more significant problem for the mechanically polished tape.
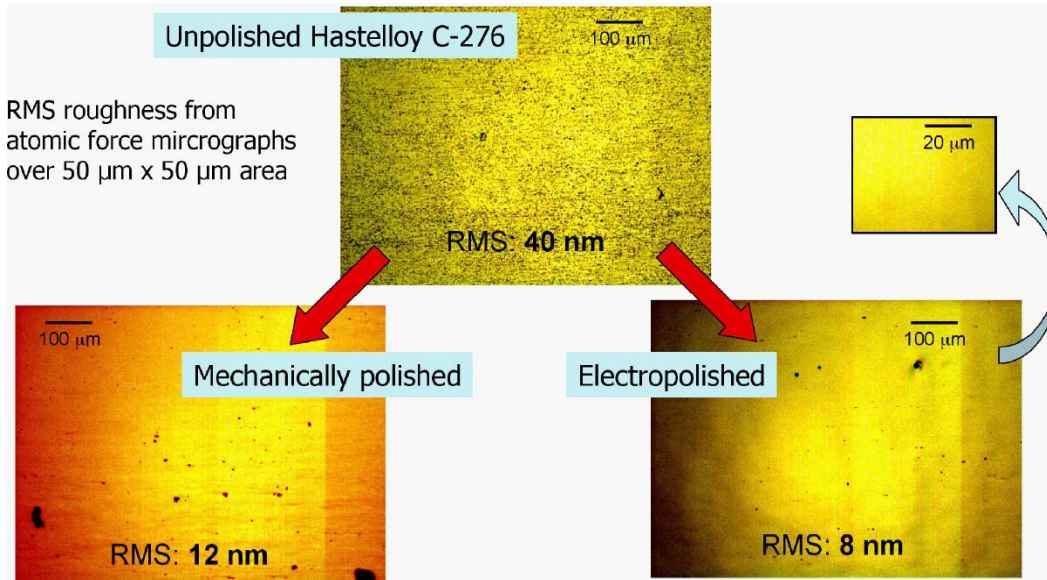
Fig. 40. Results of atomic force microscopy measurements over large areas (50 x 50 µm) of metal tape substrates.
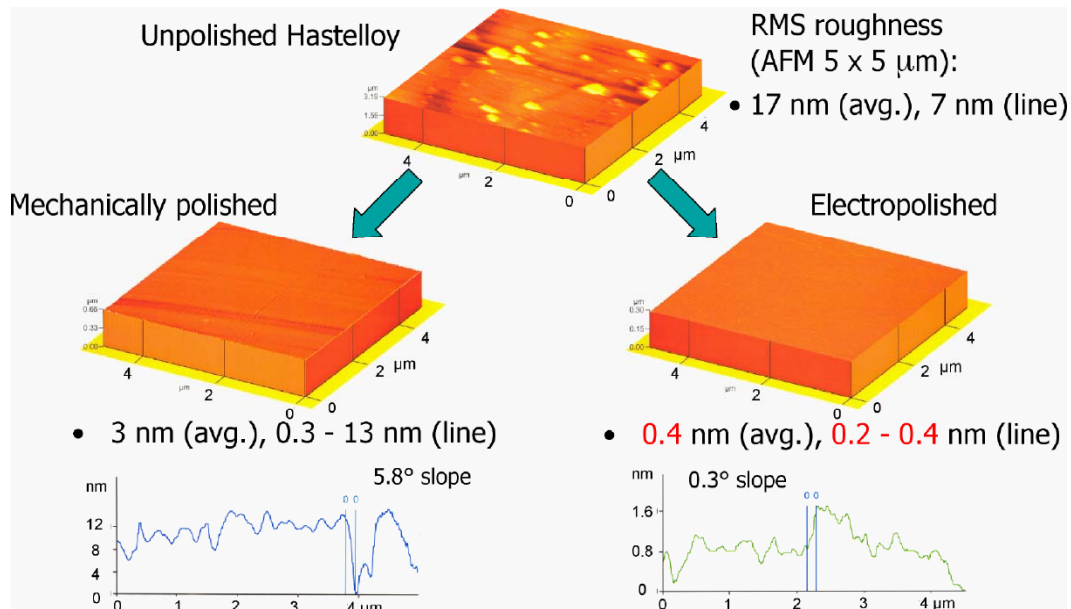
Fig. 41. Improvements in surface finish with electropolishing measured at high resolution. The line trace at left bottom for the mechanically polished substrate shows a very sharp 5.8° slope in the profile, which could result in a high angle grain boundary and low critical current in the YBCO conductor. In contrast, the electropolished substrate had a slope of 0.3°, which is not a concern for grain boundary current transport.

After the tape has been polished, the next process step is to deposit the template layer by ion beam assisted deposition (IBAD). In the LANL process, MgO is used as the IBAD template layer because very good in-plane alignment can be achieved very quickly, essentially upon nucleation of grains (10 nm thickness). This is in sharp contrast to the case of yttria-stabilized zirconia (YSZ), the other commonly used template layer, which requires layer thicknesses approaching 1 μm. Because thickness if proportional to time, this is a very slow process.

The IBAD chamber is shown schematically and pictorially in Fig. 42. The large (6' x 4' by 3.5' [183 x 122 x 107 cm^3]) vacuum chamber is designed for flexibility and access. With a pumping speed of 3000-6000 l/s, it is designed for quick turn around: it can be pumped down in a few hours and vented in 20 minutes. It can handle > 100 m lengths of tape on the reel-to-reel tape transport system. The chamber is adaptable for process integration, such as deposition of both the IBAD-MgO layer and buffer layers. The MgO is evaporated from one of the two electron beam guns with four hearths each near the floor of the chamber. The ion gun is located at the back of the chamber and directed such that the Ar ions impinge on the substrate at the appropriate angle. The tape is transported on reels through the deposition zone from right to left. The reflection high-energy electron diffraction (RHEED) source with widely spaced coils and detector are located close to the plane of the tape.
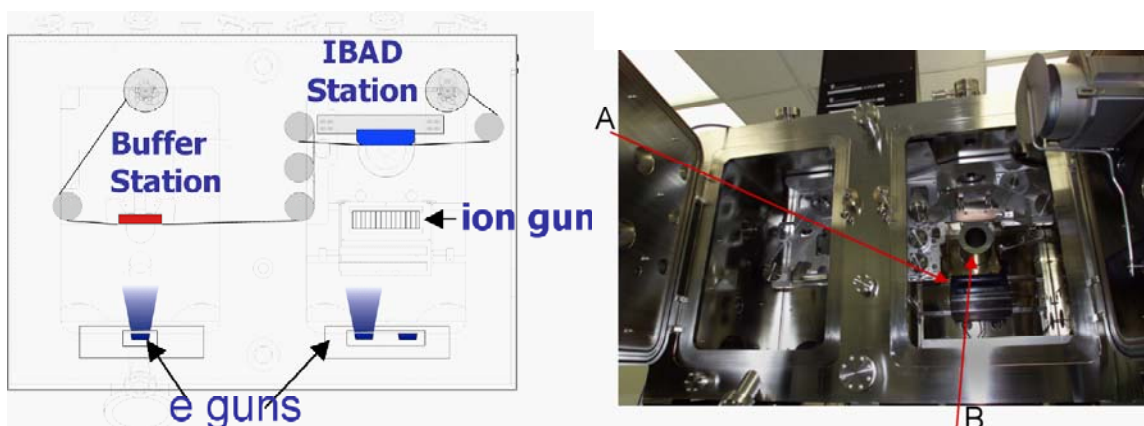
Fig. 42. Left – schematic of the IBAD chamber. Right – Photograph of the IBAD chamber with arrows indicating A – the ion gun, and B – the RHEED source.

All of the coated conductor fabrication steps at the Research Park are designed for continuous tape processing and allow the exploration of process parameters in a sequential way. The position on a tape can be tracked from one process step to the next so that a matrix of experiments, either in continuous or stationary (batch) mode, can be developed. This kind of combinatorial research provides the capability of performing hundreds of experiments on one reel of tape with very high throughput. This technique is being used to optimize the IBAD deposition process, and has aided in the transfer of this process from the 1-meter loop IBAD research system. An example of samples in the combinatorial approach is shown in Fig. 43.

In-situ RHEED is critical for development of the IBAD-MgO texturing process. RHEED provides information on structure of the film during growth, in real time; on texture development of the film; on the optimum MgO thickness; on out-of-plane crystallographic tilt; and on grain size. The IBAD system employs parallel scanning

RHEED for continuous IBAD (Fig. 44). By scanning the RHEED beam along the tape, images of the RHEED pattern at different stages of IBAD growth can be obtained.
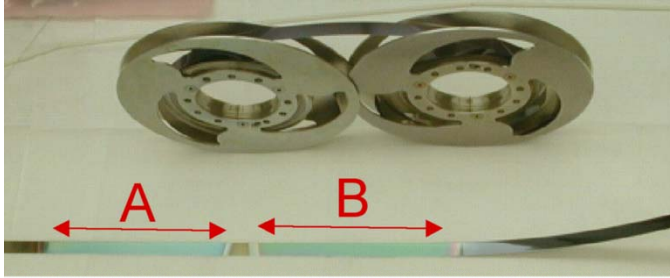
Fig. 43. Reels of metal tape in background. In foreground, A and B have different buffer layers on top of the IBAD-MgO template film.

As mentioned earlier, the IBAD chamber has two deposition stations, shown in Fig. 45, the IBAD station on the right with the RHEED gun and screen, and the buffer station on the left for non-ion beam assisted deposition of other buffer layers, such as homoepitaxial MgO, YSZ, and CeO$_2$. Because it is possible to translate the tape in either direction, the RHEED system can be used to monitor quality for films grown at either station. Representative RHEED patterns are shown in Fig. 46.
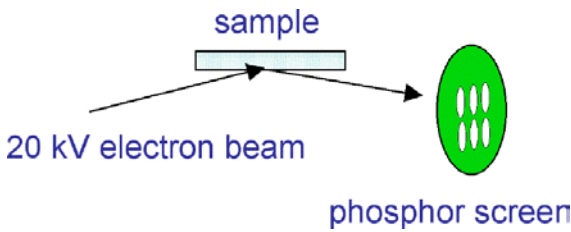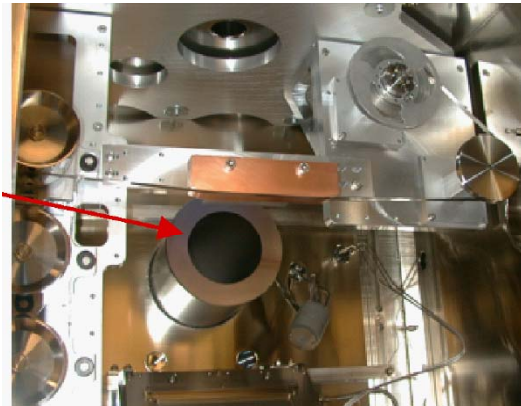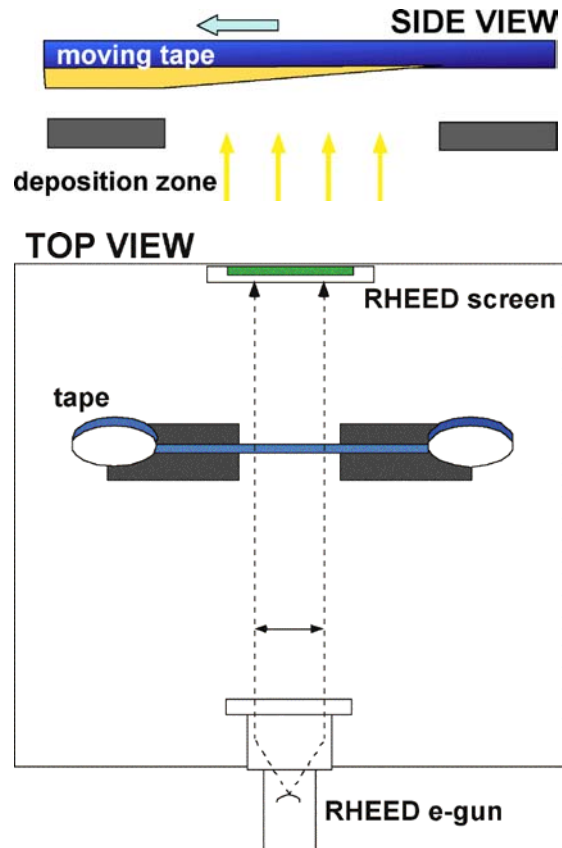
Fig. 44a. Schematic of the operation of the RHEED system. Fig. 44b. Photograph showing the RHEED gun (red arrow).

Fig. 44c. Schematic Side and Top views of the tape transport and RHEED system.
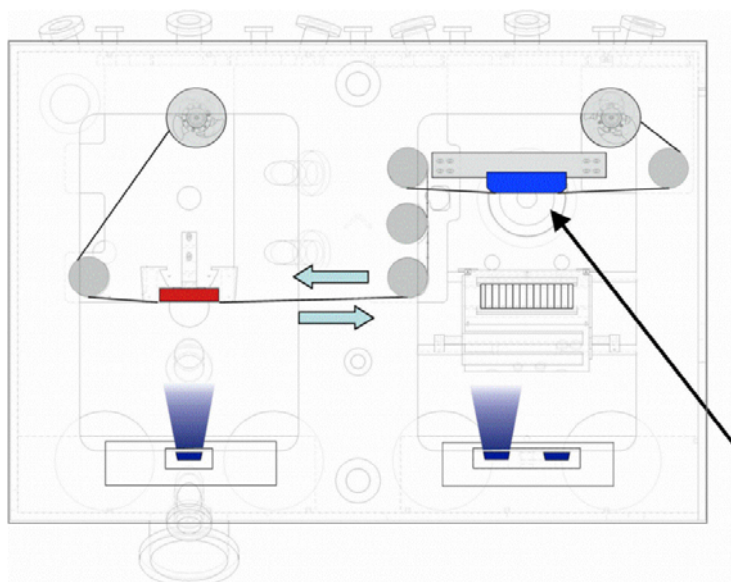
Fig. 45. Illustration of translation of the tape in either direction to the IBAD/RHEED station (right) or the buffer station (left). The arrow points to the RHEED gun used for quality control analysis.
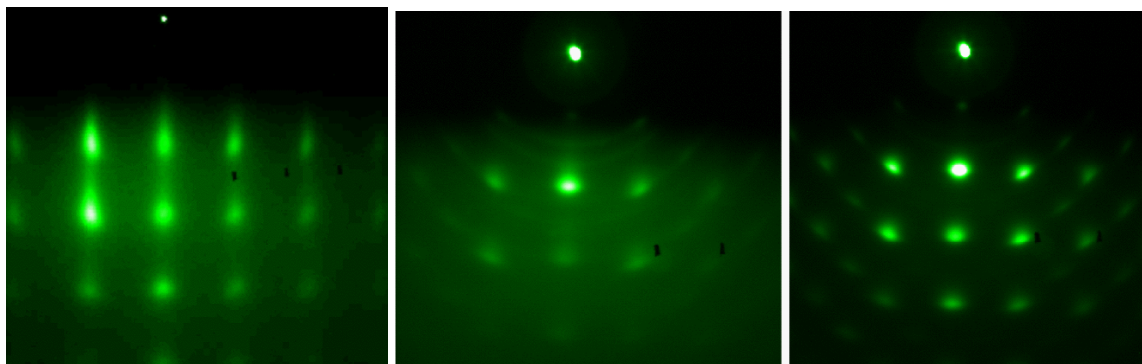
Fig. 46. RHEED images of buffer layers deposited and measured in the IBAD chamber. Left to right: IBAD-MgO, YSZ on MgO, and CeO_2 on YSZ.

The next stage in the coated conductor fabrication process is the pulsed laser deposition (PLD) of any required buffer layer and of the YBCO. The chamber is shown in Fig. 47. It is relatively large (4' x 3.5' x 2' (120 cm x 107 cm x 60 cm)) with easy access via front and side doors. It has a 4000 l/s pumping system that pumps down the chamber in one hour. It employs a 200 W XeCl laser operating at 308 nm for PLD. The multi-target manipulator holds four 4" (10 cm) targets for PLD of various buffer and HTS layers. The quartz lamp tape heater provides any required heating of the tape as it moves continuously through the PLD zone. *In-situ* adjustment of the tape position with respect to the laser plume can be made to optimize the deposition process. Silver sputter deposition is also integrated into the chamber.
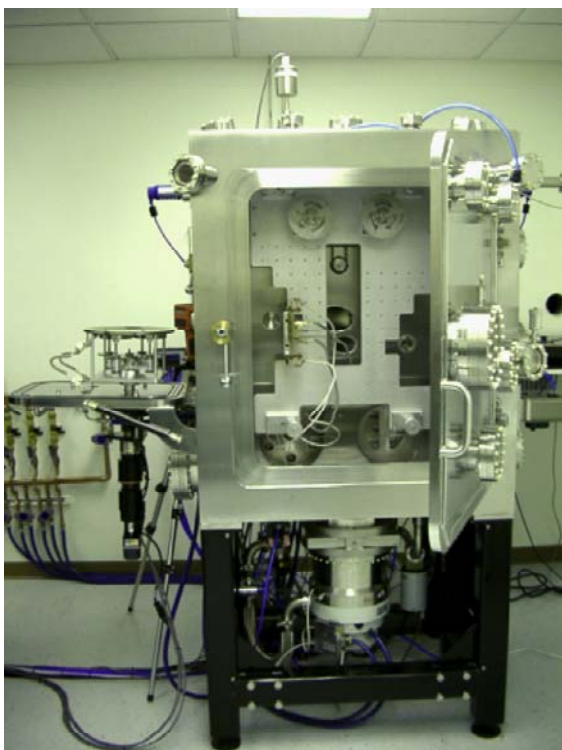
Fig. 47a. Photograph of the PLD chamber. The laser beam enters from behind the chamber on the right. The tape transport reels (top and bottom), the tape heater assembly (left inside door edge), and the target holder (pivoted out of the chamber on the left) are visible.
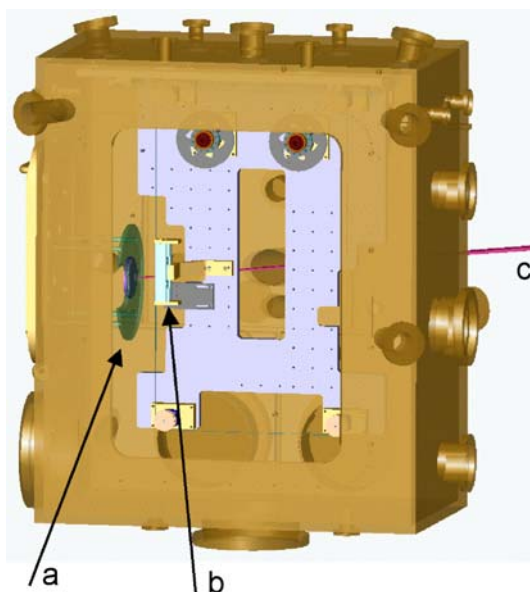
Fig. 47b. Schematic of PLD chamber. a points to the multitarget manipulator, b to the tape heater, and c represents the laser beam entering the chamber from the right rear.

This PLD chamber has produced high quality YBCO films on single-crystalline substrates, such as $SrTiO_3$. Fig. 48 shows an x-ray diffraction pattern and a sharp superconducting transition by a four-wire transport technique for one of these films. In addition to these results on single-crystalline substrates, continuous deposition of YBCO on tape has been demonstrated.
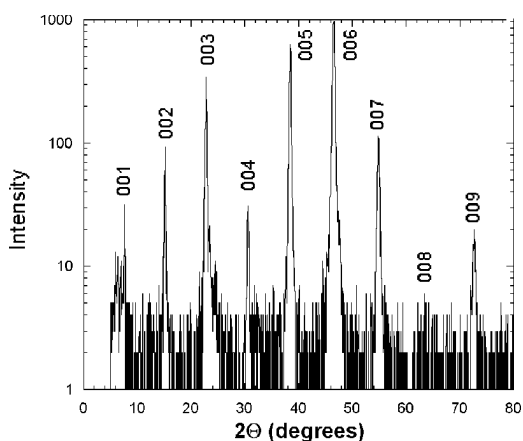
Fig. 48a. X-ray diffraction pattern of YBCO on a single-crystalline $SrTiO_3$ substrate.
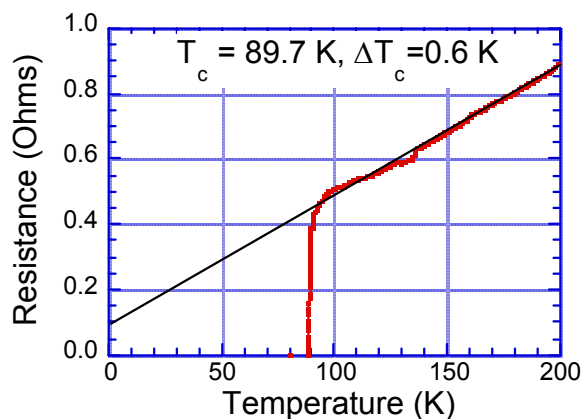
Fig. 48b. Sharp superconductive transition measured resistively on a YBCO film on a single-crystalline $SrTiO_3$ substrate

One of the major diagnostic tools used to determine coated conductor phase content and crystallographic orientation is the Bruker D8 Discover X-ray Diffraction apparatus (Fig. 49). This system makes use of a 2-dimensional Position Sensitive Detector and the GADDS (General Area Detector Diffraction System) for rapid acquisition of x-ray diffraction peaks. It has an x-y stage and a minimum spot size of 10 μm. Fig. 50a shows an x-ray diffraction pattern of YBCO on a metal tape sample from the LARP. Fig. 50b shows the pole figures deduced from an x-ray diffraction texture analysis. This sample was prepared in the IBAD system at the LARP. It consists of a 550 Å CeO_2 layer on top of YSZ-buffered IBAD-MgO on metal tape. The quite respectable in-plane texture derived from the pole figure is 12° FWHM (full width at half maximum).

Fig. 49. Two views of the BrukerD8 Discover X-Ray Diffraction apparatus at the Research Park.
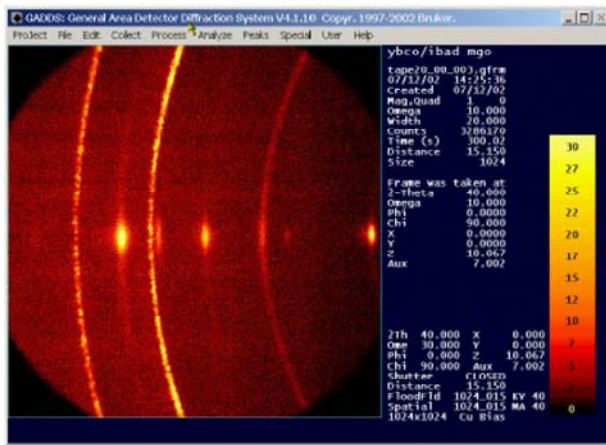
Fig. 50a. X-ray diffraction pattern of LARP-fabricated YBCO on metal tape from Bruker system
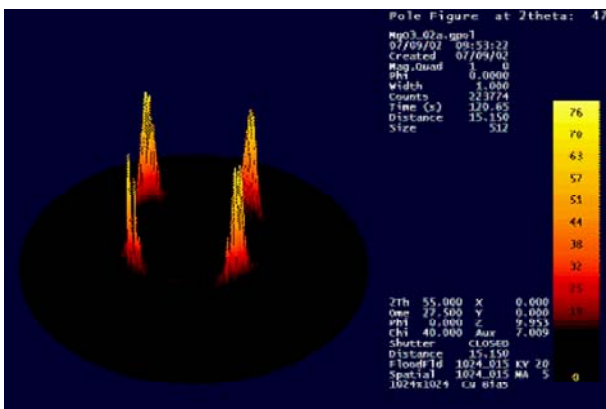
Fig. 50b. Pole figure analysis of IBAD MgO template film with YSZ and CeO_2 buffer layers. The in-plane texture is 12° FWHM.

Electrical property measurement systems have also been developed at the Research Park. A reel-to-reel (continuous measurement) system (Fig. 51a) is available for measuring position-dependent critical current I_c of the coated conductor tapes by contact (transport I_c) or by non-contact techniques. Specifically, an ac inductive technique operating at 2 kHz using both the first and third harmonics to determine I_c has been implemented (Fig. 51b). Data collection here will be integrated with the sample preparation database.
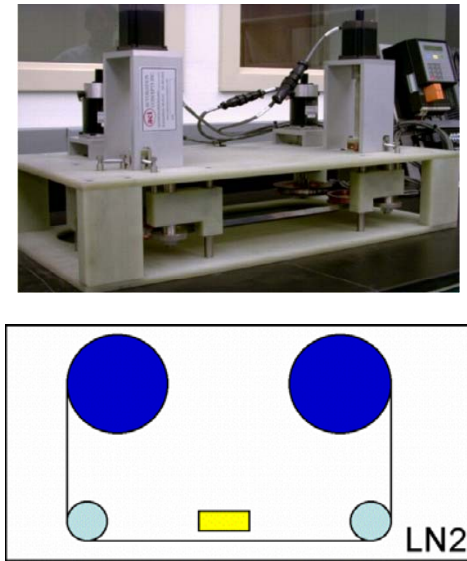
Fig. 51a. Photograph and schematic of reel-to-reel measurement system for low temperature electrical measurement.
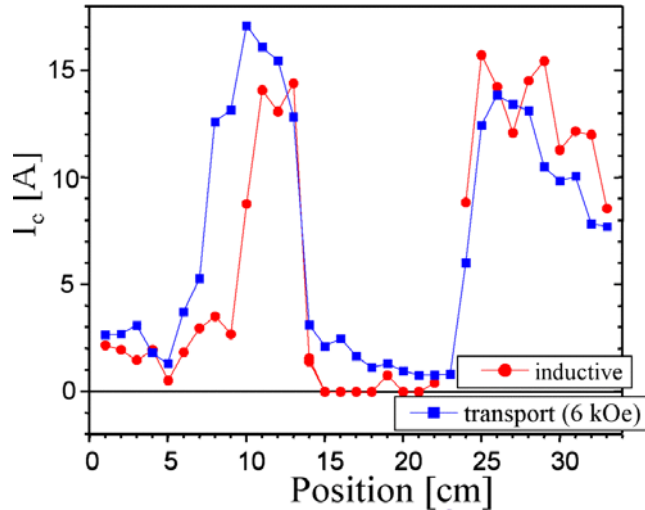
Fig. 51b. Comparison of transport and ac inductive measurement of a coated conductor sample in the reel-to-reel measurement system.

Also established at the Research Park is a program to address some of the issues related to the use of coated conductors in power applications. Most of these applications require the conductor to carry ac current, to be in an ac magnetic field, or both, or to be subject to dc fields and currents with ac ripple components. Therefore, the reduction of ac losses in CC is important for operational efficiency. The ac losses in a typical coated conductor near I_c are comparable to that of Bi-2223/Ag composite tapes. For example, for an I_c of 60 A and peak current of 90% of I_c, the loss is 0.3 mJ/cycle/m, the "Virgin" value of Fig. 52. The goal of this program is to reduce the losses without increasing the \$/kA-m. This is done by managing the entry of magnetic field into the CC tape in a number of different ways (A-D) in Fig. R. It was possible to reduce the losses to approximately 30% of the virgin CC. A patent application has recently been submitted for this technique.
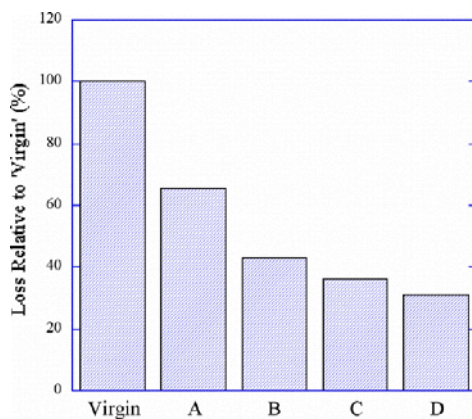
Fig. 52. Reduction in losses in coated conductors using various techniques to manage the entry of magnetic field into the material.

44

To summarize the results of the Accelerated Coated Conductor Initiative during this fiscal year, Los Alamos set up several laboratories at the Research Park for CC fabrication and characterization. The electropolishing system has been optimized to polish tape at up to 30 m/h with a surface roughness of <1 nm RMS over a 5-µm area. The IBAD system has been used to prepare multiple meters of IBAD-MgO templates with in-plane texture of 12° FWHM and out of plane texture of 2.7°. These were deposited at speeds of 6 m/h with buffers deposited at similar tape speeds. The PLD system has been used to deposit YBCO continuously on single-crystal and metal tape substrates.

In-situ RHEED was used for process optimization and quality control of the IBAD-MgO process. This was done in conjunction with a combinatorial approach for optimizing various parameters. The new Bruker x-ray diffraction apparatus with large area detector was installed and used to characterize crystallographic phases and textures of samples produced at the Research Park. Methods to reduce the ac losses of coated conductors carrying ac transport currents were developed.

The initiative also resulted in many collaborations being established this year. Cooperative Research and Development Agreements (CRADAs) have been established with IGC-SuperPower and with DuPont. Argonne, Brookhaven, and Oak Ridge National Laboratories have all committed to working at the Research Park. Lawrence Berkeley and Sandia National Laboratories, University of Wisconsin, Stanford University, University of Kansas, Wright Patterson Air Force Base, American Superconductor Corporation, and 3M Company have all expressed interest in collaborative work at the Research Park. A DOE-sponsored Superconductor Partnership Initiative (SPI) project on magnetic separation with DuPont is ongoing and a DuPont postdoc is stationed and performing R&D at the Research Park. The LARP has established an environment for new partnerships with industry, universities, and national laboratories. There are opportunities for user facility agreements and opportunities for interaction and sample supply for the Air Force-sponsored MURI Program, especially scanning techniques for local dissipation measurement.

Future plans include the completion of the system integration and process control on the fabrication systems - set up for ease-of-use and sample tracking. The additional *in-situ* diagnostic of ion scattering will be added to the IBAD system. Our near term target is to achieve performance of IBAD-MgO coated conductors with MgO in-plane texture <8° and I_c >50 A on 1-cm wide, long-length (> 5 m) tape. We plan to establish a User Facility Program with a User Advisory Committee, incorporating at least 5 outside members. For power applications development, we plan to establish an applications testing lab with capabilities of 5000 A dc and ac (variable frequency 30 to 800 Hz) for testing cables and other power device components. Targets for this laboratory at the Research Park include fabricating a 10 m CC coil and a 1000 A one-meter long CC cable and evaluating their ac and dc performance.

In conclusion, the expanded effort at Los Alamos is an aggressive program for Coated Conductor scaled-up fabrication with the goals of: (1) high-throughput sample preparation and characterization in continuous reel-to-reel processing; (2) achieving longer lengths of coated conductors; and (3) *in-situ* and real-time process diagnostics capability. The tape fabrication processes are currently operational. The applications lab is being set up for testing and evaluation of coated conductors and prototype applications. The user facility, training, and sample exchange will be available in the next year.

2.1.6 The Early Stages of the Microstructural Development of the Colony Structure in Bi-2223 Tapes

T.G. Holesinger and acknowledging the Wire Development Group (AMSC, ANL, ORNL, U. Wisc.)

It is commonly held that most of the transport current in Bi-2223 tapes is carried close to the silver interface. Hence, it is of interest to document this particular microstructure and determine the conditions during processing that shape its development. The overall structure in fully processed tapes has been documented by electron microscopy as well as by *in-situ* neutron and synchrotron x-ray diffraction. Only a few of the electron microscopy studies have focused on the through-process microstructure development while *in-situ* XRD and neutron studies suffer from a lack of spatial resolution in tracking phase development within the filaments as a function of position. In this study, phase, microstructure, and composition development in Bi-2223 tapes were examined. An emphasis was placed on detailing the structure and composition of the Bi-2223 development during the initial stages of processing.

Multifilament Bi-2223 tapes at various stages of processing were examined by analytical electron microscopy. The starting composition of the Bi-2223 powder used in the 19-filament tapes was $Bi_{1.7}Pb_{0.3}Sr_{1.9}Ca_{2.0}Cu_{3.0}O_y$. All of the tapes used in this work were processed at 827°C in 8% O_2/N_2. After ramping up to the processing temperature, the Bi-2223 tapes were held for a short dwell time and then quenched into an oil bath. The dwell times were 0, 10, 100, 300, 400, 500, and 640 minutes. The critical current densities (J_c) of fully processed tapes from this series of samples reached 70 kA/cm^2 at 77 K and self-field.

These tapes were examined from three principle directions of view in scanning and transmission electron microscopes (SEM and TEM): short transverse section, longitudinal transverse section, and plan view. Final TEM and SEM specimen preparations were accomplished with dimple polishing and ion-milling. Compositional measurements were performed in the TEM using energy dispersive spectroscopy (EDS). Standards consisted of amorphous Bi-2212 and Ca_2PbO_4.

The development of the microstructure and alignment in Bi-2223 tapes starts with the initial rolling and ramp up to temperature as indicated by the micrographs in Fig. 53. The as-rolled tape consists of several sub-micrometer sized precursor phases of $Bi_2Sr_2CaCu_2O_y$ (Bi-2212), alkaline-earth cuprates (AEC's), and CuO as shown in Figs. 53a and c. Interfacial roughness between the silver and BSCCO arises during the rolling stage as shown in Fig. 53a, but appears to be smoothed out by the rapid grain growth that occurs during initial heating. Figs. 53b and d show the resulting microstructure of Bi-2212, $(Sr,Ca)_2CuO_2$ (2:1 AEC), and $(Sr,Ca)_{14}Cu_{24}O_{41}$ (14:24 AEC) that develops during the thermal ramp. The Ca-rich 2:1 AEC phase assumes a needle-shaped morphology that can exceed 10 μm, while the $(Sr,Ca)_{14}Cu_{24}O_{41}$ (14:24 AEC) develops as a blocky phase 1-2 μm in size.
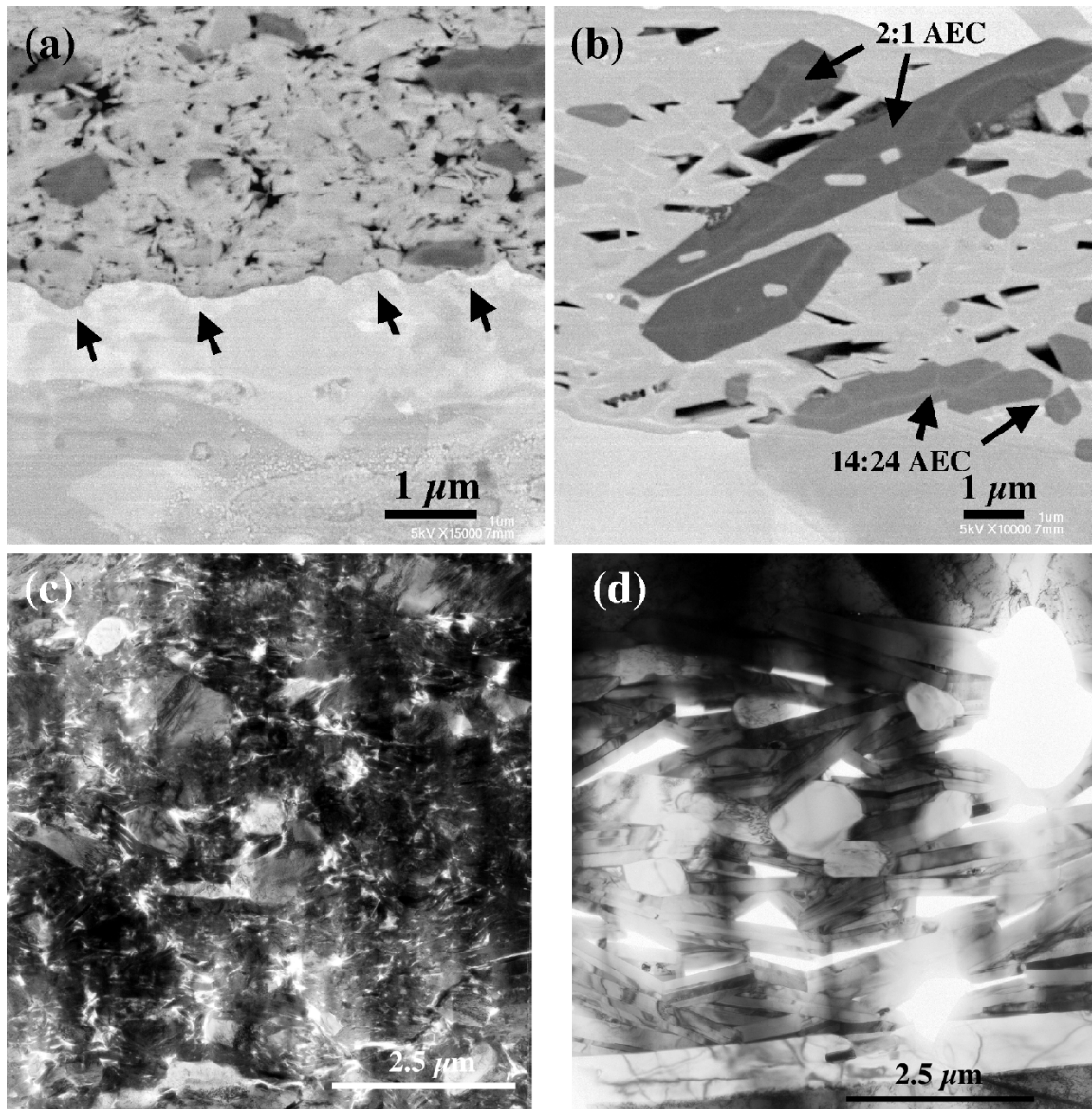
Fig. 53. Comparison of the changes in the microstructure between the as-rolled Bi-2223 tapes, (a) SEM and (c) TEM, and the microstructure of the tapes quenched after ramping up to the processing temperature of 827°C, (b) SEM and (d) TEM.

Defects that can affect the formation of the Bi-2223 colony structure can arise in these early stages of processing. The rolling process severely distorts and even amorphizes the Bi-2212 phase as shown by the grain bending, basal plane defects, and regions of amorphous material in Fig. 54a. This accumulation of damage is one reason for the rapid and somewhat uncontrolled growth of the Bi-2212 phase during the early stages of heat treatment. Rapid grain growth is also observed with the crystallization of amorphous Bi-2212 glasses. The initial texture imparted by the rolling process and the presence of the silver sheath can partially control the development of the Bi-2212 phase. However, other defect structures in the tapes can also affect the recrystallization of the Bi-2212 phase. The AEC's provide nucleation sites for the alignment and growth of the Bi-2212 phase as indicated in Fig. 54b.
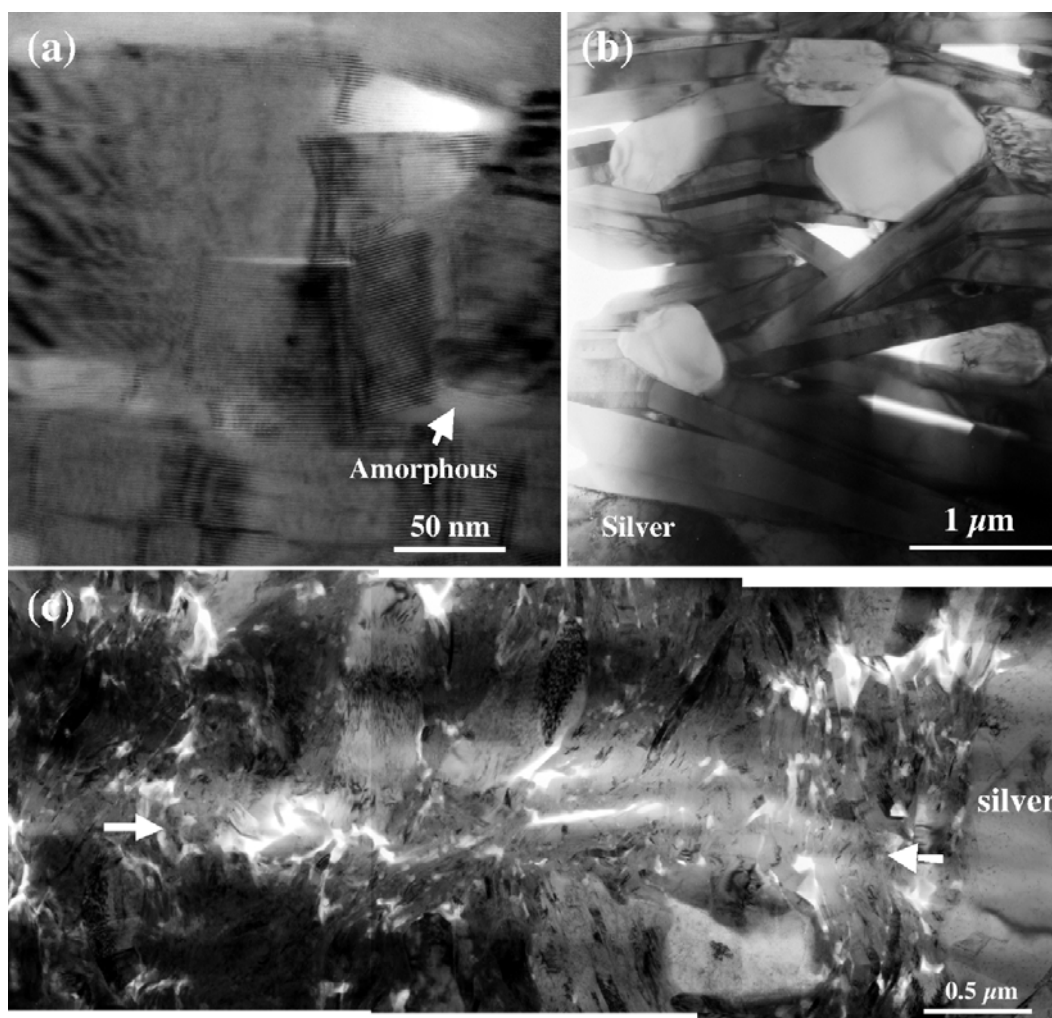
Fig. 54. TEM micrographs of (a) highly-deformed Bi-2212 grains in the as-rolled tapes, (b) the random nucleation and growth of the Bi-2212 phase on the AEC's during the early stages of heat treatment, and (c) formation of crack structures in the filaments of the as-rolled tapes.

Since the AEC's are randomly aligned, the nucleation and growth of the Bi-2212 phase from these AEC's can also be expected to be random with respect to the silver sheath. Large crack structures, as shown in Fig. 54c, can develop in the matrix of the as-rolled tapes. Although broadly textured (c-axis perpendicular to the silver sheath) by the rolling process, the local alignment of the Bi-2212 grains can be drastically altered in the vicinity of the crack structures. During subsequent processing, this defect structure may lead to the development and growth of Bi-2212 grains that are also misoriented with respect to the silver sheath. These two effects are important to understand as the local development of the Bi-2223 is directed by the local alignment of the Bi-2212 phase.

The formation of the Bi-2223 phase typically involves the presence of a liquid phase. The liquid phase arises from the interaction of the AEC's, CuO, and Bi-2212 phases. The liquid phase forms slowly and is often found with small silver or silver-copper precipitates as indicated in Fig. 55a. Hence, small particles of silver trapped within the filaments appear to promote the formation of the liquid phase early in the heat treatment. The composition of the liquid averaged over all the samples was $Bi_{1.24}Pb_{0.92}Sr_{0.70}Ca_{0.44}Cu_{1.70}O_y$. The latter composition did not differ significantly from the individual measurements of the liquid phase as a function of processing time

48

indicating that the liquid phase is thermodynamically stable. The measured composition of the liquid phase is not similar to the nominal Bi-2212 stoichiometry as was suggested by an earlier work. In the present work, the stoichiometry of Bi,Pb-2212, in the presence of the liquid phase, was measured to be $Bi_{1.88}Pb_{0.29}Sr_{1.75}Ca_{1.04}Cu_{2.04}O_y$.
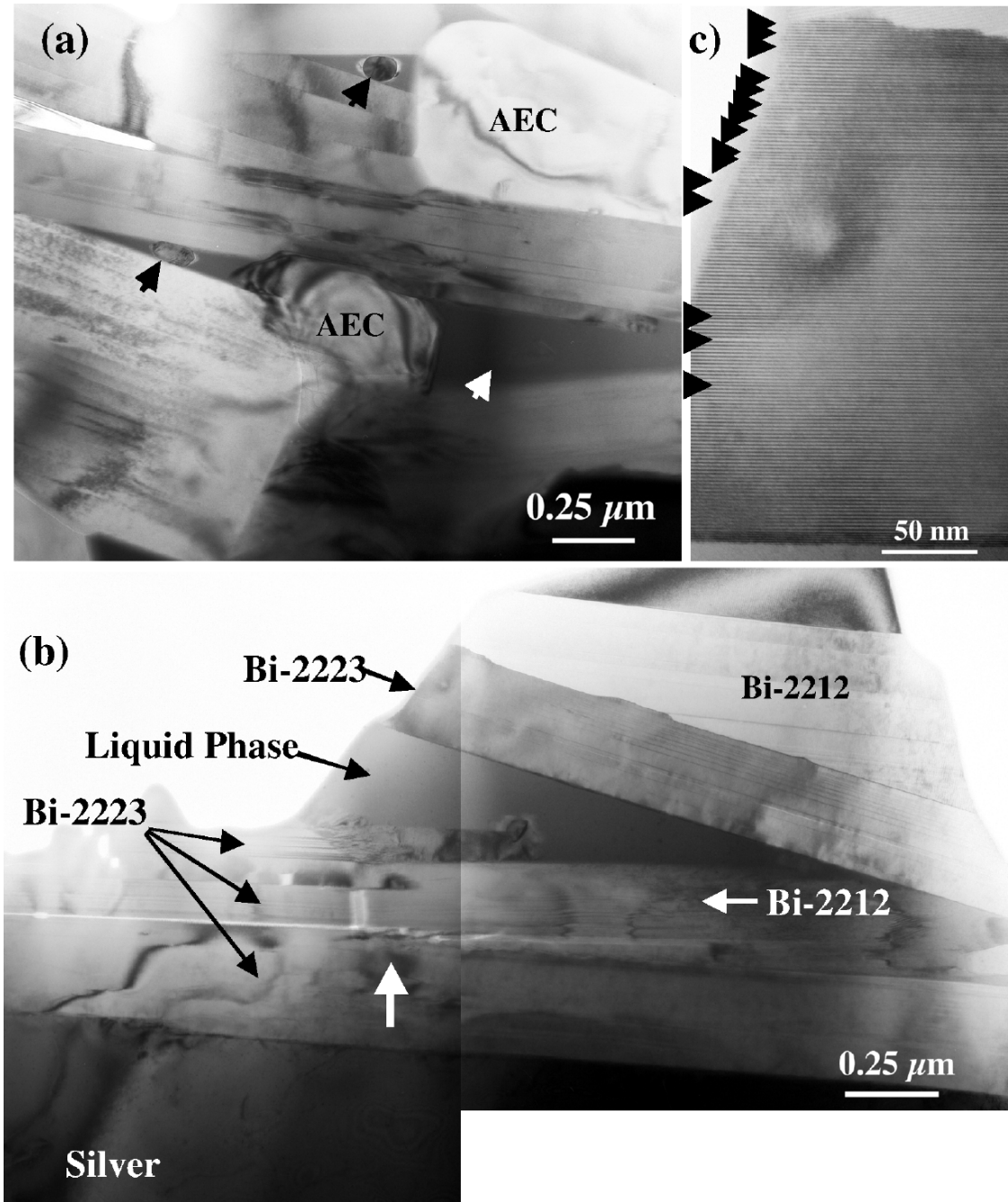
Fig. 55. TEM micrographs of (a) the formation of the liquid phase after 100 minutes at 827˚C, (b) the liquid phase and the precipitation of the Bi-2223 phase after 500 minutes of processing, and (c) the non-uniform distribution of Bi-2212 intergrowths in a "Bi-2223" grain from the sample processed for 500 minutes.
The black arrows in (a) indicate the silver-copper precipitates found in the early liquid phases. The white arrow in (b) denotes the transition zone for the conversion to Bi-2223. The liquid phase is visible at the bottom of (c).

In the early stages of heat treatment, the liquid phase is confined to interstices between grains in the filament. Bi-2223 development does not start until sufficient liquid phase has formed to burst out of its confines, flow through the filament structure, and consume the precursor phases more rapidly as indicated in Fig. 55b. This period of time, between 100 and 300 minutes, is analogous to the induction period described in an earlier work. Bi-2223 grains found in the early stages of heat treatment were always associated with a liquid phase in agreement with earlier works. The TEM micrograph of Fig. 55b shows directly for the first time the formation (white arrow) of the Bi-2223 phase via precipitation from the liquid phase within the filaments. Note that the Bi-2223 phase is assuming the approximate alignment of the existing Bi,Pb-2212 phase. This result confirms the earlier work that showed Bi-2223 precipitating from a lead-rich liquid on the surface of a pressed pellet. Intergrowths of the Bi-2212 phase are commonly found in the converted grains as indicated in Fig. 55c. However, they are non-uniformly dispersed and their density is directly proportional to the distance from the adjacent liquid phase suggesting different diffusion rates for the individual components within the liquid phase.

As the Bi-2223 precipitates, a shell of Bi-2223 is formed around the pocket of the liquid phase as indicated in Figure 55b. Since the Bi-2223 phase can be in equilibrium with the liquid phase, such a structure would be stable and would act to confine and inhibit the liquid phase from consuming more of the precursors. Hence the need for an intermediate deformation step to break up these structures and allow the reactions to proceed to completion. Another detrimental effect of the liquid phase is the residual porosity that remains as the liquid phase is consumed to form Bi-2223. The liquid does eventually make its way out of the shell of Bi-2223 leaving behind the triangular shaped porosity that is commonly found in the Bi-2223 tapes. Again, this demonstrates the need for an intermediate reduction to close up the porosity and enhance the grain-to-grain alignment of the Bi-2223 phase.

To summarize, the formation of the Bi-2223 and its associated microstructure in silver sheathed tapes was documented. Defects and secondary phases in the as-rolled tape can significantly affect the alignment and phase development of the intermediate Bi-2212 phase during the initial stages of heat treatment. This is an important point to understand as the local formation of the Bi-2223 follows the local alignment of the Bi-2212 phase. A direct observation of the precipitation of the Bi-2223 phase from a intermediate liquid phase within the Bi-2223 tapes was made and the composition of the liquid phase was measured. Its formation starts at the interface between the lead-rich Bi-2212 phase and surrounding alkaline-earth cuprates. The precipitation process that forms Bi-2223 can also form structures that further inhibit phase conversion and leave behind residual porosity. Both of these aspects point to the need for an intermediate deformation process that closes up porosity and brings the remaining precursor materials into contact to complete the phase transformation to Bi-2223.

2.1.7 Influence of Microstructures and Crystalline Defects on the Superconductivity of MgB$_2$

A. Serquis, Y. T. Zhu, X.Z. Liao, J. Y. Coulter, J. Y. Huang, J. O. Willis, D. E. Peterson, N. O. Moreno, J. D. Thompson and F. M. Mueller, (Univ. Ill.-Chicago:) R.F. Klie, J.C. Idrobo. N.D. Browning, (Univ. Calif. San Diego:) V. F. Nesterenko and S. S. Indrakanti

Magnesium diboride is a promising superconducting material for a number of applications, including some power markets, MRI, motor-generator sets, and for use in microwave cavities and accelerators.

It is well known that lattice defects, strain and vacancies may affect the physical properties of superconductors, such as superconducting transition temperature Tc and the critical current density Jc. However, there are so far no studies on the influence of lattice strain and defects on the superconductivity of MgB$_2$. The objective of this study is to understand the influence of structural defects (e.g., Mg vacancies) and the lattice strain on the superconducting properties of MgB$_2$ samples.

Several different samples were prepared using varying starting materials and/or synthesis temperatures. Boron powder (Sample A) or B + Mg powder mixture (Samples B and C) were pressed to pellets (5 mm in diameter x 4 mm in thickness). The pellets, and the Mg turnings for Sample A, were wrapped in Ta foil and placed in an alumina crucible inside a tube furnace under ultra-high purity flowing Ar. The samples were heated for one hour to corresponding synthesis temperatures (900°C for A and B; 750°C for C), cooled down at 0.5°C/min to 500°C, heated again for one hour at corresponding synthesis temperatures, and then furnace cooled to room temperature. Sample C was preheated at 600°C for 5 hours.

A SQUID magnetometer (Quantum Design) was used to measure the susceptibility of the samples over a temperature range of 10-45 K under an applied field of 10 Oe. As it can be seen in Fig. 56, all samples have sharp transitions. It is interesting to note that in the inset of Fig. 56 the superconducting transition of Sample A (ΔTc ~ 0.5 K) is several times sharper than that of a commercial powder (ΔTc ~ 11 K).
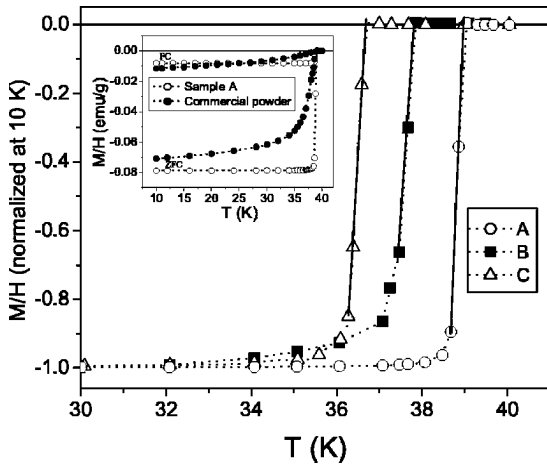
Fig. 56. Inductive superconducting transitions for several MgB$_2$ samples.
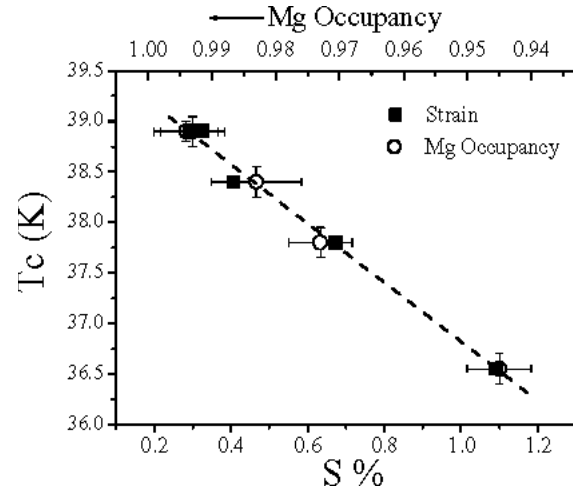
Fig. 57. Superconducting critical temperature as a function of strain and Mg occupancy for several MgB$_2$ samples.

It is clear from Fig. 57 that there is a strong correlation (-99%) between the T$_c$ and the lattice strain. The change in T$_c$ with strain is in agreement with the fact that in the MgB$_2$

system, T_c also decreases quasi-linearly with applied hydrostatic pressure, which causes a higher compression in the c axis than in the a axis. Although the average lattice parameters are the same in all our samples, small local variations caused by microstrains are likely the origin of the reduction in the T_c.

We present a direct atomic resolution analysis of oxygen rich MgB_2, using analytical scanning transmission electron microscopy (STEM). In particular, we show the detailed structure of oxygen rich precipitates that were found in high concentrations within the bulk of MgB_2 grains. It was proposed earlier that an ordering of oxygen inside the bulk material is responsible for these defects that can act as pinning sides inside the grain, therefore causing a higher critical current and an improved superconducting transition. We find that oxygen replaces boron from the ideal MgB_2 structure, which causes a periodic superstructure to appear in both STEM and conventional TEM images. The combination of Z-contrast imaging (Fig. 58) and EELS (Fig. 59) allows us now to quantify the amount of oxygen present in the individual atomic columns and compare measured image contrast in the Z-contrast image with multi-slice image simulations (Fig. 60) for the suggested MgBO structure.
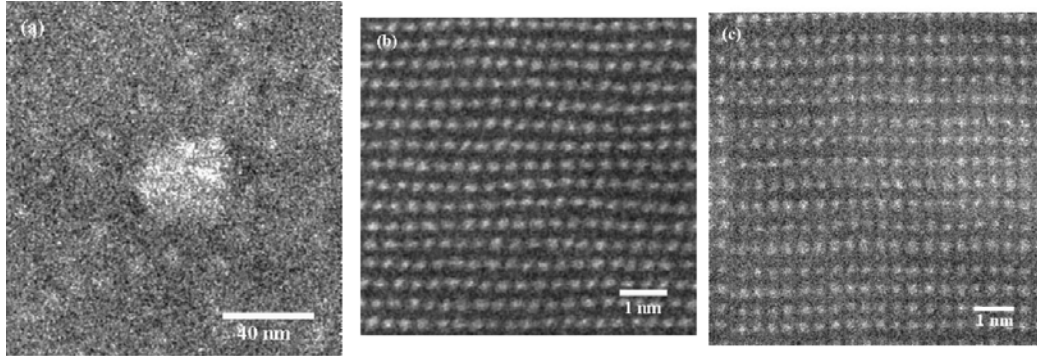
Fig. 58. a. Low magnification Z-contrast micrograph showing the brighter precipitate. b. Z-contrast image of bulk MgB_2 in the [010] direction. The bright spots represent the Mg columns; pure B columns are not visible. c. Z-contrast image of the coherent oxide precipitates in the bulk of the MgB_2 [010]. A contrast variation in every second columns is visible.
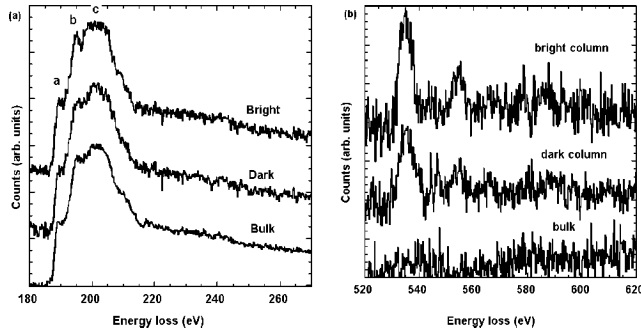
Fig. 59. a EELS B–K edges from the bulk, and the bright and dark column in the oxide precipitates. b. O–K edges from the same columns.
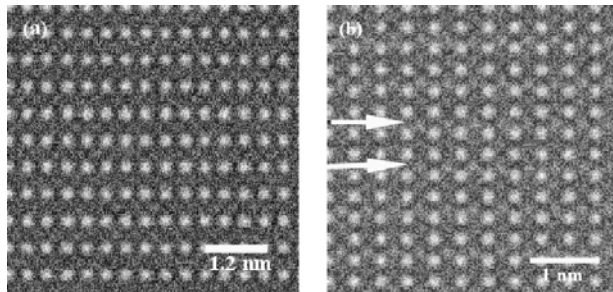
Fig. 60. a Simulated Z-contrast image from bulk MgB_2 in the [010] direction. b. Simulated Z-contrast image from the MgB_2 bulk matrix with 54% oxygen substitution.

52

However, to make practical devices, it is essential to understand the stability of MgB_2 under service environment. Most high-temperature superconductors are highly sensitive to moisture in air. Zhai et al. studied the degradation of superconducting properties in MgB_2 films by exposing it to water and observed that the T_c(onset) of the films remained unchanged throughout the degradation process. There are so far no systematic study on the chemical stability of MgB_2, more specifically, its sensitivity to O_2, H_2O and CO_2, under ambient conditions. The only observations about the MgB_2 reaction with air were the presence of surface boron oxides, identified by soft x-ray spectroscopy, and magnesium oxide layers covering the grains of MgB_2, found using transmission electron microscopy.

We report the degradation under ambient conditions of MgB_2 samples prepared by different processes. As a result of exposure to air, the superconducting transition of samples with smaller grain sizes and poorly sintered became broader and the Meissner fraction decreased with time (Fig. 61), while well-sintered samples or with larger grains remained largely unchanged. The degradation mechanisms were studied using X-ray Photoelectron Spectroscopy (XPS) on dense MgB_2 pellets prepared using hot-isostatic pressing (HIP).

Another challenge is understanding the grain boundary properties of the MgB_2 phase: whether or not weak links are a limiting factor for intergrain critical currents, similar to the situation for polycrystalline high-T_c superconductors (HTSC). Several studies indicate that a strong intergranular current network is established in MgB_2 material, so that the current is not limited by weak-link boundaries. For example, by means of magnetization measurements of grain agglomerates, it has been shown that within these microscopic structures, intergrain and intragrain critical currents are quite comparable in value. In addition, several authors reported that high density samples have high superconducting homogeneity and strong intergranular current flow as determined by magneto-optical studies. However, a rapid drop of the critical current (J_c) at high fields, which could be related to weak link behavior, can be seen in most studies.

Several works show that the transport properties of MgB_2 are sample dependent. Both the reported resistivity at room temperature ρ (297 K) and the residual resistivity ratio, RRR= ρ(297 K)/ ρ(40 K) vary among different research groups by about an order of magnitude. In addition, the T_c and the J_c and its dependence on magnetic field are also sample dependent. This sample dependency has been previously attributed to the synthesis conditions (pressure or thermal history), or to the presence of Mg deficiencies or the presence of oxygen-related defects.
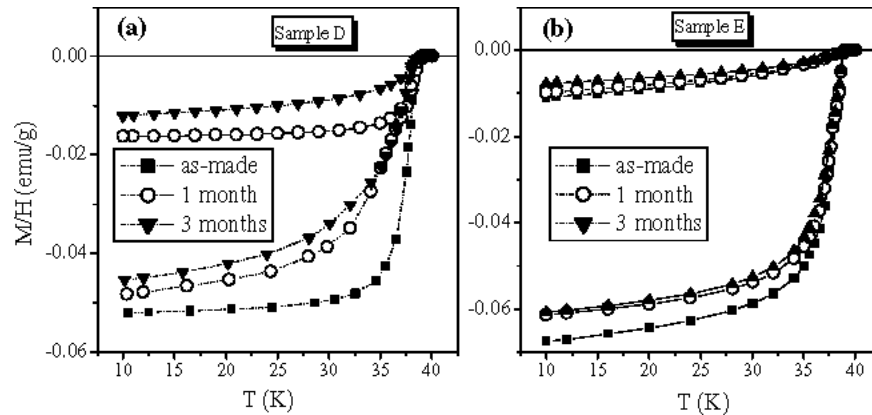
Fig. 61. a. Magnetic susceptibility of a poorly sintered sample as a function of time. b. Magnetic susceptibility of a powder sample. Both samples had small (0.1-0.5 μm) grain sizes.

Several methods have been reported to obtain well-connected and dense samples, and high-pressure synthesis seems to be able to produce fully dense bulk MgB_2 with electrical transport properties superior to those of sintered samples. In a previous work we have produced samples with very sharp superconducting transitions using a Mg vapor infiltration technique. We have observed that Mg(B,O) precipitates provide good flux pinning in these samples leading to a J_c of 1.53×10^5 A/cm^2 at 5 K and 1 T, which is better than that of the first works published on powders and wires. In this work we have used the hot isostatic pressing (HIPing) process to further improve flux pinning of our samples. The objective of this study is to understand the influence of the microstructures and crystalline defects produced by HIPing on the superconductivity of MgB_2

MgB_2 samples were synthesized using an atomic ratio of Mg:B = 1:1 at 900°C under flowing Ar. The starting materials were amorphous boron powder (2325 mesh, 99.99% Alfa Aesar) and Mg turnings (99.98% Puratronic). The boron powder was pressed to pellets (5 mm diameter 34 mm thickness). The pellets and the Mg turnings were wrapped in Ta foil, placed in an alumina crucible inside a tube furnace under ultrahigh purity flowing Ar, and heated at 900°C for 2 h. We shall hereafter refer to the as-synthesized MgB_2 pellet as the un-HIPed sample. The un-HIPed sample was ground into powder and hot isostatically pressed (HIPed) at 200 MPa to form the HIPed sample. The HIPing was carried out in an ABB mini-HIPer unit using a cycle cooling under pressure with a maximum temperature of 1000 °C.

A SQUID magnetometer (Quantum Design) was used to measure the susceptibility of the samples over a temperature range of 5–45 K in an applied field of 10 Oe. Magnetization versus magnetic field (M–H) curves were measured on rectangular-shaped samples at temperatures of 5 and 30 K under magnetic fields up to 70 kOe to determine the critical current density $J_c(H)$.

The direct current (dc) resistivity as a function of temperature was measured with a standard four-probe method in a commercial system, (PPMS Quantum Design) on samples with dimensions of ~2x0.5x0.8 mm. The surface morphology and microstructures of the samples were characterized using a JEOL 6300FX scanning electron microscope (SEM) and a Philips CM30 transmission electron microscope (TEM) operating at 300 kV and a JEOL 3000F TEM operating at 300 kV. TEM samples were prepared by grinding the MgB_2 pellets mechanically to a thickness of about 50 μm and then further thinning using a Gatan precision ion polishing system.

Fig. 62a shows the dc magnetization (M) as a function of temperature for the un-HIPed and HIPed samples. The magnetization of the commercial Alfa Aesar MgB_2 powder and that of the same powder HIPed are also shown for comparison. It is obvious that the samples synthesized in this study (both un-HIPed and HIPed) have higher T_c and sharper superconducting transitions than the as purchased and HIPed commercial Alfa Aesar samples. It can be seen that the superconducting transition in the un-HIPed sample is slightly sharper than those of the HIPed samples. It is not clear what caused the transition broadening in the HIPed sample. However, the broadening could be related to the microstructural changes induced by the HIPing process. As shown in Fig 62b, if the un-HIPed sample is ground in an agate mortar resulting in particles with average size of 5–10 μm, the superconducting transition becomes broader. The same behavior is observed if the HIPed sample is ground. The transition broadening in ground samples can be explained by the penetration length $\lambda(T)$ and its dependence on temperature, which follows the relationship:

$$\lambda(T) = \lambda(0)(1-(T/T_c)^2)^{-1/2}$$

where $\lambda(0)$ = 110–180 nm for MgB_2. Therefore, the penetration length can be significantly larger near T_c than the particle size (leading to transition broadening) and decreases with temperature. As shown in Fig. 63 isolated particles with sizes less than 1 μm exist in the ground un-HIPed sample. These particles are smaller than the penetration length near T_c, and a lower temperature is needed to expel the magnetic field from most of the particles volume, giving rise to the transition broadening. In other words, the transition broadening is caused by the small particle size rather than sample inhomogeneity, impurities, or weak link behavior as was suggested by others.
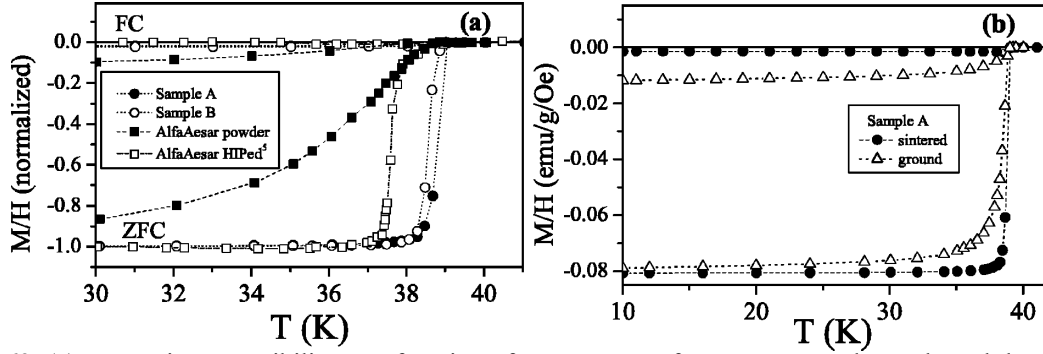
Fig. 62. (a) Magnetic susceptibility as a function of temperature of MgB_2 un-HIPed sample and the HIPed sample. (b) Magnetic susceptibility as a function of temperature of MgB_2, where the superconducting transition of sintered un-HIPed sample is compared with that of the same sample ground.
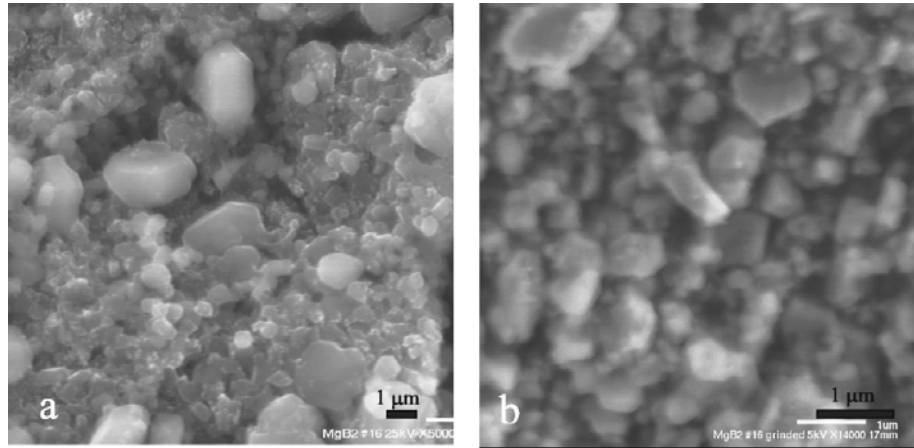
Fig. 63. SEM micrographs of (a) sintered and (b) ground un-HIPed sample.

The resistivity, ρ (T), of the HIPed and un-HIPed samples are shown in Fig. 64. The onset of the transition is 39.4 K for the un-HIPed sample and 38.5 K for the HIPed sample, while the transition width $\Delta T(10\%–90\%)$ is 0.3 K for both samples. The lower resistivity at room temperature $\rho(297\ K)$ for the HIPed sample may be due to its higher density and better intergranular connections, as will be discussed later. The RRR = ρ (297 K)/ ρ(40 K) of the un-HIPed and the HIPed samples are ~8.9 and 3.1, respectively. The last result is similar to those reported previously for HIPed Alfa Aesar powders (RRR=2.47 and 3.46). It has also been reported that single crystals of MgB_2 (~100 μm) with superconducting transitions around 38.1–38.3 K and ΔT = 0.2– 0.3 K have an estimated resistivity at 40 K of 1 μV-cm and a RRR = 5. As the phonon contribution to resistivity decreases with decreasing temperature, other defects present inside the grains (not in the grain boundaries) must have affected the resistivity near T_c. The possible

explanation for the reversed behavior of resistivity of un-HIPed and HIPed samples below 150 K is that grain boundaries in un-HIPed sample provide larger input to resistivity at higher temperatures than dislocations in HIPed samples, but the phonon contribution from bulk of grains in the un-HIPed sample is decreasing faster with temperature than in the bulk of defect saturated grains in the HIPed sample. This may mean that phonon contribution to resistivity is affected by the dislocation structure to the great extent. Xue *et al.* reported a correlation between RRR and the strain determined by Rietveld analysis of the x-ray diffraction data. In Fig. 65 we plot the strain values versus the RRR of our samples, together with the data of Xue *et al.* The clear dependence of RRR upon strain confirms that the residual resistance is related to lattice distortion (strain). As we can see below, this lattice distortion may be related to the presence of higher densities of defects.
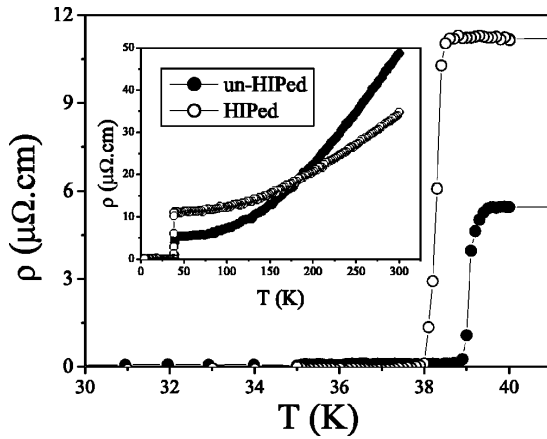
Fig. 64. dc resistivity as a function of temperature for the un-HIPed and HIPed samples. The inset shows an extended range of temperature.
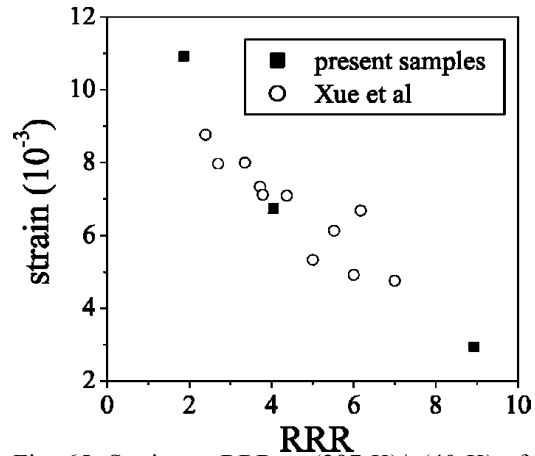
Fig. 65. Strain vs. RRR= $\rho(297 K)/\rho(40 K)$ of the present samples compared with the results of Xue *et al.*

The magnetization versus magnetic field (M–H) curves of the HIPed and the un-HIPed samples are shown in Fig. 66. The magnetization data start at zero field cooling and then trace the hysteresis loop. Some flux jumps can be observed in the region between 0 and 1 T. It can be seen from the insets that the reversible region in the HIPed sample lies above 7 T at T=5 K and above 1.9 T at 30 K, while for the un-HIPed sample, these values are reduced to 6.2 and 1.8 T, respectively.

$J_c(H)$ was determined using the Bean critical state model[20] for a long parallelepiped:

$$J_c(H)[A/cm^2] = 20 \times \Delta M(H)[emu/cm^3]/(a-a^2/3b)[cm],$$

where a and b are the lengths of the parallelepiped edges perpendicular to the magnetic field and ΔM is the width of the magnetization loop at the applied magnetic field H.

Fig. 67 shows the dependence of J_c on the applied magnetic field for both HIPed and un-HIPed samples. The J_c at 0 T is nearly the same for both samples, although some flux jumps are present in the HIPed sample below 1 T. However, the HIPed sample has a significantly higher J_c than the un-HIPed sample in magnetic field. The difference in J_c between the HIPed and un-HIPed samples increases with field. The un-HIPed sample shows a steep drop in J_c at higher fields (H>45 kOe and T = 5 K). No such steep drop in J_c is observed in the HIPed sample.

56
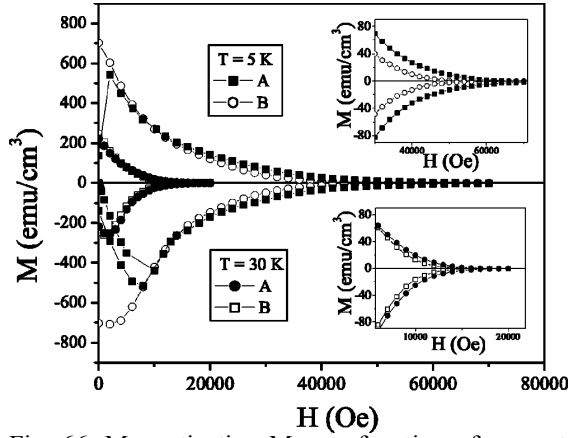
Fig. 66. Magnetization M as a function of magnetic field H at 5 and 30 K for the un-HIPed and HIPed samples.
Upper inset: expanded view showing the onset of the reversible regime at 5 K. Lower inset: expanded view showing the onset of the reversible regime at 30 K.
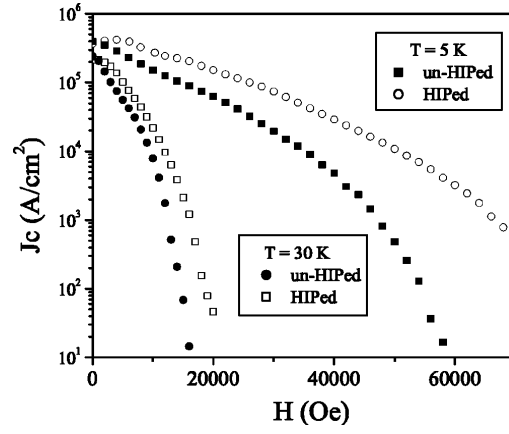
Fig. 67. Magnetization critical current density J_c as a function of magnetic field H for the un-HIPed and HIPed samples at 5 and 30 K.
The J_c at 0 field is nearly the same for both samples, but the differences between the samples increases with field, and the drop in J_c at higher fields is remarkably faster in the un-HIPed sample than in the HIPed one.

In fact, the HIPed sample has better flux pinning than samples reported earlier by other groups and is among the best reported in MgB_2 bulk samples. The excellent flux pinning in the HIPed sample was caused by the modification of microstructures and crystalline defects during the HIPing process. Therefore, it is essential to study the differences in the microstructures and defects of the HIPed and un-HIPed MgB_2 samples. Fig. 68a shows the surface morphology of the un-HIPed sample. Well-developed grains of around 0.3–5 µm can be seen in the figure. However, the grains are not well connected on the surface. In contrast, the grains in the HIPed sample (Fig. 68b) are well compacted. The high density of the HIPed sample makes it possible to prepare a polished shiny surface of mirror quality (Fig. 68c). Fig. 69a shows a TEM bright-field image of the un-HIPed sample, which reveals poor connectivity among the MgB_2 grains. The white areas in the figure are pores, and the dark areas have been proven to be MgO by electron diffraction, as shown in Fig. 69c. The MgO consists of nanometer-sized grains, as demonstrated in Fig. 69b. The images in Figs. 68a and 69a clearly show that the MgB_2 grains of the un-HIPed sample are not well connected. In other words, weak links exist at the grain boundaries of this sample. Fig. 70 shows the excellent connectivity between the MgB_2 grains of the HIPed sample. Neither pores nor MgO are seen at MgB_2 grain boundaries. The MgO, seen at the MgB_2 grain boundaries in the un-HIPed sample (Fig. 69a), have been broken up and dispersed inside the MgB_2 grains in the form of fine MgO particles. In addition, the dislocation density inside the MgB_2 grains is much higher in the HIPed sample (Fig. 70) than in the un-HIPed sample (Fig. 69).
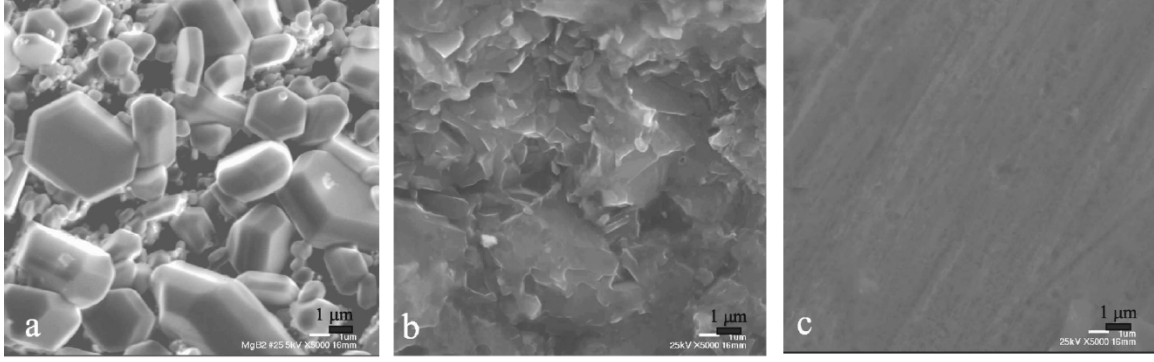
Fig. 68. SEM micrographs of MgB$_2$ samples: (a) surface of un-HIPed sample, (b) HIPed sample, and (c) polished HIPed sample.
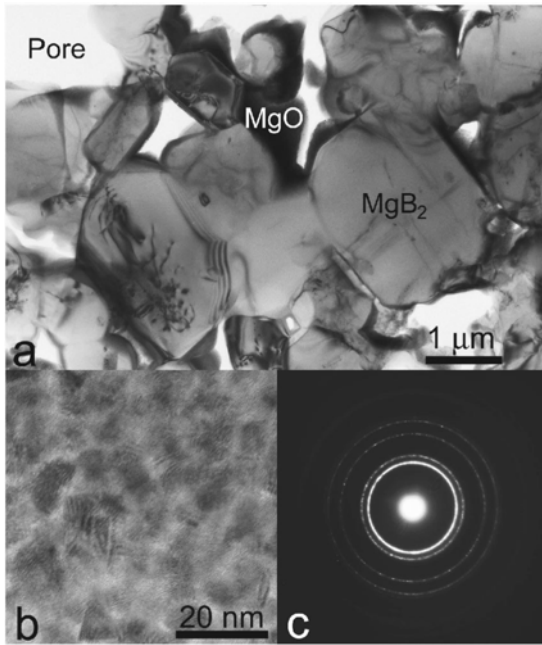
Fig. 69. (a) Bright-field image of the un-HIPed sample reveals poor connectivity among MgB$_2$ grains. Pores and MgO at the grain boundaries of MgB$_2$ are seen; (b) a magnified image of a MgO area showing the nanometer-sized grains characteristic of MgO; (c) electron diffraction pattern of MgO from one of these areas.
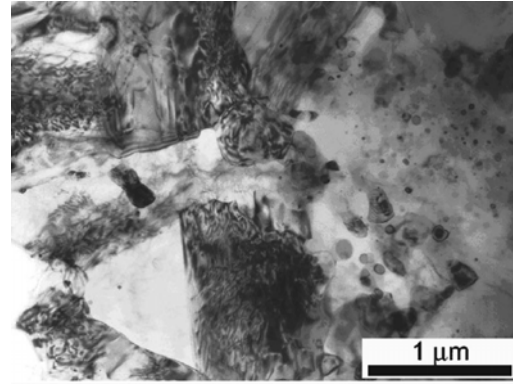
Fig. 70. Bright-field image of the HIPed sample shows that connectivity among the MgB$_2$ grains has been greatly improved. No pores are seen.

In a previous work, we also observed nanometer-sized coherent Mg(B,O) precipitates inside the MgB$_2$ grains in the un-HIPed samples, which are also present in the HIPed ones. However, because of the non-zone-axis imaging conditions used for Figs. 69a and 70, the precipitates cannot be seen in these images. Note that the fine MgO particles, with sizes around 10–50 nm, as well as high density of dislocations, are present only in the HIPed sample. It is well known that extended defects, such as dislocation networks and small precipitates of nonsuperconducting second phases, are likely to be effective flux pinning centers. In other words, the higher J$_c$ in the HIPed sample (Fig. 67) is due to effective flux pinning of finely dispersed MgO particles as well as high-density dislocation networks. These finely dispersed MgO particles and high-density dislocations also caused the higher strain in HIPed sample, which resulted in a low RRR value in that sample.

The steep drop J_c at higher fields (>45 kOe) in the un-HIPed sample is attributed to the porosity and MgO oxide on the grain boundaries. Dou *et al.* reported evidence for decoupling of the grains in sintered MgB_2, both through partial flux jumping and a step in the field dependence of J_c. These authors showed that initial bulk superconductor samples break down into a granular assembly beyond a certain critical value of field and temperature. As well as in our un-HIPed sample they observed a clear drop in the ΔM (which is proportional to the J_c), which can be attributed to the magnetic breakdown of the grain matrix as a result of flux penetration into the grain boundaries that may contain impurities. In the low-field region the current circulates mainly over the entire sample size (intergranular current), while in the high field region the current circulates only in the individual grains (intragranular current). It seems that for the un-HIPed sample this decoupling occurs ~45 kOe at 5 K, whereas for the HIPed sample we did not observe a steep drop in the J_c up to 70 kOe.

In summary, both the sample sintered at ambient pressure (un-HIPed) and the one that was HIPed present the same superconducting properties at low fields, with a very sharp transition observed by both magnetization and resistivity values. The lower RRR values can be ascribed to the presence of strain. Besides, the un-HIPed sample contains discernible empty space (pores) as well as impurity phases at the grain boundaries. The weak connectivity between domains and the presence of impurities in the grain boundaries in the MgB_2 ambient temperature sintered sample seem to limit J_c at high fields, although not as severely as in high-T_c superconductors. The HIP process improves the field dependence of J_c through better connectivity of the grains, the generation of dislocations, and the destruction of MgO at MgB_2 boundaries, which is redistributed in the form of fine particles inside the MgB_2 matrix. These defects can act as effective flux pinning centers. The HIPed sample also has a higher irreversibility field, which is an important parameter in potential applications.

2.2 Systems Technology
2.2.1 HTS Fault Current Controller (FCC) Restoration Project

H.J. Boenig, J.A. Waynert, C.H. Mielke, J.B. Schillig, J.O. Willis, L.E. Bronisz, J.E. Serna, D.A. Roybal, J.A. Stewart; (IGC SuperPower): P.J. Pellegrino, X. Yuan, P. Sutherland; (General Atomics:) B.L. Burley, A. Langhorne; (Texas Tech. Univ.:) A. Neuber, H. Keene; (Cryomech, Inc.:) P. Gifford, R. Dishman

Introduction The Department of Energy (DOE) originally awarded a Superconductivity Partnership Initiative (SPI) contract to a team led by General Atomics to develop a 15 kV class, 26 MVA high temperature superconducting (HTS) Fault Current Controller (FCC). The final stage of this SPI involved installation and testing of the FCC in the Center Substation of Southern California Edison (SCE) in June-July 1999. High voltage breakdown in each of the three phases of the FCC rendered the device inoperable and precluded the completion of the demonstration tests. DOE then contracted with Los Alamos National Laboratory (LANL) to evaluate the extent of the damage, and if feasible, to repair or modify the FCC, and to perform high voltage testing at the 13.7 kV substation at Los Alamos.

This report presents the potential causes of the high voltage breakdown, the high voltage (HV) bus design changes which address these potential failure mechanisms, a brief discussion of cryogenic and vacuum issues, and finally, the very successful results of the single-phase testing of the modified FCC with the HTS coil.

A fault current limiter (FCL) is a device placed in an electric network to limit the peak current in the event of a fault. Many projects are aimed at developing a resistive type HTS FCL. In this type device, the HTS element is placed in series with the circuit breaker. When a fault occurs, the increasing current exceeds the critical current of the HTS element causing a rapid increase in impedance in the circuit, which limits the value of the fault current.

In contrast, the FCC is based on a full-wave bridge. The four thyristors as shown in Fig. 71 provide the blocking and current limiting features. The HTS coil remains superconducting under normal operating conditions. A dc bias power supply establishes a bias current through the four thyristors with half the coil current passing through either of the two legs. The ac load current is superimposed on the bias current. If the peak ac current exceeds the magnitude of the dc bias current, as in a short circuit, the current value will pass through zero, turning off a pair of thyristors each half cycle. The inductance is automatically switched into the circuit, limiting the current because of the added impedance. With the additional capability to control the phase of the firing of the thyristors, the magnitude of the ac current can be regulated from the maximum shorting value to zero. Hence, the FCC can control the value of the fault current rather than merely limit it. Fig. 72 shows the three-phase FCC parked at the LANL substation.
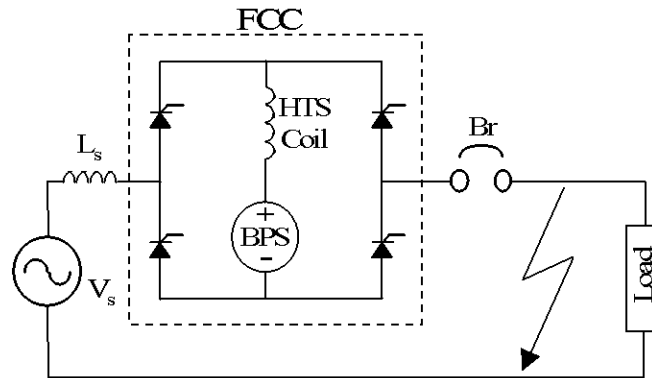
Fig. 71. Schematic showing keys components of FCC and location in typical network. V_s is the voltage source, L_s is the source inductance, Br is the breaker, and BPS is the bias power supply.

Fig. 72. The FCC on a semi-trailer. The cold head compressors are under the tarp to the far left. The small door leads to a control room. Behind each of the three large doors is a vacuum vessel with an HTS coil inside. The power electronics are behind the vessels and cooled by the circulation system at the right end of the trailer. The LANL substation can be seen to the right of the trailer.

HV Bus Failure Mechanisms The FCC has a vacuum vessel with an HTS coil for each of the three electrical phases. The vessel provides the cryostat for maintaining the temperature and thermal isolation of the HTS coil. Three Gifford-McMahon (GM) cryocoolers are used to cool the coil, the thermal shield, and the HV leads. The cryocooler compressors are electrically isolated from the cold heads.

One of the vessels had experienced a small internal helium leak and was being actively pumped during the testing at the SCE substation. That vessel experienced HV breakdown through the residual gas in the polymer tubing connecting the backing pump, which was at ground potential, to the diffusion pump mounted on the vessel. Upon disassembly of the other two vessels, evidence of burn marks on the vacuum vessel, vaporization of multi-layer insulation (MLI), and partial melting of HV bus bolt threads was seen. It appeared that an electrical arc had passed from the HV bus to the nearby, grounded cold head.

Some of the more obvious causes of the HV breakdown were field enhancement by the presence of sharp corners on the HV bus structure, and the presence of dirt particles, which can act as emitters or microparticles that are electromagnetically stripped off the surface and contribute to microplasmas on collision with the opposing electrode. Other less obvious potential causes of the breakdown were also identified:

61

1. The HTS coil may see twice the applied voltage because of a resonance between the source reactance and the stray capacitance of the coil. A low inductance capacitive snubber across the coil could remedy this.

2. The source voltage also has a stray capacitance, which, combined with the coil stray capacitance, can result in fast (nanosecond time scale) charging currents in the bus. The increased joule heating from the currents within the skin depth of the bus could evaporate any condensate on the bus. This would raise the gas pressure locally, decreasing the breakdown voltage.

3. The MLI near the HV bus penetration of the thermal shield appeared unconstrained. The MLI is readily displaced by an electric field that could arc to the material, vaporizing it, producing a local gas cloud, reducing the discharge strength, and allowing an arc from the bus to the grounded region.

4. A current in the bus generates a local magnetic field, which forces any free electrons in the vacuum space to undergo a helical motion. There may be a two-order decrease in the magnitude of the breakdown voltage when the diameter of the helical motion becomes comparable to the mean free path of the residual gas. For the FCC, this would occur for a current of about 20 kA as might be generated per item 2 above.

Although the exact cause of the breakdown cannot be identified, any one or combination of the above may have contributed to the arc.

HV Bus Redesign The more obvious causes of the HV breakdown listed above can be avoided through general HV engineering practice. The redesigned bus has no sharp corners. Furthermore, all assembly was done in a clean environment with efforts taken to minimize the production and agitation of dust. All the internal components of the FCC vessels received a final cleaning with ethanol using lint-free materials to remove dust particulates. Three of the other four voltage breakdown mechanisms can be mitigated with a simple change in design of the bus. The previous design of the HV bus used a grouping of several layers of thin copper sheets as shown in Fig. 73. The resulting design is rectangular in cross-section. In addition, there were relatively sharp corners on the silver plated copper terminals that connected to the threaded vertical rods, one on the HV bushing, which penetrates the vacuum vessel top plate, and one that penetrates the thermal shield within the FCC vessel. Fig. 74 shows a schematic of the HV bus. The internal arcing occurred between points a and b.
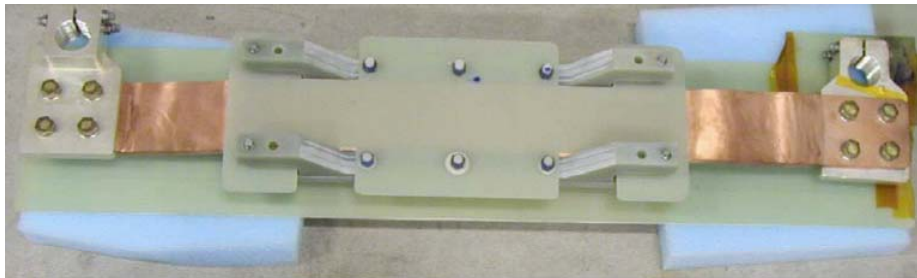
Fig. 73. Horizontal portion of the failed HV bus. The left end connects to a threaded copper rod that is part of the HV bushing that penetrates the vacuum vessel top plate. The right end connects to a threaded copper rod, which penetrates the thermal shield. The green colored G-10 is used to support the copper sheets of the conductor.
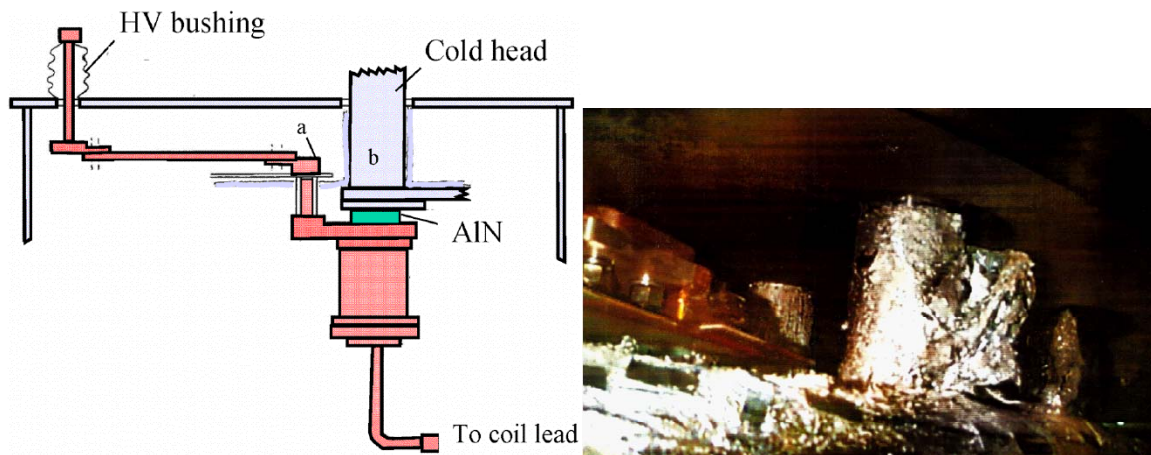
Fig. 74. Left-Schematic of the HV (red) bus, and the grounded (blue-green) vacuum vessel and cold head. The internal arcing occurred between the HV bus at 'a' and the grounded cold head at 'b'. The aluminum nitride, AlN, which separates the HV bus from the cold head, is also shown. Right-burned MLI near the HV bus, visible on the left..

The HV conductor is now a 1,029,000 circular mil Litz wire (individually insulated multistrand conductor) inside a stainless steel tube. The tube is wrapped in a dielectric and a grounding sheath is applied as a final wrap. Thus, the electric field is confined to the annular space between the inner stainless tube and the ground sheath. The two exceptions to the confined electric field design are the warm end of the bus where it connects to the HV bushing, which penetrates the vacuum vessel top plate, and the opposite, cold end of the bus, which interfaces to the cryocooler. Finite element electrostatics analysis was used to evaluate conductor shapes that minimize electric field enhancements in these two regions. Convoluted end fittings were used to lengthen the HV tracking paths connecting the ground sheath termination to the HV portion of the bus. Several prototype busses were fabricated to evaluate key design features and fabrication techniques. The prototypes and the final bus were hipot tested in air, thermally cycled to liquid nitrogen temperature, hipot tested again in air, and then hipot tested in vacuum. Fig. 75 illustrates the main features of the modified bus and Fig. 76 shows a schematic of the bus as installed in the FCC vessel.
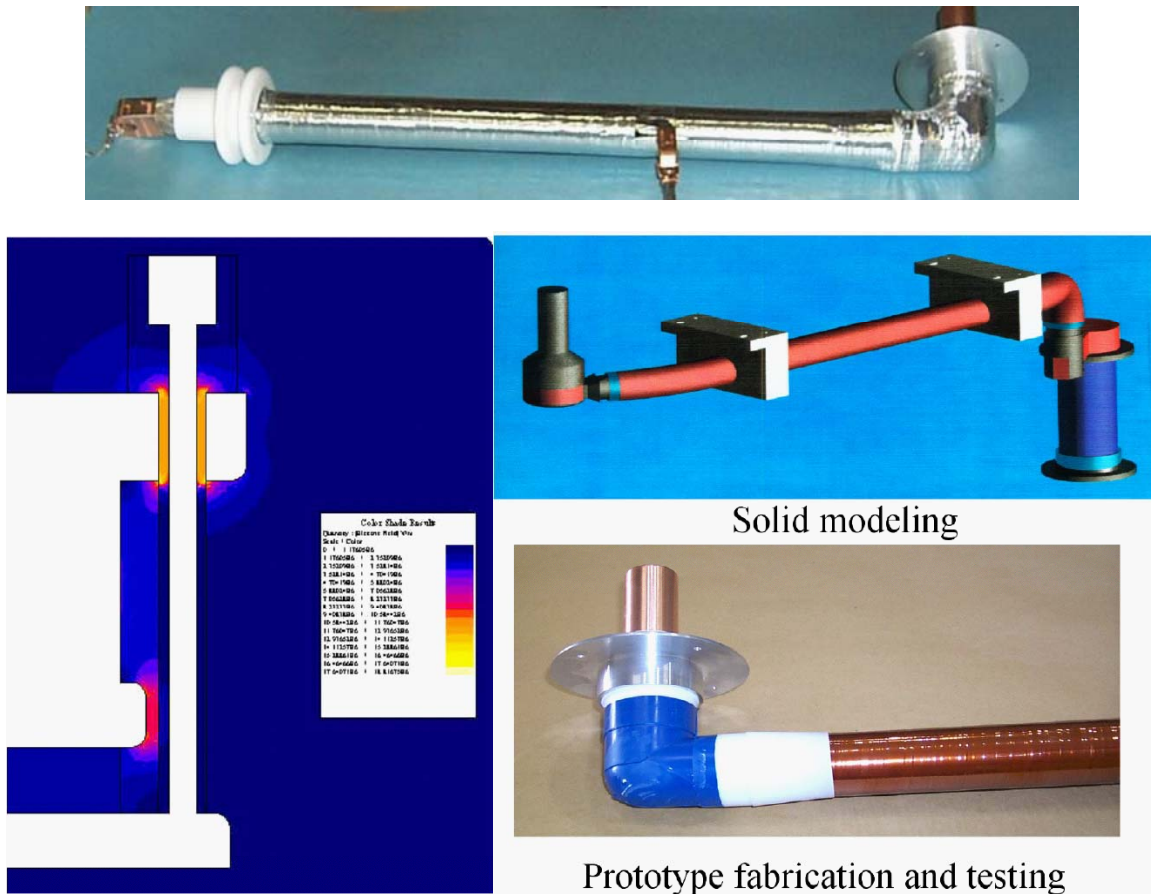
Fig. 75. Top - Modified HV bus undergoing hipot testing. The right end of the bus normally points down as in the Solid Model image on the right. Bottom right is a prototype bus end. At bottom left is a finite element model electrostatic analysis of the new bus.
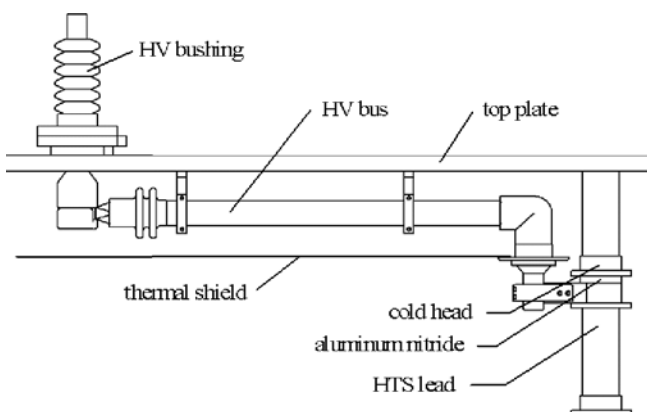
Fig. 76. Drawing of the HV bus, top plate of the vacuum vessel, the cold head which provides the low temperature thermal intercept for the bus, and the aluminum nitride disk which provides the thermal path for cooling the cold end of the HV bus.

Although the internal HV breakdown occurred between the bus and the cold head, it was recognized that the next likely failure location was at the interface between the HV bus and the cold head. Fig. 77 shows the aluminum nitride (AlN) disk separating the HV bus from the cryocooler cold head. The AlN acts as an electrical insulator isolating the bus from the grounded cold head, and as a thermal short, allowing heat to be transferred from the bus to the cold head.
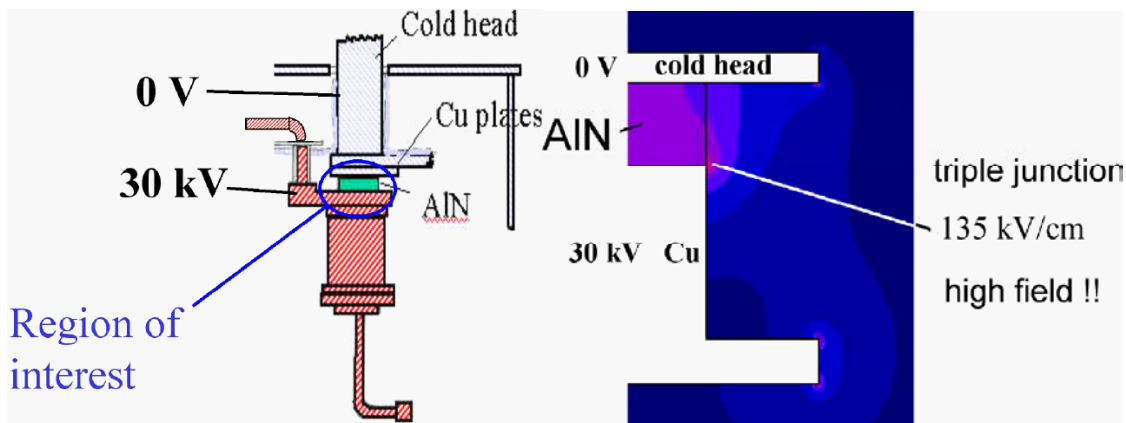
Fig. 77. Left - Schematic of AlN location on the cold head assembly. Right – electrostatic analysis of original cold head/HV bus/AlN disk design showing a triple junction region with a high electric field.

The dielectric strength of AlN is given by the vendor, Kyocera, as 12 kV/mm, and should be more than adequate given the 15 mm thickness separating the bus and the cold head. The main concern is surface flashover. A mock-up of the cold head, AlN, and HV bus was fabricated. A series of experiments were performed by Texas Tech University to determine the breakdown voltage as a function of temperature and vacuum pressure. The results are shown in Fig. 78. The upper curve is for roughly 60 Hz applied pulses. The lower curve is for dc-applied pulses. Also shown is the effect of reversing the polarity across the AlN. If the triple junction between the AlN, Cu and vacuum are such that the Cu is at a negative voltage, the Cu is likely to act as an emitter and lower the breakdown voltage. The interpretation of this data is that, because of the scatter, it is unlikely that the present design would provide adequate voltage standoff.
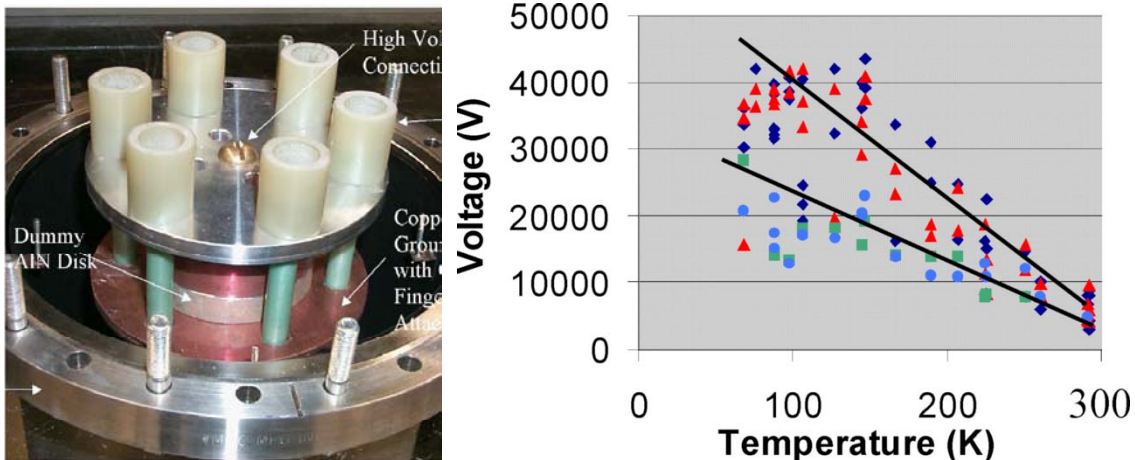
Fig. 78. Left – photograph of the test rig. Right - breakdown voltage across the AlN as a function of temperature and polarity. The upper curve is for roughly 60 Hz pulses and the lower curve for dc. The dark blue diamonds (60 Hz) and green squares (dc) are for the Cu at the triple junction being positive polarity; the other symbols are for the negative polarity case.
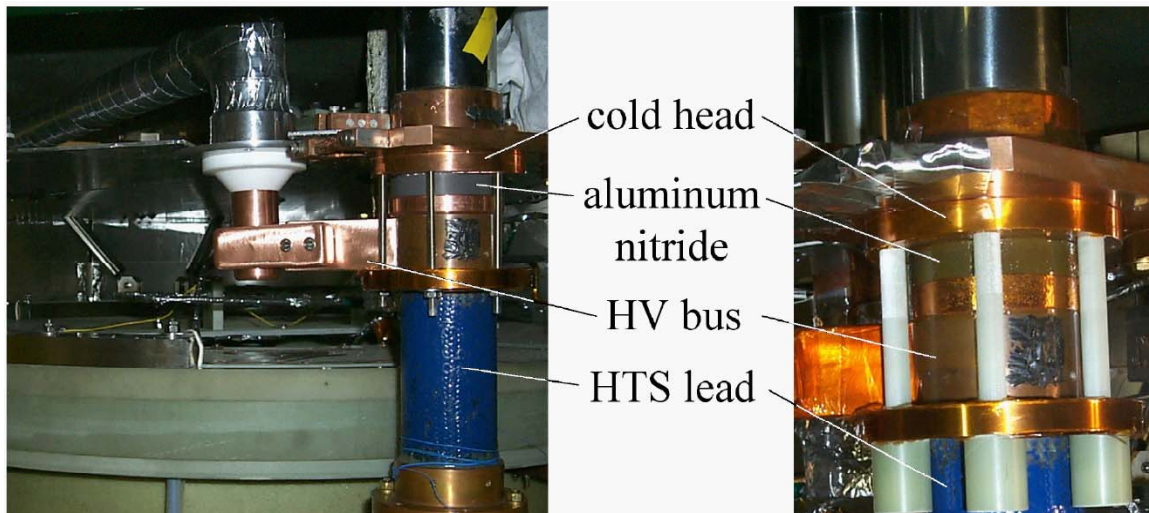
Fig. 79. Photographs of the installed HV bus Hipot tested to 15 kV.

Several design modifications were suggested. These were initially evaluated using a finite element electrostatics code. Two configurations were tested. The installed configuration used a dielectric varnish to cover the triple junction between the AlN, the vacuum, and a copper disk of the same diameter as the AlN and in contact with the HV bus. The final bus and AlN configuration were hipot tested in air, then in vacuum, and finally, connected to the cold head (Fig. 79) and at operating temperature and vacuum conditions. During the final hipot testing of the installed configuration, breakdowns, which were not self-healing, began to occur at 15 kV. The goal was 26 kV, but it was decided that this performance was adequate for testing in the LANL substation where the maximum applied voltage would be less than a 5 kV steady state condition. In addition, this hipot testing was done with dc rather than 60 Hz applied voltage; the 60 Hz results should have a higher breakdown potential than the dc, providing additional operating margin.

<u>Vacuum and Cryogenics Systems and Cool down</u> The original vacuum pumping port was through a roughly 1.5" diameter tube. This severely limits the pumping speed and hence, the pump down time of the FCC vacuum vessel. Thus, a 6" diameter hole was cut into the side of the vessel, a flange welded on, and a gate valve was attached (Fig. 80). A 300 L/s turbo pump with a dry scroll roughing pump was used for evacuating the system. Once the system had been pumped and purged with dry nitrogen gas, the vessel could be pumped down from atmospheric pressure to 10^{-4} torr within a few hours. The cold heads were typically turned on when the system reached the 10^{-5} torr range. The turbo pump was valved off from the FCC vessel when the pressure dropped below 10^{-7} torr. The temperature of the coil was around 80 K at that time.

66

Fig. 80. Left – cooling fan mounts were adjusted for improved reliability. Right – Vacuum vessel installed in the FCC trailer with additional 6" diameter vacuum port added for improved initial pump down.

During cool down four temperatures were monitored: the two cold head temperatures of the large AL 200's which cool the high and low voltage leads to the coils and the thermal shield; the temperature of the return helium flow from the coils; and the inlet helium coolant flow to the coil just before entering the final heat exchanger attached to the AL 125 cold head. (The outlet from the heat exchanger went directly to the inlet of the coil.) The helium coolant mass flow rate to the coil was periodically monitored, as was the pressure in the FCC vessel. The compressor high and low pressure readings were also monitored. As the coil temperature was reduced below about 50 K, the helium pressure in the compressor for the AL 125 had to be replenished due to the reduction in pressure from the increased density of helium in the coil at the low temperatures. Fig. 81 shows the cool down in terms of the coil resistance as a function of time. At 10,580 minutes, the cooling was stopped, because the initial cooling had been in the high bay of the National High Magnetic Field Laboratory building at LANL and the coil and vessel had to be transported about 100 m to the FCC trailer and installed before the cooling could be re-started at 11,600 minutes.
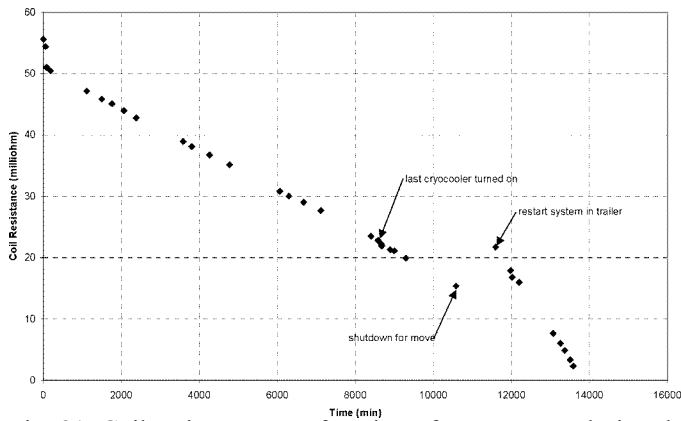
Fig. 81. Coil resistance as a function of temperature during the cool down of the FCC. One of the AL 200 cryocoolers was not turned on until 1000 minutes to prevent excess thermal stresses in the HTS leads.

<u>Single Phase Testing</u> Fig. 82 shows the circuit that was established to test the FCC. The LANL substation, shown to the left of the vertical dotted line, includes a 4.3 mH line inductance and a main breaker (MB). The components outside the substation may be disconnected and grounded from the substation through the D/GS blade switch. A 2.3 mH protection inductor was required by the utility to limit the maximum current that could be drawn. For load tests, the FCC is connected in series with a 64 Ω resistor that draws 1 MW of power (for a maximum of 20 seconds). For load step tests, the Jennings switch (JS), a vacuum load switch, is closed so that the load increases to 3 MW. For shorting tests, the Westinghouse breaker (WB) is closed to provide a short across the load.
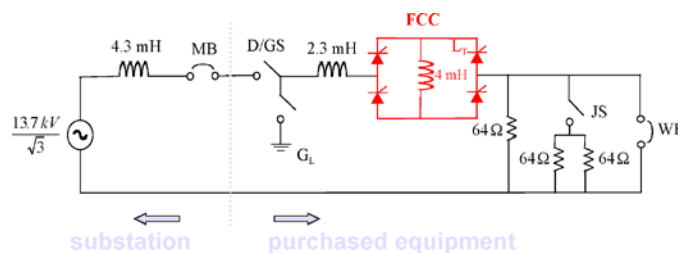
Fig. 82. Circuit used for single-phase testing of the FCC. The substation, to the left of the dotted vertical line has a source impedance of 4.3 mH and the main breaker, MB. The disconnect/grounding switch is D/GS; 2.3 mH is a protection inductor. The load resistance is 64 Ω (1 MW); this becomes 3 MW if the Jennings switch, JS, is closed. WB is a Westinghouse breaker used to short the load.

After verification of the control and operation of all the breakers and switches, the first test of the FCC was a voltage withstand test. With the thyristors in a blocking mode, the full voltage was applied to the FCC to verify that the electronics could successfully withstand the voltage for an extended time. It is noteworthy that 7.9 kV withstand voltage in Los Alamos is equivalent to a voltage about 113% higher (8.9 kV) at sea level.

For proper operation, the FCC should be transparent to the system during normal loading and load changes. To test this, a representative 1 MW resistive load was applied. The ac load current, the current through the thyristors, and the voltages at selected points were measured. The test would also demonstrate that the bias power supply was not necessary. (This last fact had actually been demonstrated in testing earlier this fiscal year using a resistive Cu coil while the HV bus was being modified.) To simulate load changes, the system was started with the 1 MW load, then switched to a 3 MW load, and finally, switched back to the 1 MW load. Fig. 83 shows representative results of a load step test.

The 60 Hz 175 A peak load current for the 1 MW load switches to 525 A peak during the 3 MW operation and back to 175 A peak as the load switches back to 1 MW. Also shown is the nearly dc current through the HTS coil. Without the bias power supply, the coil bias current is drawn from the power source. The bias current adjusts itself to equal the amplitude of the load current. Once the bias current is established, the ac current flows unimpeded through the FCC, except for two short time periods during the 60 Hz cycle when the bias current is recharged to the peak ac value. The coil current decrease is based on the time constant determined by the coil inductance and the series resistance of the coil and thyristors. There is also a forward voltage drop across the thyristors, which creates an additional effective resistance. The cyclic decay and recharge of the bias current is the ripple seen in Fig. 83. This ripple will cause ac losses and a temperature rise in the HTS coil, but the duration of the testing was sufficiently short that no measurable temperature increase in the coil was observed.
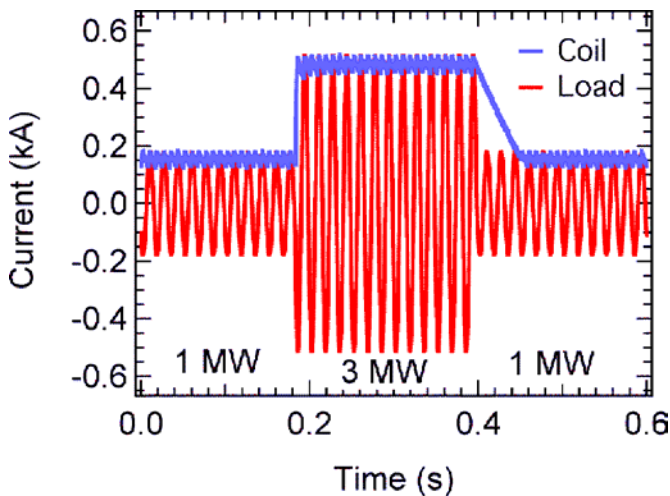
Fig. 83. Illustration of a load step test. The ac load current and the corresponding nearly dc current through the FCC coil are shown for an initial load of 1 MW, switching to 3 MW at about 0.2 s and back to 1 MW at 0.4 s.

The FCC was tested for a fault response by energizing the 1 MW load and then shorting the load by closing the Westinghouse breaker, as discussed above. If the thyristors are triggered at the zero crossing of the voltage (and forward biasing), the FCC coil will be in the ac circuit for the minimum duration and the ac current will be a maximum. However, the ac current may be reduced through use of phase-delay angle control. The triggering of the thyristors can be delayed by a phase angle; the longer the phase delay, the longer the FCC coil remains in the ac circuit. The FCC acts as a variable inductance with values from zero to infinite with the corresponding ac current varying from a maximum value to zero. Fig. 84 illustrates one example of the FCC responding to a fault imposed at about 0.18 s with the phase delay angle set at 120 degrees. Note the change in scale for the ac current compared to Fig. 83. The large, nearly 4200 A, peak current half cycle is the maximum ac current without the FCC coil in the circuit, and evidence of the time required for the control system to react. Fig. 85 shows the peak ac fault current as determined by the setting of the phase delay angle. (It should be mentioned that for phase delay angles greater than 90 degrees, the fault current becomes non-sinusoidal.)
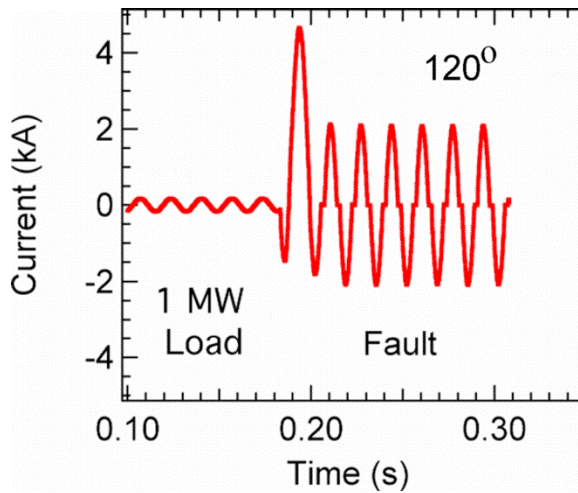
Fig. 84. An example of the response of the FCC to a fault applied at 0.18 s when the phase delay angle is set for 120 degrees. For times less than 0.18 s, the FCC was responding to a 1 MW load (175 A peak current).
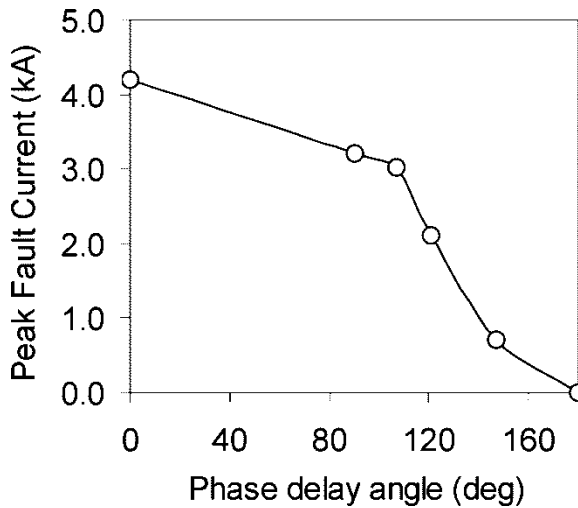
Fig. 85. The dependence of the magnitude of the fault current on the setting of the phase delay angle for the circuit shown in Fig. 7.

To summarize this work, a number of mechanisms have been identified to explain the high voltage breakdown in the FCC vessels. A new design of the HV bus has been developed, fabricated and tested, which addresses all the failure mechanisms identified. The next weakest link in terms of voltage standoff capability is the aluminum nitride. A number of changes have been made in the AlN region, but dc highpot testing indicated breakdown at voltages lower than desired (15 kV rather than 26 kV), but adequate for testing at the LANL substation.

Only one of the three FCC phases was modified, evacuated, and cooled. The device was installed in the FCC trailer and integrated with the LANL substation and appropriate electric load components. The device successfully underwent high voltage standoff testing to demonstrate the system could withstand the total single-phase source voltage. The FCC also responded appropriately to a constant load of 1 MW and load changes of 1 MW to 3 MW and back to 1 MW. The control of the fault current from a maximum value obtained without the FCC in the circuit, to zero current was successfully demonstrated by varying the phase delay angle firing of the thyristors. The single phase FCC was successfully operated without the bias power supply as predicted by circuit modeling.

3. Fiscal Year 2002 Publications

3.1. Journal Articles Published

"Structure, Processing and Property Relationships in Tunable RF and Microwave Devices,"
B.J. Gibbons, B.H. Park, Y. Gim, Y. Fan, A.T. Findikoglu, D.W. Reagor, Q.X. Jia,
Integrated Ferroelectrics **39**, 1211 (2001).

"Rietveld Refinement of Crystal Chemistry of $RBa_4Cu_3O_{8.5+\delta}$ (R=Rare Earth),"
Y.T. Zhu, L. Shu, E.J. Peterson, D.E. Peterson, and F.M. Mueller,
J. Physics and Chemistry of Solids **63**, 23 (January 2002).

"Josephson Plasma Resonance in $Tl_2Ba_2CaCu_2O_8$ in a Magnetic Field Measured Using THz Spectroscopy,"
V.K. Thorsmolle, R.D. Averitt, M.P. Maley, L.N. Bulaevskii, C. Helm, A. Taylor,
Physica B **312**, 84 (March 2002).

"Nonequilibrium Superconductivity in $Y_{1-x}Pr_xBa_2Cu_3O_7$ Thin Films,"
R.D. Averitt, V.K. Thorsmolle, Q.X. Jia, S.A. Trugman, and A.J. Taylor,
Physica B **312**, 86 (March 2002).

"In vacuo Pulsed Laser Ablation of $YBa_2Cu_3O_{7-x}$ Target for the Formation of Y_2O_3 Nanostructures,"
D.B. Jan, Q.X. Jia, M.E. Hawley, G.W. Browne, C.J. Wetteland, H.P. Sun, X.Q. Pan,
Journal of Materials Research **17**, 697 (March 2002).

"High Temperature Superconducting Thick Films with Enhanced Supercurrent Carrying Capability,"
Q.X. Jia, S.R. Foltyn, P.N. Arendt, J.F. Smith,
Applied Physics Letters **80**, 1601 (March 2002).

"Another Look at MgB_2 and YBCO Wires,"
R.A. Hawsey and D.E. Peterson,
Science 296, 655 (April 2002).

"Oxidation of c-Axis Oriented Epitaxial $YBa_2Cu_3O_{7-x}$ Thin Films in Ozone-Containing Atmospheres,"
B.J. Gibbons, C.B. Eom, R.A. Rao, S. Trolier-McKinstry, D.G. Schlom,
J. Materials Research **17**, 884 (April 2002).

"Effect of Lattice Strain and Defects on the Superconductivity of MgB_2,"
A.C. Serquis, Y.T. Zhu, E.J. Peterson, J.Y. Coulter, D.E. Peterson, F.M. Mueller,
Applied Physics Letters **79**, 4399 (Dec 2001)

"Observation of Coherent Oxide Precipitates in Polycrystalline MgB_2,"
   R.F. Klie, J.C. Idrobo, N.D. Browning, A.C. Serquis, Y.T. Zhu, X.Z. Liao, F.M. Mueller,
   Applied Physics Letters **80**, 3970 (May 2002).

"Controlling Flux Pinning Precipitates in MgB_2 Synthesis,"
   X.Z. Liao, A.C. Serquis, Y.T. Zhu, J.Y. Huang, D.E. Peterson, F.M. Mueller, and H.F. Zu,
   Applied Physics Letters **80**, 4398 (June 2002).

"Degradation of MgB_2 under Ambient Environment,"
   A. Serquis, Y.T. Zhu, D.E. Peterson, F.M. Mueller, R.K. Schulze, V.F. Nesterenko, and S.S. Indrakanti,
    Applied Physics Letters **80**, 4401 (June 2002).

"The Influence of Microstructures and Crystalline Defects on the Superconductivity of MgB_2,"
   A.C. Serquis, X.Z. Liao, Y.T. Zhu, J.Y. Coulter, J. Huang, J. O. Willis, D.E. Peterson, F.M. Mueller, N.O. Moreno, J.D. Thompson, V.F. Nesterenko, S.S. Indrakanti,
   Journal of Applied Physics **92**, 351 (July 2002).

"Monolithic Integration of Superconducting YBCO and Dielectric $SrTiO_3$ Films on Polycrystalline Ferrites,"
   Q.X. Jia, J.R. Groves, P.N. Arendt, and F.A. Miranda,
   Integrated Ferroelectrics **42**, 71 (2002).

"Evidence for Line-like Vortex Liquid Phase in $Tl_2Ba_2CaCu_2O_8$ Probed by the Josephson Plasma Resonance,"
   V.K. Thorsmolle, R.D. Averitt, M.P. Maley, M.F. Hundley, A.E. Koshelev, L.N. Bulaevskii, and A.J. Taylor,
   Physical Review B **66**, 12519 (July 2002).

"High Temperature Superconducting Magnetic Refrigeration,"
   P.E. Blumenfeld, F.C. Prenger, A. Sternberg, C. Zimm,
   Advances in Cryogenic Engineering, vol. 47, eds. S. Breon et al., (American Institute of Physics, Melville, NY, 2002), p. 1019.

"Microstructural Development and Control in $YBa_2Cu_3O_7$ Coated Conductors,"
   T.G. Holesinger, B.J. Gibbons, S.R. Foltyn, P.N. Arendt, J.R. Groves, and J.Y. Coulter,
   Advances in Cryogenic Engineering (Materials), vol. 48, eds. U. Balachandran, D. Gubser, and K.T. Hartwig, (American Inst. of Physics, Melville, NY, 2002), p.647.

"The Development of the Superconducting Phase and the Origin of Potential Current Limiting Defects in Bi-2223 Tapes,"
   T.G. Holesinger, J.F. Bingert, R.D. Parrella, G.N. Riley, Jr.,
   Advances in Cryogenic Engineering (Materials), vol. 48, eds. U. Balachandran, D. Gubser, and K.T. Hartwig, (American Inst. of Physics, Melville, NY, 2002), p.724.

"Enhanced Critical Currents in Bi-2223/Ag Sheathed Tapes by High Energy Proton Irradiation**,”**
  J.O. Willis, J.Y. Coulter, M.P. Maley, J.L. Ullmann, S. Fleshler, G.N. Riley, Jr.,
  Advances in Cryogenic Engineering (Materials), vol. 48, eds. U. Balachandran, D. Gubser, and K.T. Hartwig, (American Inst. of Physics, Melville, NY, 2002), p.1201.

3.2. Journal Articles Submitted for Publication

"Conductive Metal Oxide Thin Films,”
  Q.X. Jia,
  Book chapter for **Thin Film Handbook**, Academic Press (in press).

"IBAD Template Films for HTS Coated Conductors,”
  Paul N. Arendt,
  Book Chapter for **Next Generation High Temperature Superconducting Wires**, ed. A. Goyal, Plenum Press (in press).

"Recent Progress in Continued Processed IBAD MgO Template Meters for HTS Applications,”
  J.R. Groves, P.N. Arendt, S.R. Foltyn, Q.X. Jia, T.G. Holesinger, H. Kung, R.F. DePaula, P.C. Dowden, E.J. Peterson,
  Paper submitted to the 10th US Japan Workshop on High-T_c Superconductors, Santa Fe, NM, December 2-5, 2001.

"Bridge-Type Fault Current Controller-A New FACTS Controller,”
  H.J. Boenig, C.H. Mielke, B.L. Burley, J.A. Waynert, J.O. Willis,”
  Paper submitted to IEEE 2002 Power Engineering Society Summer Meeting Proceedings, Chicago, IL, July 21-25, 2002.

"High Critical Currents in Powder in Tube MgB_2 Wires: Influence of Microstructure and Heat Treatments,”
  L. Civale, A.C. Serquis, D.L. Hammon, X.Z. Liao, J.Y. Coulter, Y.T. Zhu, T.G. Holesinger, D.E. Peterson, F.M. Mueller,
  Paper submitted to *IEEE Transactions on Applied Superconductivity*.

"The Influence of Structural Defects on Intragranular Critical Currents of Bulk MgB_2,”
  A.C. Serquis, X.Z. Liao, L. Civale, Y. T. Zhu, J.Y. Coulter, D. E. Peterson, F. M. Mueller,
  Paper submitted to *IEEE Transactions on Applied Superconductivity*.

"Improvement of IBAD MgO Template Layers on Metallic Substrates for YBCO HTS Deposition,”
  J.R. Groves, P.N. Arendt, S.R. Foltyn, Q.X. Jia, T.G. Holesinger, L.A. Emmert, R.F. DePaula, P.C. Dowden, L. Stan,
  Paper submitted to *IEEE Transactions on Applied Superconductivity*.

"AC Losses in Prototype Multistrand Conductors for Warm Dielectric Cable Design,"
J.O. Willis, M.P. Maley, H.J. Boenig, G. Coletta, R. Mele, and M. Nassi,
Paper submitted to *IEEE Transactions on Applied Superconductivity*.

"Fabrication of High J_c $YBa_2Cu_3O_{7-d}$ Tapes Using the Newly Developed Lanthanum Manganate Single Buffer Layers,"
M.P. Paranthanam, T. Aytug, S. Kang, R. Feenstra, J.D. Budai, D.K Christen, P.N. Arendt, L. Stan, R.F. DePaula, S.R. Foltyn, T.G. Holesinger, J.R. Groves,
Paper submitted to *IEEE Transactions on Applied Superconductivity*.

"Growth and Characterization of $SrRuO_3$ Buffer Layer on MgO Template for Coated Conductors,"
Q.X. Jia, S.R. Foltyn, P.N. Arendt, T.G. Holesinger, J.R. Groves, M. Hawley,
Paper submitted to *IEEE Transactions on Applied Superconductivity*.

"Spatial Distribution Analyses of Critical Temperature in Epitaxial Y-Ba-Cu-O Film Using Variable Temperature Scanning Laser Microscopy,"
C. Kwon, L.B. Wang, S. Seo, B.H. Park, Q.X. Jia,
Paper submitted to *IEEE Transactions on Applied Superconductivity*.

"Variable Temperature Scanning Laser Microscopy of Wider Width High Temperature Superconducting Films,"
L.B. Wang, M.B. Price, C. Kwon, Q.X. Jia,
Paper submitted to *IEEE Transactions on Applied Superconductivity*.

"Accelerated Coated Conductor Program at Los Alamos National Laboratory,"
V. Matias, B.J. Gibbons, A.T. Findikoglu, S. Kreiskott, and L. Bronisz,
Paper submitted to *IEEE Transactions on Applied Superconductivity*.

"Vortex Melting in High-T_c Superconductors Probed Using Terahertz Time Domain Spectroscopy,"
A.J. Taylor, V. Thorsmolle, R.D. Averitt, M.P. Maley, M.F. Hundley, L. Bulaevskii, A.E. Koshelev
Paper for *Proceedings of Optical Society of America.*

"Characterization of Superconducting $SmBa_2Cu_3O_7$ Films Grown By Pulsed Laser Deposition,"
Q.X. Jia, S.R. Foltyn, J.Y. Coulter, J.F. Smith, M.P. Maley,
Paper submitted to the *Journal of Materials Research*.

"Imaging Transport Current Distribution in High Temperature Superconductors using Room Temperature Scanning Laser Microscope,"
B.E. Klein, S. Seo, C. Kwon, B.H. Park, Q.X. Jia,
Submitted to *Applied Physics Letters*.

"Flux Pinning Enhancement in Ferromagnetic and Superconducting Thin Film Multilayers,"
D.B. Jan, J.Y. Coulter, B.B. Maranville, M. Hawley, L. Bulaevskii, M.P. Maley, F. Hellman, Q.X. Jia,
Paper submitted to *Applied Physics Letters.*

"Effect of Lattice Strain on the Critical Superconducting Temperature of MgB_2,"
X.Z. Liao, A.C. Serquis, YT. Zhu, D.E. Peterson, F.M. Mueller, H. Xu,
Paper submitted to *Journal of Applied Physics*.

"$Mg(B,O)_2$ Precipitation in MgB_2,"
X.Z. Liao, A.C. Serquis, Y.T. Zhu, J.Y. Huang, L. Civale, D.E. Peterson, F.M. Mueller, H.F. Xu,
Paper submitted to the *Journal of Applied Physics*.

"Microstructure and High Critical Current of Powder-in-Tube MgB_2,
A.C. Serquis, L. Civale, D.L. Hammon, X.Z. Liao, J.Y. Coulter, Y.T. Zhu, D.E. Peterson, F.M. Mueller*,
Paper submitted to *Applied Physics Letters*.

"Reflection High Energy Electron Diffraction Experimental Analysis of Polycrystalline MgO Films with Grain Size and Orientation Distributions,"
R.T. Brewer, H.A. Atwater, J.R. Groves, and P.N. Arendt,
Paper submitted to the *Journal of Applied Physics*.

"Role of $SrRuO_3$ Buffer Layers on the Superconducting Properties of $YBa_2Cu_3O_7$ Films Grown on Polycrystalline Metal Alloy Using a Biaxially Oriented MgO Template,:
Q.X. Jia, S.R. Foltyn, P.N. Arendt, J.R. Groves, T.G. Holesinger, M.E. Hawley, and P. Lu,
Submitted to *Applied Physics Letters*.

3.3 Other Publications and Conference Abstracts

"Integration of Biaxally Aligned Conducting Oxides with Silicon Using Ion Beam Assisted Deposited MgO Templates,"
L.A. Emmert, B.H. Park, J.R. Groves, R.F. DePaula, Q.X. Jia, P.N. Arendt,
MRS Symposium Proceedings "Transport and Microstructural Phenomena in Oxide Electronics," vol. 666, eds. D.S. Ginley, *et al*., (Materials Research Society, Warrendale, PA, October 2001), p. F7.2.1.

"Ion-Beam Assisted Deposition of MgO with *in situ* RHEED Monitoring to Control Bi-axial Texture,"
J.R. Groves, P.N. Arendt, S.R. Foltyn, Q.X. Jia, R.F. DePaula, P.C. Dowden, H. Kung, T.G. Holesinger, L. Stan, L.A. Emmert, E.J. Peterson,
MRS Symposium Proceedings "Transport and Microstructural Phenomena in Oxide Electronics," vol. 666, eds. D.S. Ginley, *et al*., (Materials Research Society, Warrendale, PA, October 2001), p. F10.6.1.

"In-Situ Biaxial Texture Analysis of MgO Films during Growth on Amorphous
Substrates by Ion Beam-Assisted Deposition,"
R.T. Brewer, P.N. Arendt, J.R. Groves, H.A. Atwater,
MRS Symposium Proceedings "Mechanisms of Surface and Microstructure
Evolution in Deposited Films and Film Structures," vol. 672, eds. J. Sanchez, Jr., *et al*., (Materials Research Society, Warrendale, PA, October 2001), p. O6.2.1.

"Synthesis, Characterization and Ageing of MgB_2,"
A.C. Serquis, R.K. Schulze, Y.T. Zhu, J.Y. Coulter, D.E. Peterson, N.O. Moreno,
P.G. Pagliuso, S.S. Indrakanti, V.F. Nesterenko, and F.M. Mueller,
MRS Symposium Proceedings "Materials for High-Temperature Superconductor
Technologies," vol. 689, eds. M.P. Paranthaman *et al*., (Materials Research Society,
Warrendale, PA, 2002) p. 47.

"The Early Stages of Microstructural Development of the Colony Structure in Bi-2223
Tapes,"
T.G. Holesinger,
MRS Symposium Proceedings "Materials for High-Temperature Superconductor
Technologies," vol. 689, eds. M.P. Paranthaman *et al*., (Materials Research Society,
Warrendale, PA, 2002), p. 65.

"Spatial Distribution Analyses of Superconducting Transition Temperature in Epitaxial
$YBa_2Cu_3O_7$ Film Using Variable Temperature Scanning Laser Microscopy,"
S. Seo, C. Kwon, B.H. Park, and Q.X. Jia,
MRS Symposium Proceedings "Materials for High-Temperature Superconductor
Technologies," vol. 689, eds. M.P. Paranthaman *et al.,* (Materials Research Society,
Warrendale, PA, 2002), p. 283.

"Phase Diagram Studies in the SrO-CuO-TiO2 System; Applications to YBCO Coated
Conductors,"
A. Ayala, T.G. Holesinger, E.J. Peterson, and M. Archuleta,
MRS Symposium Proceedings "Materials for High-Temperature Superconductor
Technologies," vol. 689, eds. M.P. Paranthaman *et al*., (Materials Research Society,
Warrendale, PA, 2002), p. 289.

"Imaging Transport Current Distribution in High Temperature Superconductors Using
Room Temperature Scanning Laser Microscope,"
C. Kwon, B.E. Klein, S. Seo, B.H. Park, and Q.X. Jia,
MRS Symposium Proceedings "Materials for High-Temperature Superconductor
Technologies," vol. 689, eds. M.P. Paranthaman *et al*., (Materials Research Society,
Warrendale, PA, 2002), p. 295.

"Engineered Microstructures and Transport Properties in YBCO Coated Conductors"
T.G. Holesinger, B.J. Gibbons, J.Y. Coulter, S.R. Foltyn, J.R. Groves, P.N. Arendt,
MRS Symposium Proceedings "Materials for High-Temperature Superconductor
Technologies," vol. 689, eds. M.P. Paranthaman *et al*., (Materials Research Society,
Warrendale, PA, 2002), p. 329.

"Characterizing Transport Current Defects in 1-cm-Wide $YBa_2Cu_3O_{7-d}$ Coated
 Conductors,"
 G.W. Brown, M.E. Hawley, E.J. Peterson, J.Y. Coulter, P.C. Dowden, P.N. Arendt,
 S.R. Foltyn, F.M. Mueller,
 MRS Symposium Proceedings "Materials for High-Temperature Superconductor
 Technologies," vol. 689, eds. M.P. Paranthaman *et al*., (Materials Research Society,
 Warrendale, PA, 2002), p. 375.

 "Synthesis, Characterization and Superconductivity of MgB_2,"
 A.C. Serquis, Y.T. Zhu, J.Y. Coulter, D.E. Peterson, and F.M. Mueller,
 A*bstract for the 13th Annual Rio Grande Regional Symposium on Advanced
 Materials October 15, 2001, Albuquerque, NM.*

'Synthesis, Characterization and Ageing of MgB_2,"
 A. Serquis, Y.T. Zhu, D.E. Peterson, N.O. Moreno, P.J. Pagliuso, F.M. Mueller,
 Abstract submitted to the 2001 MRS Fall Meeting, Boston, MA, Nov. 25-30, 2001.

"X-Ray Diffraction Mapping of YBCO Superconducting Tape on a Mesostructural
 Scale,"
 E.J. Peterson, U. Preckwinkle, B.N. Herrington, F.M. Mueller, D.J. Brown, G.W.
 Brown, M.E. Hawley, J.Y. Coulter, S.R. Foltyn, P.N. Arendt, D.E. Peterson,
 Abstract submitted to the 2001 MRS Fall Meeting, Boston, MA, Nov. 25-30, 2001.

"(110)-Oriented Grain Boundaries in $YBa_2Cu_3O_7$-based Coated Conductors,"
 B.J. Gibbons, H.J. Kung, Q.X Jia, Steve R. Foltyn,
 Abstract submitted to the 2001 MRS Fall Meeting, Boston, MA, Nov. 25-30, 2001.

"AC Losses in Bi2223/Ag Tapes in Perpendicular Magnetic Fields: A Single Tape and
 Double Shorted Tapes,"
 M. Suenaga, J.R. Clem, and J.O. Willis,
 Abstract submitted to the 10th US Japan Workshop on High Tc Superconductors,
 Santa Fe, NM, December 2-5, 2001.

"Bridge-Type Fault Current Controller-A New Facts Controller, H.J. Boenig, C.H.
 Mielke, B.L. Burley, J.A. Waynert, J.O. Willis,"
 Abstract submitted to IEEE 2002 Power Engineering Society Summer Meeting
 Proceedings, Chicago, IL, July 21-25, 2002.

"Restoration and Testing of an HTS Fault Current Controller,"
 J.A. Waynert, H.J. Boenig, C.H. Mielke, and J.O. Willis,
 Abstract submitted to the Applied Superconductivity Conference, Houston, TX,
 August 4-9, 2002.

"Improvement of IBAD MgO Template Layers on Metallic Substrates for YBCO HTS Deposition,"
J.R. Groves, P.N. Arendt, S.R. Foltyn, Q.X. Jia, T.G. Holesinger, L.A. Emmert, R.F. DePaula, P.G. Dowden, L. Stan,
Abstract submitted to 2002 Applied Superconductivity Conference, Houston, TX, August 4-9, 2002.

"Materials Issues of YBCO and Nonlinear Dielectric Films for Tunable Microwave Devices,"
Q.X. Jia, A.T. Findikoglu, and P. Lu,
Abstract for the 2002 Applied Superconductivity Conference, Houston, TX, August 4-9, 2002.

"Fabrication of High J_c $YBa_2Cu_3O_{7-d}$ Tapes Using the Newly Developed Lanthanum Manganate Single Buffer Layers,"
M.P. Paranthanam, T. Aytug, S. Kang, R. Feenstra, J.D. Budai, D.K Christen, P.N. Arendt, L. Stan, R.F. DePaula, S.R. Foltyn, T.G. Holesinger, J.R. Groves,
Abstract for the 2002 Applied Superconductivity Conference, Houston, TX, August 4-9, 2002.

"Spatial Distribution Analyses of Critical Temperature in Epitaxial Y-Ba-Cu-O Film Using Variable Temperature Scanning Laser Microscopy,"
C. Kwon, L.B. Wang, S. Seo, B.H. Park, Q.X. Jia,
Abstract for the 2002 Applied Superconductivity Conference, Houston, TX, August 4-9, 2002.

"Variable Temperature Scanning Laser Microscopy of Wider Width High Temperature Superconducting Films,"
L.B. Wang, M.B. Price, C. Kwon, Q.X. Jia,
Abstract for the 2002 Applied Superconductivity Conference, Houston, TX, August 4-9, 2002.

"Accelerated Coated Conductor Program at Los Alamos National Laboratory,"
V. Matias, B.J. Gibbons, A.T. Findikoglu, S. Kreiskott, and L. Bronisz,
Abstract for the 2002 Applied Superconductivity Conference, Houston, TX, August 4-9, 2002.

"Growth and Characterization of $SrRuO_3$ Buffer Layer on MgO Template for Coated Conductors,"
Q.X. Jia, S.R. Foltyn, P.N. Arendt, T.G. Holesinger, J.R. Groves, M. Hawley,
Abstract for the 2002 Applied Superconductivity Conference, Houston, TX, August 4-9, 2002.

"Comparative Study of Buffer Layers on IBAD-MgO for Coated Conductors,"
Q.X. Jia, S.R. Foltyn, P.N. Arendt, J.R. Groves, R.F. DePaula, L. Stan,
Abstract submitted to 2002 Applied Superconductivity Conference, Houston, TX, August 4-9, 2002.

"The Influence of Structural Defects and Doping on Critical Current of Bulk MgB_2,"
A.C. Serquis, X.Z. Liao, Y.T. Zhu, J.Y. Coulter, L. Civale, D.E. Peterson, F.M. Mueller, J.D. Thompson, S. S. Indrakanti, and V.F. Nesterenko,
Abstract submitted to 2002 Applied Superconductivity Conference, Houston, TX, August 4-9, 2002.

"Ac Losses in Prototype Multistrand Conductors for the Detroit Edison DOE SPI Project,"
J.O. Willis, M.P. Maley, H.J. Boenig, G. Coletta, R. Mele, and M. Nassi,
Abstract submitted to 2002 Applied Superconductivity Conference, Houston, TX, August 4-9, 2002.

"High Critical Currents in Powder in Tube MgB_2 Wires: Influence of Microstructure and Heat Treatments,"
L. Civale, A.C. Serquis, D.L. Hammon, X.Z. Liao, J.Y. Coulter, Y.T. Zhu, T.G. Holesinger, D.E. Peterson, F.M. Mueller,
Abstract for the 2002 Applied Superconductivity Conference, Houston, TX, August 4-9, 2002.

"IBAD Template Layers For HTS Coated Conductors: Issues and Current Status at LANL,"
J.R. Groves, P.N. Arendt, S.R. Foltyn, R.F. DePaula, P.C. Dowden, L. Stan,
Abstract for the MRS International Workshop on Processing and Applications of Superconductors, Gatlinburg, TN, July 30-August 3, 2002.

"Microstructural Development in $YBa_2Cu_3O_y$ Coated Conductors,"
T.G. Holesinger, P.N. Arendt, Q.X. Jia, S.R. Foltyn, J.R. Groves, P.C. Dowden, R.F. DePaula,
Abstract for the MRS International Workshop on Processing and Applications of Superconductors, Gatlinburg, TN, July 30-August 3, 2002.

"Continuous Fabrication of $YBa_2Cu_3O_7$ Based Coated Conductors,"
B.J. Gibbons, V. Matias, A.T. Findikoglu, S. Kreiskott, L.N. Bronisz, DE. Peterson,
Abstract for 9th International Workshop on Oxide Electronics, St. Petersburg Beach, FL, October 19-24, 2002.

"Low Creep Rate Glassy Vortex Dynamics in High Density Bulk MgB_2,"
L. Civale, A.C. Serquis, M.P. Maley, J.Y. Coulter, Y.T. Zhu, X.Z. Liao, V.F. Nesterenko, S.S. Indrakanti, D.E. Peterson, and F.M. Mueller,
Abstract for the MRS 2002 Fall Meeting, Boston, MA, Dec. 2-6, 2002.

"Magnesium Oxide Templates for YBCO Coated Conductors,"
P.N. Arendt, J.R. Groves, S.R. Foltyn, Q.X. Jia, T.G. Holesinger, L. Emmert, R.F. DePaula, P.C. Dowden, L. Stan, J.Y. Coulter,
Abstract for the MRS 2002 Fall Meeting, Boston, MA, Dec. 2-6, 2002.

"Properties and Nanostructures of Materials Processed by SPD Techniques,"
Y.T. Zhu, A.C. Serquis, X.Z. Liao, L. Civale, D.L. Hammon, T. G. Holesinger, J.Y. Coulter, D.E. Peterson, and F.M. Mueller,
Abstract for the MRS 2002 Fall Meeting, Boston, MA, Dec. 2-6, 2002.

"The Structures of Oxygen-Related Defects in MgB_2,"
X.Z. Liao, A.C. Serquis, Y.T. Zhu, J. Huang, D.E. Peterson, F.M. Mueller, H. Xu,
Abstract for the MRS 2002 Fall Meeting, Boston, MA, Dec. 2-6, 2002.

"Influence of Microstructures and Heat Treatments on the Critical Current of Powder in Tube MgB_2 Wires and Tapes,"
A.C. Serquis, D.L Hammon, X.Z. Liao, L. Civale, J.Y. Coulter, Y.T. Zhu, T.G. Holesinger, D.E. Peterson, and F.M. Mueller
Abstract for the MRS 2002 Fall Meeting, Boston, MA, Dec. 2-6, 2002.

"Microstructural Development in $YBa_2Cu_3O_y$ Coated Conductors,"
T.G. Holesinger, P.N. Arendt, Q.X. Jia, J.R Groves, P.C. Dowden, R.F. DePaula,
Abstract for the MRS 2002 Fall Meeting, Boston, MA, Dec. 2-6, 2002.

"Deposition and Characterization of Superconducting $ReBa_2Cu_3O_7$ Films,"
Q.X. Jia, S.R. Foltyn, J.Y. Coulter, T.G. Holesinger, V.A. Maroni, K. Venkataraman,
Abstract for the MRS 2002 Fall Meeting, Boston, MA, Dec. 2-6, 2002.

"IBAD MgO Template Development for YBCO Coated Conductors,"
P.N. Arendt, J.R. Groves, T.G. Holesinger, S.R. Foltyn, Q.X. Jia, L. Emmert, R.F. DePaula, P.C. Dowden, and L. Stan,
Abstract for the MRS 2002 Fall Meeting, Boston, MA, Dec. 2-6, 2002.

4. Patent and License Activity (April 1988 to Present)

4a. Invention Disclosures and Patent Applications

Designation	Date	Subject	Submitted by
DOE S-89,678 S.N. 09/152,813	 Filed 9/14/98	Superconducting Structure	C. Kwon, Q.X. Jia, and S.R. Foltyn
DOE S-89,679 S.N. 60/100,215 S.N. 09/787,224	 Filed 9/14/98 Filed 3/14/01	Superconducting Structure Including Mixed Rare-Earth Barium Copper Oxide Compositions	C. Kwon, Q.X. Jia, S.R. Foltyn, J.L. Smith, W.L. Hults, E.J. Peterson
DOE S-91,761 S.N. 60/213,111 S.N. 09/867,842	 Filed 6/21/00 Filed 5/29/01	Architecture for High Critical Current Superconducting Thick Films	Q.X. Jia S.R. Foltyn T.G. Holesinger
DOE S-94,668 S.N. 60/170,968 S.N. 09/616,570	 Filed 12/15/99 Filed 7/14/00	Surface Control of Alloy Substrates and Methods of Manufacture Thereof	L.G Fritzmeier, Q. Li, M.W. Rupich, E. Thompson, E. Siegel, C. Thieme, S. Annavurapu, P.N. Arendt, S.R. Foltyn
DOE 94,720	7/13/00	Apparatus for Heating a Moving Tape	S. R. Foltyn, P.C. Dowden
DOE 94,726 S.N. 09/731,534	 Filed 12/06/00	High Temperature Superconducting Thick Films	P.N. Arendt, S.R. Foltyn, J.R. Groves, T.G. Holesinger, Q.X. Jia
DOE 94,731 S.N. 09/731,646	 Filed 12/06/00	Superconducting Composite Structures	T.G. Holesinger S.R. Foltyn
DOE 94,732 S.N. 09/721,834	 Filed 11/22/00	Adjustable Direct Current and Pulsed Fault Current Limiter	H.J. Boenig J.B. Schillig
DOE 94,734 S.N. 60/333,917 S.N. 10/113,475	 Filed 11/21/01 Filed 3/28/02	Composition of Matter for Superconducting Composite Conductors and Manufacturing of Same	T.G. Holesinger, S.R. Foltyn, P.N. Arendt, J.R. Groves, Q.X Jia, A. Ayala
DOE S-97,723 S.N. 10/113,476	 Filed 5/30/01	High Critical Current Superconducting Tapes	T G. Holesinger, Q.X. Jia S.R. Foltyn
DOE S-97,725 **S.N. 10/113,476**	 **Filed 3/28/02**	**Buffer Layer on Metal Alloy Substrates for Superconducting Tapes**	**Q.X. Jia, S.R. Foltyn, P.N. Arendt, J.R. Groves**
DOE S-97,795 **S.N. 10/209,391**	 **Filed 7/31/02**	**Multilayer Composites and Manufacture of Same**	**T.G. Holesinger, Q.X. Jia**
DOE S-97,803 **S.N. 10/161,132**	 **Filed 5/29/02**	**Reduced AC Losses in HTS Coated Conductors**	**S.P. Ashworth**
DOE S-97,804 **S.N. 10/096,774**	 **Filed 3/13/02**	**Synthesis of Magnesium Diboride by Magnesium Vapor Infiltration**	**A. Serquis, Y.T. Zhu, F.M. Mueller, D.E. Peterson, X.Z. Liao**
DOE S-99,943 **S.N. 10/242,895**	 **Filed 9/11/02**	**Buffer Layers on Metal Alloy Substrates for Superconducting Tapes**	**Q.X. Jia, S.R. Foltyn, P.N. Arendt, J.R. Groves**

Designation	Date	Subject	Submitted by
DOE S-99.947	**Disclosed 9/10/02**	**Processing of High Density MgB$_2$ Wires by Hot Isostatic Pressing**	**Y.T. Zhu, A. Serquis, D. Hammon, L. Civale, X.Z. Liao, F.M. Mueller, D.E. Peterson, V. Nesterenko, Y. Gu**
DOE S-99.952	**Disclosed 9/16/02**	**Use of High Current Density Electropolishing for the Preparation of Very Smooth Substrate Tapes for Coated Conductor Applications**	**S. Kreiskott, V. Matias, P.N. Arendt. S.R. Foltyn**

4b. Patents Granted

Designation	Date	Subject	Issued to	Status
DOE S-63,245 S.N. 07/041,950 US Pat.4,784,686	Filed 04/24/87 Issued 11/15/88	Synthesis of Ultrafine Powders by Microwave Heating	T.T. Meek H. Sheinberg R.D. Blake	Expired 05/15/00
DOE S-68,033 S.N. 07/454,607 US Pat. 5,008,622	Filed 12/21/89 Issued 04/16/91	Superconductive Imaging Surface Magnetometer	W.C. Overton, Jr D. van Hulsteyn E.R. Flynn	Expired 10/16/98
DOE S-68,041 S.N. 07/330,329 US Pat 5,006,672	Filed 03/29/89 Issued 04/09/91	Apparatus for Storing High Magnetic Fields Having Reduced Mechanical Forces and Reduced Magnetic Pollution	M.L. Prueitt F.M. Mueller J.L. Smith	Maint. Fee 3 due 10/09/02
DOE S-68,042 S.N. 07/276,188 US Pat 4,873,444	Filed 11/23/88 Issued 10/10/89	Detection of Surface Impurity Phases in HTS Using Thermally Stimulated Luminescence	D.W. Cooke M.S. Jahan	Expired 10/10/97
DOE S-68,086 S.N. 07/311,998 US Pat 4,992,696	Filed 02/17/89 Issued 02/12/91	Apparatus Having Reduced Mechanical Forces for Supporting High Magnetic Fields	M.L. Prueitt F.M. Mueller J.L. Smith	Maint. Fee 3 payed 08/12/02
DOE S-68,098 S.N. 07/324,264 US Pat 5,015,952	Filed 03/14/89 Issued 05/14/91	Apparatus for Characterizing Conductivity of Materials by Measuring the Effect of Induced Shielding Currents Therein	J.D. Doss	Expired 05/14/99
DOE S-71,082 S.N. 07/671,231 US Pat 5,102,863	Filed 03/19/91 Issued 04/07/92	Process for Producing Clad Superconducting Materials	R.B. Cass K.C. Ott D.E. Peterson	Expired 10/07/99

Designation	Date	Subject	Issued to	Status
DOE S-71,084 S.N. 07/670,111 US Pat 5,134,360	Filed 03/15/91 Issued 07/28/92	Apparatus and Method for Critical Current Measurements	J.A. Martin R.C. Dye	Expired 01/28/00
DOE S-72,816 S.N. 07/690,725 US Pat 5,268,646	Filed 04/24/91 Issued 12/07/93	Apparatus & Method for Characterizing Conductivity of Materials	J.D. Doss	Maint. Fee 2 due 06/07/01
DOE S-72,851 S.N. 07/860,337 US Pat. 5,238,913	Filed 03/30/92 Issued 08/24/93	Superconducting Micro-circuitry by the Micro-lithographic Patterning of Superconducting Compounds and Related Materials	N.V. Coppa	Maint. Fee 2 due 02/24/01
DOE S-72,861 S.N. 813,726 US Pat 5,262,394	Filed 12/27/91 Issued 11/16/93	Superconductive Compositions Including Cerium Oxide Layer	X.D. Wu R. Muenchausen	Maint. Fee 2 due 05/16/01
DOE S-72,880 S.N. 07/774,748 US Pat 5,278,138	Filed 10/11/91 Issued 01/11/94	Aerosol Chemical Vapor Deposition of Metal Oxide Films	K.C. Ott T.T. Kodas	Maint. Fee 2 due 05/16/01
DOE S-72,898 S.N. 814,355 US Pat 5,252,551	Filed 12/27/91 Issued 10/12/93	Superconductive Articles	X.D. Wu, R.E. Muenchausen	Maint. Fee 2 due 01/11/01
DOE S-72,899 S.N. 813,727 US Pat 5,270,294	Filed 12/27/91 Issued 12/14/93	Free-Standing Superconductive Articles	X.D. Wu, R.E. Muenchausen	Maint. Fee 2 due 06/14/01
DOE S-75,023 S.N. 08/419,485 US. Pat 5,554,224	Filed 03/31/94 Issued 09/10/96	Substrate Heater for Thin Film Deposition	S.R. Foltyn	Maint. Fee 2 due 03/10/04
DOE S-75,081 S.N. 08/067,911 US Pat 5,300,486	Filed 05/27/93 Issued 04/06/94	Synthesis of BiPbSrCaCuO Superconductor	W.L. Hults, K.A Kubat-Martin, K.V. Salazar, D.S. Phillips, D.E. Peterson	Maint. Fee 2 due 10/05/01
DOE S-78,394 S.N. 08/419,485 US. Pat. 5,569,641	Filed 04/10/95 Issued 10/29/96	Preparation of Superconducting Bi-2223 Wire	M.G. Smith J.O. Willis D.E. Peterson	Maint. Fee 2 due 04/29/04
DOE S-80,400 S.N. 08/168,331 US Pat 5,434,128	Filed 12/17/93 Issued 07/18/95	Superconducting Wire	D.A. Korzekwa J.F. Bingert D.E. Peterson H. Sheinberg	Maint. Fee 2 due 01/18/03

Designation	Date	Subject	Issued to	Status
DOE S-82,620, S.N. 08/425,752 US Pat. 5,872,080	Filed 04/19/95 Issued 02/16/99	High Temperature Superconducting Thick Films	P.N. Arendt X.D. Wu S.R. Foltyn	Maint. Fee 1 due 08/16/02
DOE S-82,623 S.N. 08/608,069 US Pat. 5,958,842	Filed 02/28/96 Issued 09/28/99	Melt Processing of Superconductors Using Alumina	T.G. Holesinger	Maint. Fee 1 due 03/28/03
DOE S-82,633 US Pat. 5,726,848	Filed 05/8/96 Issued 3/10/98	Fault Current Limiter and Alternating Current Circuit Breaker	H.J. Boenig	Maint. Fee 1 due 09/10/01
DOE S-84,942 S.N. 08/597,061 US Pat. 5,908,812	Filed 02/05/96 Issued 06/01/99	Structure for HTS Composite Conductors & Manufacture of Same	J.D. Cotton G.N. Riley	Maint. Fee 1 due 12/01/02
DOE S-84,965 S.N. 08/865,827 US Pat.5,820,678	Filed 09/23/96 Issued 10/13/98	Solid Source MOCVD Delivery System	B.N. Hubert X.D. Wu	Maint. Fee 1 due 04/13/02
DOE S-89,600 S.N. 60/074,717 S.N. 09/249,476	Filed 2/13/98 Filed 02/12/99 Issued 3/6/01	Compressive Annealing of BSCCO-2223 Superconductive Tapes	Y.T. Zhu, P.S. Baldonado, J.F. Bingert, T.G. Holesinger, D.E. Peterson	Maint. Fee due 3/06/04
DOE S-89,624 **S.N. 08/942,038** **US Pat. 6,428,635**	**Filed 10/1/97** **Issued 8/6/02**	**Substrates for Superconductors**	**L.G. Fritzmeier, E. Thompson, E. Siegel, C. Thieme, R.D. Cameron, J.L. Smith, W.L. Hults**	**Maint. Fee due 8/6/05**
DOE S-91,736 S.N. 60/138,326 S.N. 09/615,640 US Pat. 6,451,742	**Filed 06/09/99 Filed 7/13/00 Issued 9/17/02**	**High Temperature Superconducting Composite Conductor & Method for Manufacturing the Same**	**T.G. Holesinger and J.F. Bingert**	**Maint. Fee due 9/17/05**
DOE S-91,748 S.N. 60/143,781 S.N. 09/615,640 US Pat. 6,452,375	**Filed 7/13/99 Filed 7/13/00 Issued 9/17/02**	**Apparatus for Measurement of Critical Current in Superconductive Tapes**	**J. Y. Coulter R.F. DePaula**	**Maint. Fee due 9/17/05**
DOE S-91,761 S.N. 60/213,111 S.N. 09/867,842 US Pat. 6,383,989	**Filed 6/21/00 Filed 5/29/01 Issued 5/7/01**	**Architecture for High Critical Current Superconducting Thick Films**	**Q.X. Jia S.R. Foltyn T.G. Holesinger**	**Maint. Fee due 11/7/05**

4c. Licenses Granted

License Number	Date	Subject	Issued to
89-41-0000-1	12/28/88 (Terminated 11/94)	Apparatus for Characterizing Conductivity of Materials by Measuring the Effect of Induced Shielding Currents Therein	Lakeshore Cryotronics
99-C00510.1	11/11/98	Superconductive Article including Cerium Oxide Layer	DuPont Superconductivity
01-C01080.0	05/29/01	High Temperature Superconductor Material	IGC-SuperPower, LLC
01-C01081.0	05/29/01	High Temperature Superconductor Material	IGC-SuperPower, LLC
01-C01082.0	05/29/01	Fault Current Limiter and Alternating Current Circuit Breaker Device	IGC-SuperPower, LLC

5. Agreements in Progress (14 Active, all types)

5a. Superconductivity Pilot Center Agreements – Active:
None

5b. CRADA Agreements - Active

Organization	Topic	PI	Funding,$K DOE	Funding,$K Partner	Dates
Oxford Superconducting Technology	Bi-2212 HTS Tapes	Smith Holesinger Holesinger	290 55 700	290 100 730	11/93 -11/96 10/97–10/98 5/99-10/05
3M Corporation	Coated Conductors	Peterson	960 720 400	1375 720 150	3/97-3/99 3/99-5/00 5/00-1/02
IGC-SuperPower	Coated Conductors	Foltyn Balachandran	700, LANL 500, ANL	1300	1/00-1/03
American Superconductor Corp.	**Bi-2223 Wire Development**	**Holesinger**	**450**	**450**	**5/02-5/04**
General Electric	**HTS Generator**	**Waynert**	**860**	**860**	**4/02-4/04**
DuPont	**HGMS Magnetic Separation**	**Waynert**	**120 LANL 300 FI Dupont**	**200**	**6/02-6/04**
Hyper Tech Research, Inc.	**MgB$_2$ Wire Development**	**Mueller**	**400**	**400**	**9/02-9/04**

5c. Funds In / Funds Out Agreements – Active:
None

5d. Other Collaborations - Active

Organization	Topic	PI	Dates
ASC/ ANL/ ORNL/ U. Wisconsin/ (previously, NIST-Gaithersburg)	Bi-2223 Wire Development (Wire Development Group)	J. Willis Holesinger	11/91-11/00 11/00-
3M/ORNL/ Southwire / Stanford University	Coated Conductor Group	E. Peterson	3/97-
ASC/ ORNL/ LBNL/U. Wisconsin/ Stanford U./MIT/ Wright-Patterson AFB/ EPRI (previously, TCSUH)	Coated Conductor Development Group	J. Willis Holesinger	2/96- 11/00-
Oak Ridge National Laboratory	HTS Information Exchange	D. Peterson	In Progress
Argonne National Laboratory	HTS Information Exchange	D. Peterson	In Progress
Sandia National Laboratories	HTS Information Exchange	D. Peterson	In Progress
Brookhaven National Lab.	HTS Information Exchange	D. Peterson	In Progress

6. Completed Agreements

6a. Superconductivity Pilot Center Agreements - Completed

Organization	Topic	PI	Funding,$K DOE	Funding,$K Partner	Dates
CPS Superconductor	Metal-Ceramic Interfaces	Mitchell	102.6	80.8	9/89 - 9/90
DuPont / Hewlett-Packard	HTS Electronic Components	Peterson	3777	7200	10/89 - 10/92
Space Industries, Inc.	Microgravity Processing	Peterson	205	247	4/90 - 4/91
Cryopower Associates	Improvement of Bulk HTS Materials	Maley Maley	45.2 199.4	60 485.9	Ph 1: 2/90 Ph 2: 1/92 1/94
HiTc Superconco	Optimizing Performance of HTS Cavities and Targets	Wu Wu	136.6 101.9	125 100	Ph 1: 9/89 Phase 2: 12/91
Ceracon, Inc	Bulk HTS Consolidation	Foltyn	237.5	300	Phase 1: 6/91
Nuclear Metals/ SNL/AT&T	HTS Co-extrusion	Wallace Bingert	239.2 239.2	760.5 285 NM 190 ATT	Ph 1: 8/90- 8/93 Ph. 2: 10/93-10/96
The Boeing Company	Superconducting Electromagnetic Devices	Peterson	240	240	4/97 - 4/98
Power Superconduct-ing Devices, Inc	Development of HTS Fault Current Limiter	Peterson	250	250	7/96-7/98

American Superconductor Corporation	Bi-2223 Conductors	Peterson	170.5	179	Ph 1: 6/89-
		Peterson	587.1	350	Ph 2: 11/91-
		Willis	1500	950	Ph 3: 2/94-
	HTS Composite Conductors	Willis	2300	1100	Ph 4: 3/96-
		Willis	1800	1800	Ph.5: 7/98-3/01
		Holesinger			

6b. CRADA Agreements - Completed

Organization	Topic	PI	Funding,$K DOE	Funding,$K Partner	Dates
Lockheed Martin	Coil Development	Peterson	330	210	7/93 - 7/96
Plastronic, Inc.	Liquid Cryogen Free HTS Magnet System	Daugherty	100 +33k funds in	67	6/95 - 5/96
The BOC Group, Inc.	Superconducting Coated Materials	Peterson	70	70	2/23/96-11/22/96
EURUS Technologies, Inc.	Development of HTS Current Leads & Solders	Peterson	80	140	2/6/96-2/5/97
Eriez Magnetics	HTS Magnetic Separation	Daugherty	70	52	4/2/96-4/1/97
Lockheed Martin	HTS Current Limiter	Peterson	400	400	11/95-10/97
Lockheed Martin	Bridge-Type Fault Current Limiter	Boenig	700	1400	11/95-9/98
General Atomics (assumed LM activity)	Bridge-Type Fault Current Limiter	Peterson	Remainder of 700 from above	Remainder of 1400 from above	9/98-5/99, 5/99-11/99
Astronautics Corp. of America	Active HTS Magnetic Refrigerator	Peterson	200	200	4/98-7/00
ABB Power T&D Co., Inc.	HTS Transformer	Maley	95	70	7/99-7/00

6c. Funds In / Funds Out Agreements - Completed

Organization	Topic	PI	Type	Value $K	Dates
Superconductor Technologies, Inc.	Rutherford Backscattering	Maggiore	Funds In	1.0	5/88 - 5/89
Public Service Co. of New Mexico	HTS Theory	Parkin	Funds In	357.1	6/88 - 6/90
EPRI	Assessments for Utilities	Newkirk	Funds In	99.8	6/88 - 6/89

AMP, Inc.	RF Characterization of TI-Based HTS Films	Wallace	Funds In	102.9	1/89 - 5/89
EPRI	Heat Pipe Switch	Merrigan	Funds In	150	1/89 - 1/90
Univ. Missouri, Rolla	HTSC Fibers	Maestas	Funds Out	111	1/89 - 1/90
Bechtel	SMES Systems/ Hot-to-Cold Transitions	Maestas	Funds Out	10	2/89 - 2/90
Rocketdyne Corp., Rockwell, Intl.	Synthesis of TI HTS	Peterson	Funds Out	95.3	5/89 - 5/90
EPRI	New Families of HTS	Smith	Funds In	120	2/90 - 2/92
Underground Systems	Transmission Systems	Stewart	Funds In	48	5/91 - 5/92
W.J. Schafer Assoc.	SMES Assessment	Peterson	Funds Out	89.9	5/92 - 5/93
Univ. Calif.-San Diego	Hydrocode Models	Peterson	Funds Out	63 57	12/92 -12/93 6/94 - 5/95
Intermagnetics General Corporation	TI-Based HTS Coils	Peterson	Funds Out	400	10/92 - 10/96
MIT	Bitter Magnets	Peterson	Funds In	50	5/93 - 4/96
Midwest Super-conductivity, Inc.	IBAD-Coated Flexible Substrates	Peterson	SBI Tech Consulting Agreement	5	3/95 - 3/96
EPRI	Ac Loss Measurements in HTS Cables	Maley	Funds In	150	9/5/95-9/4/96
EPRI	Thick Films on Flexible Substrates	Wu	Funds In	25 200	7/95-9/95 10/95-10/96
Pirelli Cable & Systems	Ac Losses on HTS Cables	Peterson Willis	Funds In	55 63	11/97 – 6/98 1/99 – 9/99

6d. Other Collaborations - Completed

Organization	Topic	PI	Dates
Tektronix, Inc.	Cryogenic Materials Characterization	J. Smith	11/89-5-94